

# Chapter 1

## The Traveltime Seismic Tomography

### 1.1 Inverse methods in Geophysics: general description

We define “Inverse methods” or “Inverse theory” a complex of mathematical methods (above all numerical) which allows us to extract informations about a physical system starting from observed data. This theory is based on two elements: the observed data and the model (described by means of a series of parameters). The last one conveys our knowing of physical system. Observed data could be direct or indirect measurings of physical quantities that we want to investigate. Instead, model represents our idea on connection between physical system's parameters and observed data and generally it is a mathematical relation. Each inverse method is solved searching solutions at two problems.

- Forward problem: Starting from an initial estimate of model parameters, we obtain theoretical data. These must be compared with observed data to have an estimate of model parameters in the best way possible
- Inverse problem: It consists in the minimization of difference between observed data and theoretical data, in a way to obtain the better model estimate. Generally, this problem is solved in an iterative way.

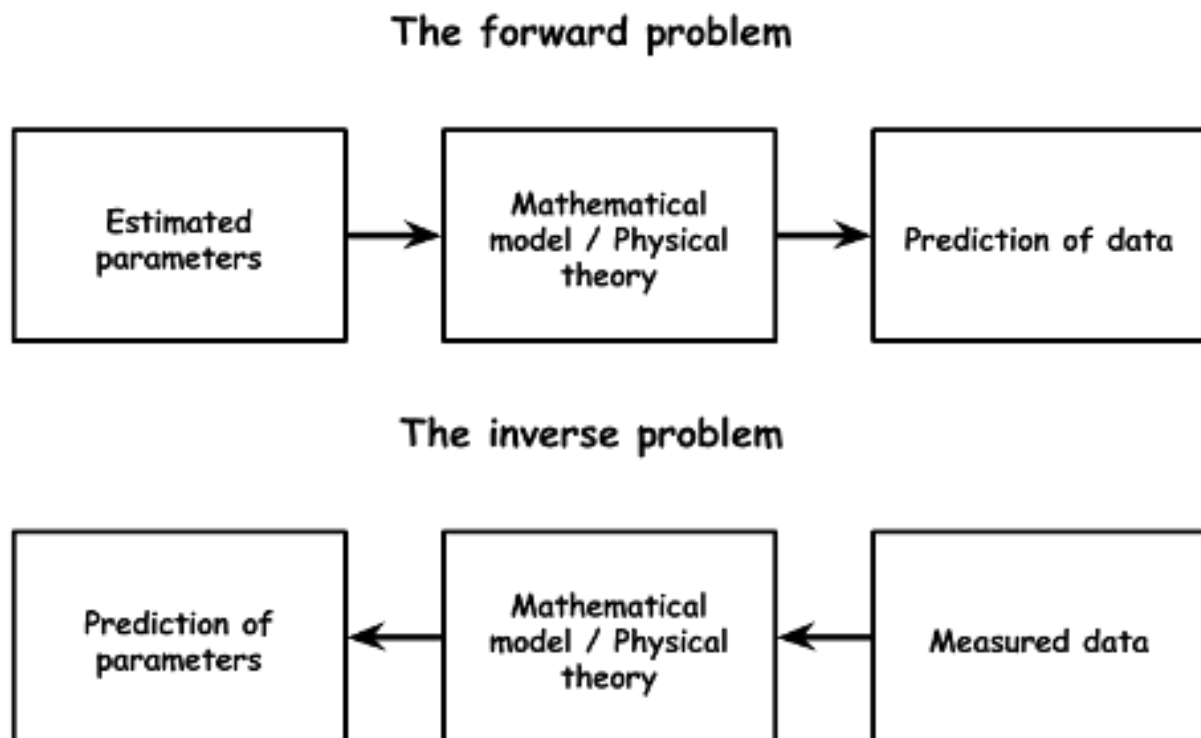


Figure 1.1: Schematical description of the forward and the inverse problem

The majority of Inverse Methods implicitly include computation of Forward problem.

In addition to this goal, inverse methods have other aims. For example, the unicity and the goodness of obtained solution, the study of effect that mistakes in measurement of data could have on model parameters, the study of goodness of so-called “study of resolution”. That is, if our instruments are arranged in a way that observed data could supply us a correct description of model parameters.

## 1.2 Mathematical general description of Inverse Methods

We suppose that we have made  $N$  measures on a particular physical system and we organise them in a vector  $\mathbf{d}$ , that we named “data vector”.

$$\mathbf{D} = [\mathbf{d}_1, \mathbf{d}_2, \mathbf{d}_3, \dots, \mathbf{d}_N] \quad (1.1)$$

We make the same procedure with the  $M$  parameters of physical system and we organise them in a vector  $\mathbf{m}$ , which we named “parameter vector”

$$\mathbf{m} = [\mathbf{m}_1, \mathbf{m}_2, \mathbf{m}_3, \dots, \mathbf{m}_M] \quad (1.2)$$

Now, we should define a mathematical relations which representing the model. Before of proceeding, it's a well thing to underline that, generally, there is not a unique model. An inverse method could show us the validity or not of a determined model, considering the misfit of observed data. So, there is two ways of proceeding. First option is to verify the reliability of various models by means of statistical test. Second one is considering an error on utilized model (for example, setting an error to parameters).

Model is represented by a series of  $L$  equations which have the following form:

$$\mathbf{f}_1(\mathbf{m}, \mathbf{d}) = \mathbf{0}, \mathbf{f}_2(\mathbf{m}, \mathbf{d}) = \mathbf{0}, \dots, \mathbf{f}_L(\mathbf{m}, \mathbf{d}) = \mathbf{0} \quad (1.3)$$

We can easily notice that these equations depends on data and parameters.

In the majority of cases, we can separate data and model parameters and obtaining  $L=N$  equations of model which depend on data in a linear way but depend on parameters in a non linear way. If we are able to “linearize” these last equations, thus we obtain a system of linear equations which we can summarize in the following form:

$$\mathbf{d}_i = \sum_{j=1, M} \mathbf{G}_{ij} \mathbf{m}_j \quad (1.4)$$

$\mathbf{G}_{ij}$  is a  $N \times M$  coefficient matrix with  $N$  data and  $M$  parameters. For “linearizing” inverse problem in Geophysics, generally it is preferable to apply a perturbative approach (for example, a Taylor Series arrested at first order). In this case, problem is solved computing perturbations of parameters in comparison with those one unperturbed of starting model. For each  $i$ -th datum, we can define the difference between its theoretical estimate ( $d_i^{\text{TEO}}$ ) and its effective measure ( $d_i^{\text{OBS}}$ ). We name this difference ***residual***

$$\mathbf{e}_i = \mathbf{d}_i^{\text{OBS}} - \mathbf{d}_i^{\text{TEO}} \quad (1.5)$$

The solution of inverse problem could be found minimising the following function:

$$\mathbf{E} = \|\mathbf{e}\|_2 = [\sum_{i=1, N} |\mathbf{e}_i|^2]^{1/2} \quad (1.6)$$

that is the euclidean norm or  $L_2$  norm of (1.5), interpreting it as a vector

which represent the euclidean distance between observations and their predicted values according to chosen model. Practically, we can solve an inverse problem by means of a *Least Squares* method. Through the choice of this kind of norm, we define a gaussian distribution of observed data. If we choice a norm with a high power, we should give importance to data which strongly move away from their theoretical estimates.

Thus, following a Least Squares method, we should make the derivative of (1.6) for each model parameter and put each derivative equal to 0. If we consider  $\mathbf{e}$  as a vector  $\mathbf{e} = [e_1, e_2, \dots, e_N]$ , the  $i$ -th component  $e_i$ , as indicated by the (1.4) and (1.5), is given by:

$$\mathbf{e}_i = \mathbf{d}_i^{\text{OBS}} - \sum_{j=1, M} \mathbf{G}_{ij} \mathbf{m}_j \quad (1.7)$$

This relation could be written in a more compact form as:

$$\mathbf{e} = \mathbf{d} - \mathbf{Gm} \quad (1.8)$$

According to (1.6), then, we can write

$$\mathbf{E} = \mathbf{e}^T \mathbf{e} = (\mathbf{d} - \mathbf{Gm})^T (\mathbf{d} - \mathbf{Gm}) \quad (1.9)$$

Computing the partial derivatives of (1.9) for each model parameter and put them equal to 0, we obtain a series of equation which in a matrix form we can write as:

$$\mathbf{G}^T \mathbf{Gm} - \mathbf{G}^T \mathbf{d} = \mathbf{0} \quad (1.10)$$

where  $\mathbf{G}^T\mathbf{G}$  is a  $M \times M$  square matrix. If the inverse matrix  $(\mathbf{G}^T\mathbf{G})^{-1}$  exists, the solution of inverse problem is given by:

$$\mathbf{m}^{\text{sti}} = (\mathbf{G}^T\mathbf{G})^{-1}\mathbf{G}^T\mathbf{d} \quad (1.11)$$

where  $\mathbf{m}^{\text{sti}}$  represent the model parameters estimate.

### 1.3 Overdetermined inverse problems: assigning a weight to data and parameters

A overdetermined inverse problem is a kind of inverse problem with  $N$  observed data and  $M$  model parameters, where  $N > M$ . Given that part of data could be affected by error due to various causes (examples: precision of instrument, presence of noise, etc...), it might help the goal of a better solution for the problem assigning some weights to observed data, in a way to underline the importance of data which are less affected by errors. If we named  $w_i$ , the  $i$ -th weight which we assign at  $i$ -th datum  $e_i$ , so (1.6) becomes:

$$E = \sum_{i=1,N} w_i (\mathbf{d}_i - \mathbf{G}\mathbf{m})^2 = \mathbf{e}^T \mathbf{W} \mathbf{e} \quad (1.12)$$

where  $\mathbf{W}$  is the  $N \times N$  diagonalised weight matrix. In fact, we put the condition that weights are normalised to 1. In this way, (1.11) becomes:

$$\mathbf{m}^{sti} = (\mathbf{G}^T \mathbf{W} \mathbf{G})^{-1} \mathbf{G}^T \mathbf{W} \mathbf{d} \quad (1.13)$$

We could assign a weight to model parameters, too. In this case, we assume an *a priori* knowledge of model and of maximum expected variation of model parameters. This could be the case of inverse problems solved by means of a perturbative approach, where the parameters we want to determine are the gaps in comparison with a pre-determined value. This last one, generally, is the mean value of (1.2)  $\langle \mathbf{m} \rangle$ . The equation (1.9) becomes:

$$\mathbf{E} = \mathbf{E}_d + \mathbf{E}_m = \sum_{i=1,N} |\mathbf{e}_i|^2 + \sum_{i=1,M} |\mathbf{m}_i - \langle \mathbf{m} \rangle|^2 = \mathbf{e}^T \mathbf{e} + (\mathbf{m} - \langle \mathbf{m} \rangle)^T (\mathbf{m} - \langle \mathbf{m} \rangle) \quad (1.14)$$

where  $\mathbf{E}_m$  is the so called *minimum length constrain*. In this way, the (1.11) becomes:

$$\mathbf{m}^{sti} = [\mathbf{G}^T \mathbf{G} + \mathbf{I}]^{-1} [\mathbf{G}^T \mathbf{d} + \langle \mathbf{m} \rangle] \quad (1.15)$$

where  $\mathbf{I}$  is the identity matrix. If we want to emphasize the error in data, we introduce a *damping factor*  $\varepsilon$  in a way that (1.14) and (1.15) become respectively:

$$\mathbf{E} = \mathbf{e}^T \mathbf{e} + \varepsilon (\mathbf{m} - \langle \mathbf{m} \rangle)^T (\mathbf{m} - \langle \mathbf{m} \rangle) \quad (1.16)$$

$$\mathbf{m}^{sti} = [\mathbf{G}^T \mathbf{G} + \mathbf{I}]^{-1} [\mathbf{G}^T \mathbf{d} + \langle \mathbf{m} \rangle] \quad (1.17)$$

If we assign a weight both to observed data and to model parameters, we have the following general formula:

$$\mathbf{m}^{sti} = \langle \mathbf{m} \rangle + [\mathbf{G}^T \mathbf{W}_d \mathbf{G} + \varepsilon \mathbf{W}_m]^{-1} \mathbf{G}^T \mathbf{W}_d [\mathbf{d} - \mathbf{G} \langle \mathbf{m} \rangle] \quad (1.18)$$

where  $\mathbf{W}_d$  and  $\mathbf{W}_m$  are respectively weights matrix for observed data and weights matrix for model parameters.

## 1.4 Error estimate on least squares solution

Least squares solution represents the point in the space of parameters  $\mathbf{m}$  where function (1.9) has a minimum. Practically, we must establish the minimum of curve  $E(\mathbf{m})$ . To do this, we must introduce a **covariance matrix** which describes error on solution and model parameters correlation. On the diagonal of this matrix, we have the error, while elements out of the diagonal express correlation coefficients among model parameters. The **covariance matrix** has the following form:

$$\mathbf{cov}(\mathbf{m}) = \sigma_d^2 [\mathbf{G}^T \mathbf{G}]^{-1} \quad (1.19)$$

where  $\sigma_d$  is the standard error on observed data. It is simple to show, computing two times the derivative of (1.9) respect to  $\mathbf{m}$  that:

$$(\mathbf{1}/2)(\partial^2 \mathbf{E} / \partial \mathbf{m}^2) = [\mathbf{G}^T \mathbf{G}] \quad (1.20)$$

and, making a comparison between (1.19) and (1.20) we have:

$$\mathbf{cov}(\mathbf{m}) = \sigma_d^2 [\mathbf{G}^T \mathbf{G}]^{-1} = \sigma_d^2 [(\mathbf{1}/2)(\partial^2 \mathbf{E} / \partial \mathbf{m}^2)]_{\mathbf{m}=\mathbf{m}^{sti}}^{-1} \quad (1.21)$$

Thereby, small variations of (1.20) (that is small variations of the curve around the minimum) produce big variances (mistakes) in the least squares solution (see following figure).

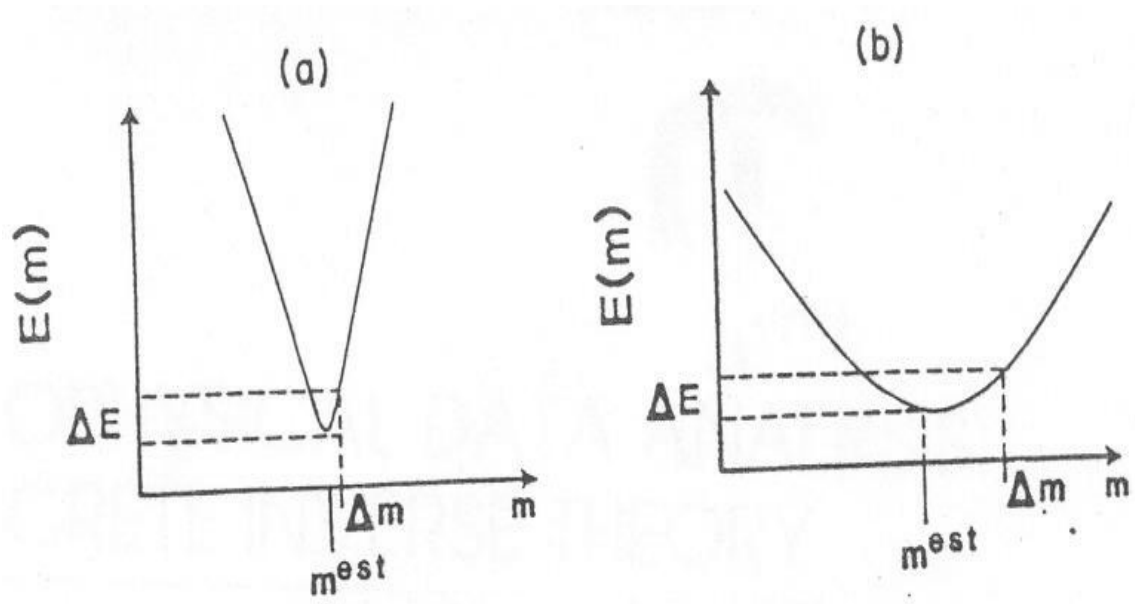


Figure 1.2: graphical representation of function  $E(m)$

## 1.5 The traveltimes seismic tomography – general description

Through the word “tomography”, we describe a process used in many known sciences (for example, medicine, oceanography, etc...) where there is an only aim: discovering the internal structure of a determined system by means of a series of sources which illuminate it. For example, the CAT (Computer Axial Tomography) is used in medicine and consists in X-Ray beams which “barrage” the body of person to light up his (or her) internal. The principle of traveltimes seismic tomography is the same. This process allows us to know a structure in depth of a determined part of Earth. The “sources” used are the traveltimes of earthquakes registered by a specific network (distributed on area following a geometrical criterion) of seismic stations. Inverting these traveltimes, we can obtain a 3D distribution of seismic velocities and, so on, we can reconstruct the internal structure of the area which we are examining. So, traveltimes seismic tomography is an Inverse Method and therefore, solving it we must solve two problems: a forward problem and an inverse problem. We can summarise the basis of them in the following way.

- **FORWARD PROBLEM:** We must compute theoretical traveltimes starting from an estimate of hypocentral parameters. This estimate is obtained by a 1-D starting velocity model.
- **INVERSE PROBLEM:** We must make a comparison between theoretical traveltimes and observed traveltimes. The goal is to “minimize” their difference, that we named ***residual***. In this way, we can obtain a 3D velocity model of the area and we can obtain so on a

re-localization of hypocenters (this last point is true only when we use passive sources (that is, natural seismic events) and not active sources (that is, artificial seismic events)).

Both problems can be solved by means of numerical techniques. Generally, traveltime seismic tomography is a non linear problem. It is very simple to understand why. A generic travel time  $\mathbf{T}$  along a ray  $\mathbf{r}$  is given by:

$$\mathbf{T} = \int_{r(s)} \mathbf{s}(\mathbf{r})d\mathbf{s} \quad (1.22)$$

where  $\mathbf{s}$  is the slowness, that is the reciprocal of velocity  $\mathbf{v}$ . Using slowness instead of velocity, we could affirm that expression (1.22) is linear. This affirmation is wrong. In fact, rays are curves of stationary travel time and therefore depends on the slowness. So, slowness compares both in the integrand and it determines ray position  $r(s)$  in (1.22). Before of proceeding, we should linearize (1.22). For obtaining this result, we invoke Fermat 's principle which says that the travel along a ray does not change to first order when this ray is perturbed. We apply it to following equation:

$$|\nabla\mathbf{T}|^2 = \mathbf{s}^2(\mathbf{r}) \quad (1.23)$$

It is the *eikonal equation*, that is an equation which describes the propagation of a wavefront  $\mathbf{T}$  and its solution allows us to compute traveltimes. We consider a reference slowness  $s_0(\mathbf{r})$  that is perturbed by a perturbation  $\varepsilon s_1(\mathbf{r})$ , where the parameter  $\varepsilon$  serves to facilitate a systematic

perturbation approach. In this way, we have:

$$\mathbf{s}(\mathbf{r}) = \mathbf{s}_0(\mathbf{r}) + \epsilon \mathbf{s}_1(\mathbf{r}) \quad (1.24)$$

Applying this perturbation, we have a change in traveltime  $T$  and this last one can be written as:

$$T = T_0 + \epsilon T_1 + \epsilon^2 T_2 \quad (1.25)$$

Inserting (1.25) and (1.24) in (1.23) we have the following two equations:

$$|\nabla T_0|^2 = s_0^2(\mathbf{r}) \quad (1.26)$$

$$(\nabla T_0 \nabla T_1) = s_0 s_1 \quad (1.27)$$

(1.26) is the eikonal equation for the reference travel time. We symbolise with  $\mathbf{t}_0$  the unit vector directed along  $\nabla T_0$ . In this way, we can write:

$$\nabla T_0 = s_0 \mathbf{t}_0 \quad (1.28)$$

We multiply all two members of (1.28) with  $\mathbf{t}_0$ . In this way, we can write (1.28) as:

$$(dT_0/du_0) = s_0 \quad (1.29)$$

We can integrate (1.29) and therefore we obtain

$$T_0 = \int s_0(\mathbf{r}_0) du_0 \quad (1.30)$$

computed along  $r_0(s_0)$  where  $r_0$  is the position of the ray in the reference slowness field.

By means of (1.28), (1.27) can be written as:

$$(dT_1/du_1) = s_1 \quad (1.31)$$

Thereby, we can integrate (1.31) too and we obtain:

$$T_1 = \int s_1(\mathbf{r}_0) d\mathbf{u}_0 \quad (1.32)$$

Operating in this way, we have that the integration in (1.32) is along the reference ray  $r_0(s_0)$  rather than along the true ray in the perturbed medium. Thus, we have reached the goal of obtaining a linearized relation between the travel time perturbation  $T_1$  and the slowness perturbation  $s_1$ .

In the computational cases, we divide the area to investigate in cells where we assume that slowness perturbation is constant. In this way, (1.32) can be written in its discretized form:

$$\delta T_i = \sum_j l_{ij} s_j \quad (1.33)$$

In this form, the subscript  $i$  labels the different travel times that are used in the inversion while  $j$  is the cell index and  $l_{ij}$  is the length of ray  $i$  through cell  $j$ . If we label with  $n$  the number of cells, with  $m$  the number of observable data, we can obtain the  $n \times 1$  matrix  $s$  for the slowness, the  $m \times 1$  matrix  $t$  for the reference travel times and the  $m \times n$  matrix  $M$  for the

length of rays ( $l_{ij}$  is the element at  $i$ -th row and at  $j$ -th column of this matrix). Thus, equation (1.33) becomes:

$$\mathbf{Ms} = \mathbf{t} \quad (1.34)$$

The matrix  $M$  is in general very sparse for tomographic problems because every ray intersects only a small fraction of the cells.

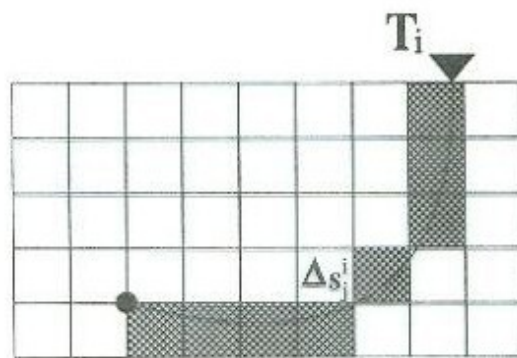


Figure 1.3: Graphical representation of discretization of velocity model

There are lots of numerical methods which allow to solve a seismic tomography. For example, for the forward problem there are the **MTTT (Minimum Travel Time Tree, Zhao et al., 2000)**, the **difference finite eikonal solver (Vidale 1988, Podvin & Lecomte 1990)** with this method which is often followed by a decoupling of velocity parameters by earthquakes localization parameters (**Pavlis & Booker, Spencer & Gubbins, 1980**), the **Fast Marching method (Sethan & Popovici, 1999, see Appendix 3)**.

There are various examples of 1-D velocity model (that is, a model which considers only variations of velocity of a specific seismic wave in relation

only to the depth and not to horizontal dimensions). Two of them are the most known and used. First, the **Jeffreys-Bullen model**, which, despite its age (it was developed by Harrold Jeffreys and Keith Bullen in 1940), is still used by relevant scientific agencies and organizations as **ISC (International Seismological Centre)** and **USGS (United States Geological Survey)**. Second, the **Ak135 model** (see Appendix 1) developed by **Kenneth & Engdahl** in 1995 improving their existing 1-D velocity model, **IASP91**. Ak135 has been conceived following the algorithm of **Buland & Chapman** for travel-time tables' elaboration. Other examples of 1-D velocity models are the **PREM (Preliminary Reference Earth Models, Dziewonski & Anderson, 1981)** and the **Herrin's 1-D velocity model (1968)**.

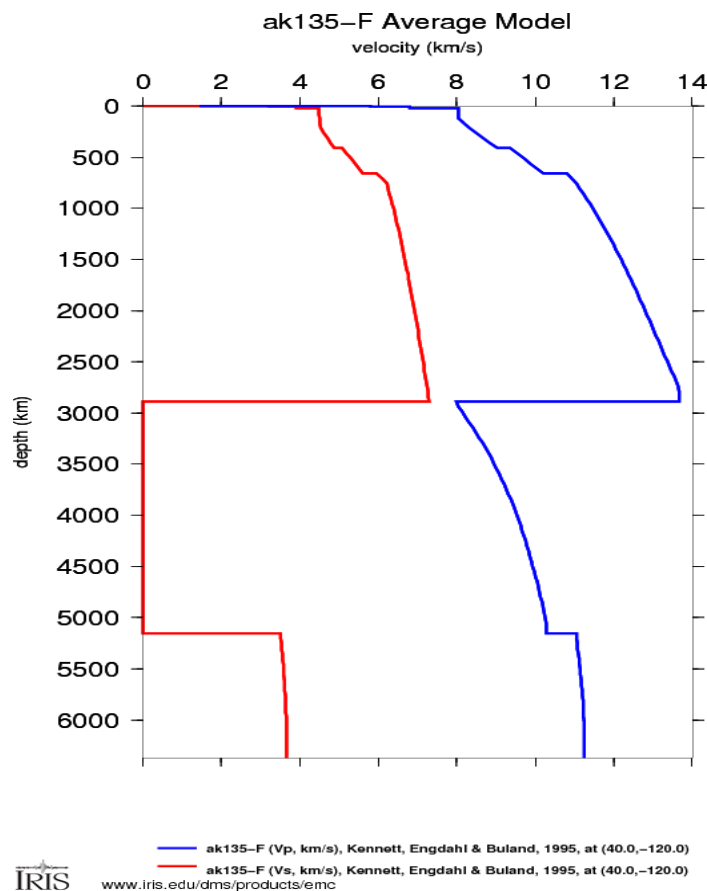


Figure 1.4: ak153 1D velocity model (blue for P waves, red for S waves)

Same critical mass of algorithms is for inverse problem. Most known and used one is **Least Squares**. This last one presents various versions. Most used are *Paige & Saunders'* one and **Damped Least Squares** (*Marquardt, 1970*). Other kind of algorithms are ART (algebraic reconstruction technique), Kaczmarz's algorithm, and conjugate gradient. In major part of these methods, the numerical technique of SVD (Singular Value Decomposition) is used to eliminate redundant values during the computation of inverse problems.

## 1.6 Methods to verify resolution of a seismic tomography

Seismic tomography is a numerical simulation and by means of it we want build a “simulation” of a subsoil of a determined reason. For this reason, it could be subject to statistical error and for each process of seismic tomography, we should implement a significant test to appreciate resolution. Two typologies of test are implemented for this goal:

***checkerboard test*** and ***velocity anomalies test***. Checkerboard sensitivity tests are useful to assess the ability of tomographic inversion to resolve structural details in the earth. In tomographic inversion, lack of an explicit inverse operator in the computational formulation makes it difficult to estimate parameter uncertainties and resolution for the inverted model. The checkerboard test is a useful alternative which gives a general picture of the resolving power of tomographic inversion. It can be applied to any inversion procedure without knowledge of the internal operation of the inversion.

The idea is to superimpose a small perturbation (typically a 3-D or 2-D regular "checkerboard" or grid pattern) signal onto the tomographically inverted structure model, compute synthetic travel times (data) to all observing stations from all sources used in the original tomographic inversion, and then invert the synthetic travel and arrival times in the same manner as the actual data. Random errors may added to the synthetic data to simulate random errors in the actual observations. The ability of the tomographic method to quantitatively recover the perturbed model is then an estimate of the sensitivity of the original inversion of real data to

recover similar details in the real earth.

There are obviously many factors that influence the results of a checkerboard test. These include such things as: the amplitude of the perturbation signal, whether the perturbation signal is a smooth variation such as a 2-D or 3-D sinusoid or a "square" wave (or other wave form), the size of the grid (or the spatial wavenumber) of the perturbation signal, whether variation is allowed in depth as well as in latitude and longitude, and whether the spatial wavenumber of the perturbation is the same in all three dimensions.

The second method is that of velocity anomalies. We produce a synthetic model fixed velocity anomalies in a set of vertical (or horizontal, if we want horizontal velocity anomalies) prisms limited by two depth levels. Using these prisms, we can create any complex 3-D pattern. We should modify in an opportune way shape and amplitude of these anomalies for obtaining maximum similarity with the real data inversion. This operation is performed iteratively by a trial and error method and it stops when the required similarity is retrieved. For describing in a better way this method, we assume that  $X_0$  is the real velocity distribution in the Earth. The rays travelling through this velocity anomaly produce the real data set  $D_0$ . Performing the inversion with a set of the free parameters  $S_0$  produces the resulting model  $X_1$ . Then, we create the synthetic model  $X_2$ , which is used to compute synthetic data  $D_2$ . After performing inversion for these data with the same set of the free parameters  $S_0$  as in the real data inversion, we obtain the model  $X_3$ , which is approximately equal to  $X_1$ . Since the inversion conditions are absolutely identical, we can assume  $X_0 \approx X_2$  and

thus we can proceed in an iterative way starting from  $X_2$  as previously written.

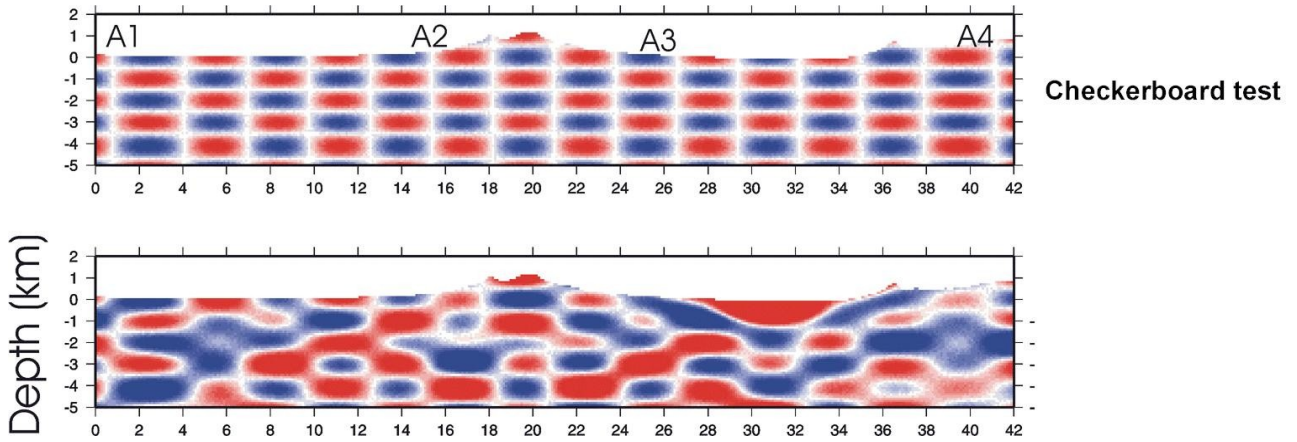


Figure 1.5: example of checkerboard test for a seismic tomography

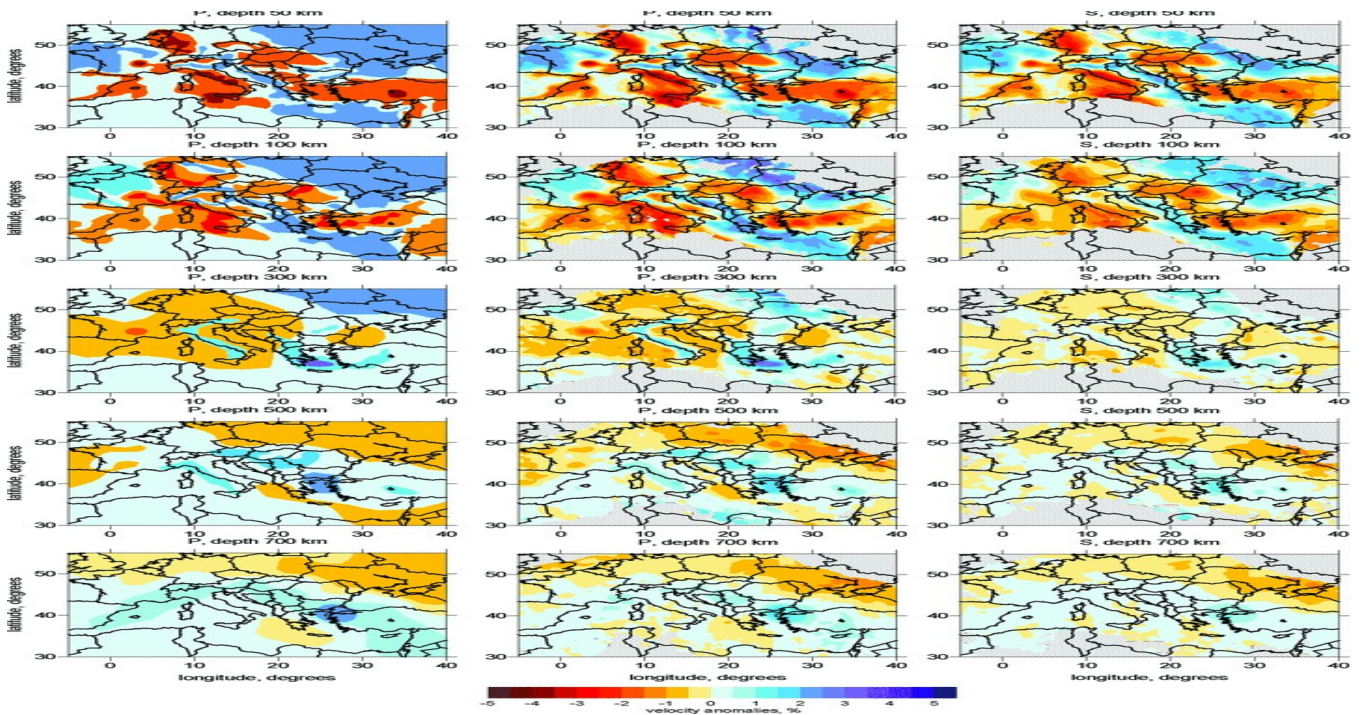


Figure 1.6: example of velocity anomalies test for a seismic tomography

## Chapter 2

### The phenomenon of subduction

#### 2.1 Plate tectonics: general description

Plate tectonics is the theory, powered by lots of observed data, which explains the evolution of the Earth's outer shell, the **lithosphere**, divided into several elements, the **plates**. They are subjected to a relative motion among each others. This fragmentation and this motion are the causes of actual Earth crust configuration, the earthquakes (above all) and of the formation of sedimentary basins containing majority of hydrocarbons. Defining this theory in a simple way, the plate tectonics represents the motion of a rigid and elastic lithosphere on a viscous fluid, the **asthenosphere**.

Lithosphere is Earth's outer shell and is composed by the Earth crust and the initial part of upper mantle. It could be divided in oceanic lithosphere and continental lithosphere. First's thickness ranges from 20 to 100 km and it has a density of 3-3,3 g/cm<sup>3</sup>. Second's thickness extends from 50 to 250 km and it has a density of 2,8-3,3 g/cm<sup>3</sup>. According to temperature, we can define its lower boundary by a specific isotherm at 1300°C. Although above 600°C some materials will begin to experience ductile deformation, defining the so-called **thermal lithosphere**.

Asthenosphere is the less viscous part of the upper mantle ( $10^{17} - 10^{19}$  Pa•s against  $10^{21}$  Pa•s). It has a thickness going from 100 to 400 km of depth and a density of 3,3 g/cm<sup>3</sup>. It is solid, but on geological time scales (10<sup>15</sup> s) it starts a behaviour like fluid. This happens because a little percent of

its components (1-3%) are partially molten. Evidence of this is the presence of a low velocity zone (where for velocity, we intend the velocity of seismic waves which are travelling through the internal of Earth, see chapter 3) that is included between 100 and 200 km of depth. This low velocity zone represents the so-called *décollement plain*, that is the point which controls dynamics of plates. Through the study of observed data, we can say that where the *décollement plain* is less viscous, the overlying plate moves faster than other.

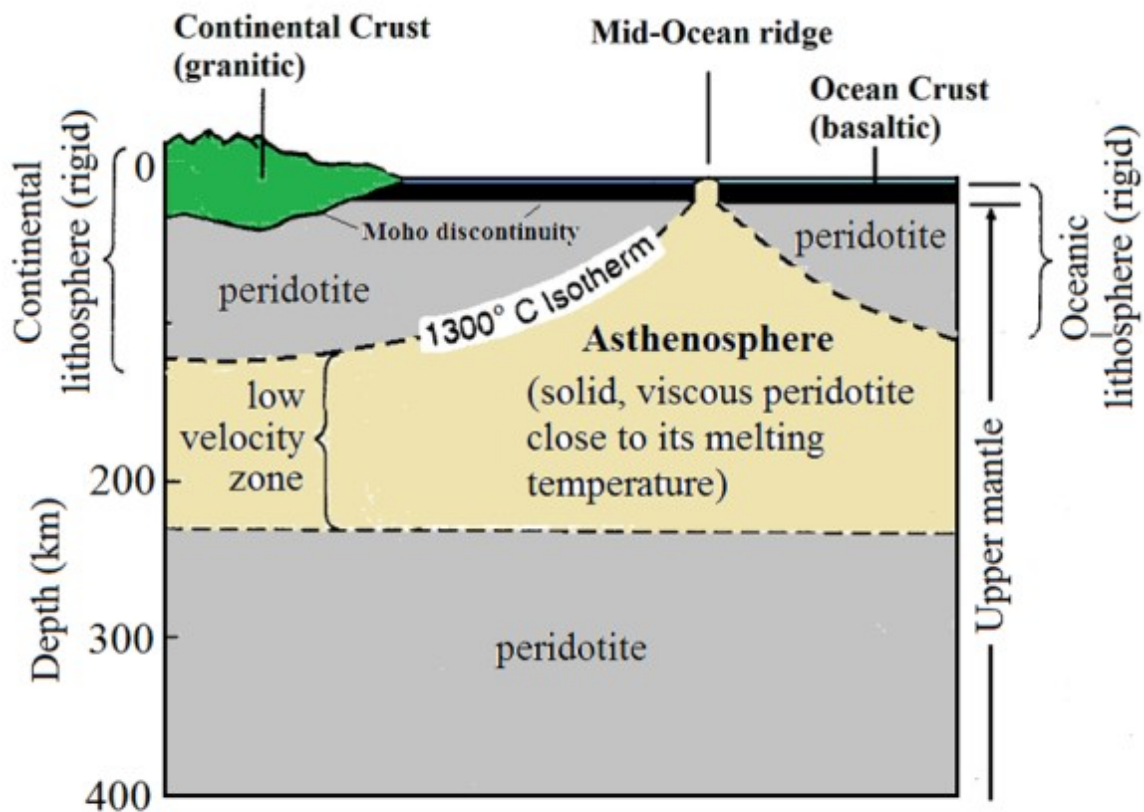


Figure 2.1: schematic stratigraphy of lithosphere and asthenosphere

The plates which compose the lithosphere are 12. In alphabetic order, they are: African, Antarctic, Arabian, Caribbean, Cocos, Eurasian, Indian, Nazca, North American, Pacific, Philippine and South American. But a great importance have the plate boundaries, because along them it is concentrated majority of Earth seismicity. This happens because movements of lithospheric plates involve shearing motions at the plate boundaries. Much of this motion occurs by aseismic creep, but shear-faulting earthquakes are also produced. The release of strain energy by seismic events is restricted to regions where there is an inhomogeneous stress environment and where material is sufficient strong for brittle failure. They are 14. In alphabetic order, Aleutian, Antilles, Central American, East Pacific Rise, Hindu Kush, Indonesian, Japan, Mariana, Mid Atlantic Rise, New Hebrides, San Andreas Fault, Scotia, South American, Tonga-Kermadec.

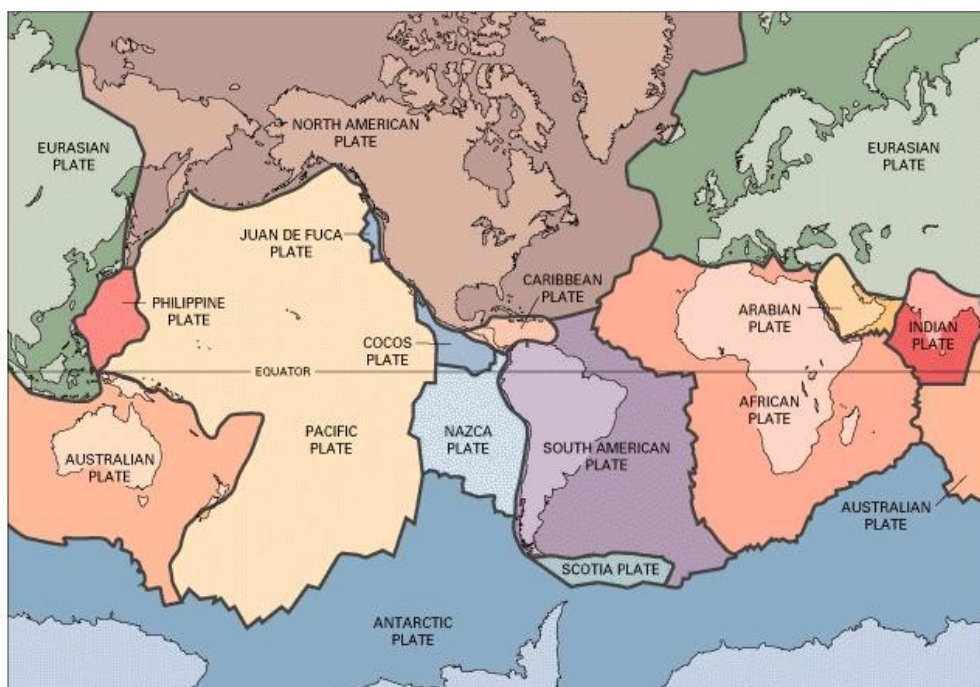


Figure 2.2: Illustration of plates which compose lithosphere

Three basic types of plate boundary are characterized by different modes of plate interaction:

- **Divergent boundaries**, where two plates are moving apart and new lithosphere is produced or old lithosphere is thinned. Mid-oceanic ridges and continental rifts are examples of divergent boundaries
- **Convergent boundaries**, where lithosphere is thickened or consumed by sinking into the mantle. **Subduction zones** and **alpine belts** are examples of convergent plate boundaries.
- **Transcurrent boundaries**, where plates move past one another without either convergence or divergence. **Transform faults** and other **strike-slip faults** are examples of transcurrent boundaries.

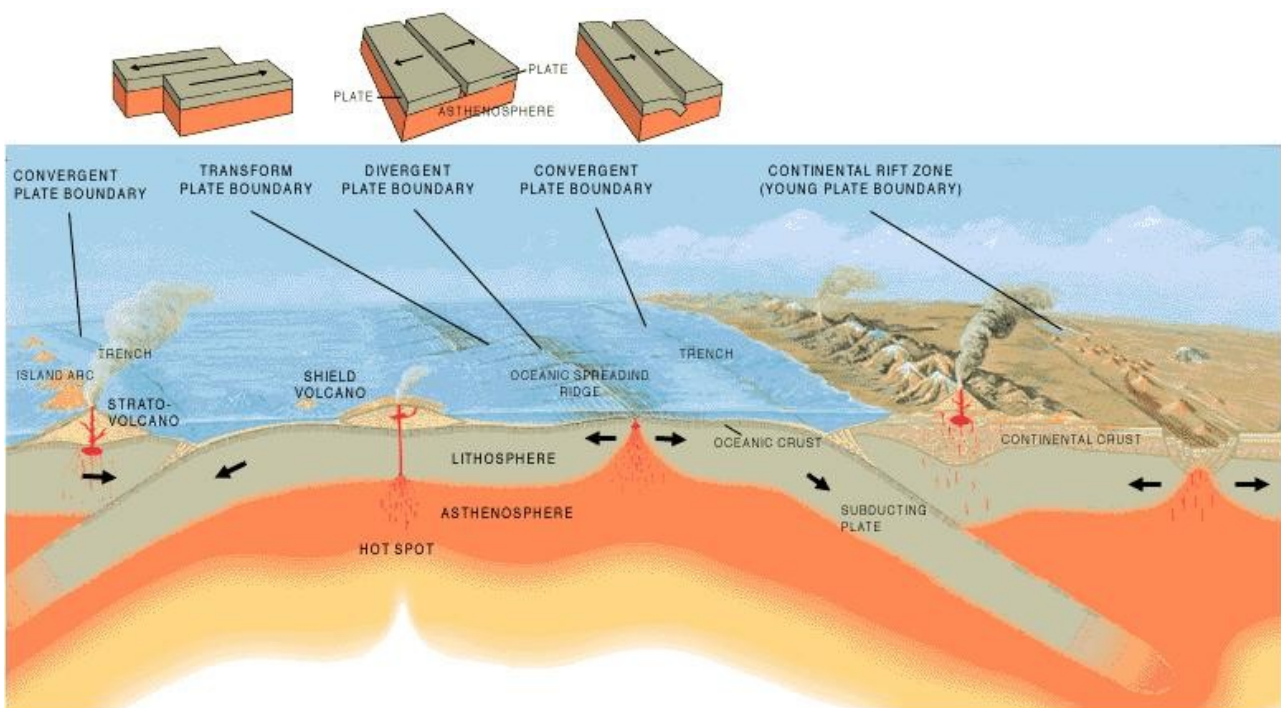


Figure 2.3: Cross section (by José F. Vigil from *This Dynamic Planet*) illustrating the main types of plate boundaries

In general, divergent and transcurrent plate boundaries are characterized by shallow seismicity (that is the maximum depth of earthquakes is less than 30 km). Instead, subduction zones and regions of continental collision have much deeper seismicity. For example, 80% of the world's seismicity is along the circum-Pacific margin and occurs mostly in subduction zones (see paragraph 2.3).

The kinematics of tectonics plates is based on *Euler's theorem* (see Appendix 2). This last one states that the relative motion of two plates can be described by a rotation about a pole (called an *Euler pole*). If a plate boundary is perpendicular to a small circle about the pole of rotation, convergence or divergence must be occurring between the plates. If the boundary is parallel to a small circle, the relative plate motion is transcurrent. The relative velocity between two plates depends on the proximity of a plate boundary to the pole of rotation. The rotation is described by an angular velocity  $\omega$ . As the distance to the boundary increases, the relative motion on a boundary also increases.

Several investigators have used the orientation of plate boundaries and relative velocities derived from the analysis to construct relative plate motions for the entire world. Absolute plate motions are more difficult to determine because the whole surface is in motion, but it is possible if one assumes a fixed hotspot or other reference frame. From observed data, we can obtain the result that plates do not move in a chaotic way, but they follow a global flux. The trend of this flux describes a sort of *tectonic equator*, that is an imaginary line which represents the motion of plates. This tectonic equator presents a sinusoidal form. From geodetical data

(especially GPS data), we can observe as there is a gradual change of direction of plates motion from WNW-ESE in Pacific to E-W in Atlantic. Then, tectonic equator gets back on a direction SW-NE through Africa, India and Europe. After, flux falls back again on Pacific. Major part of continental lithosphere (Eurasia) is concentrated where flux tends to flex towards Pacific. This results are valid in reference system **ITRF** (**International Terrestrial Reference Frame**). In this system, we assume that there is a no-net rotation of lithosphere compared to underlying Earth.

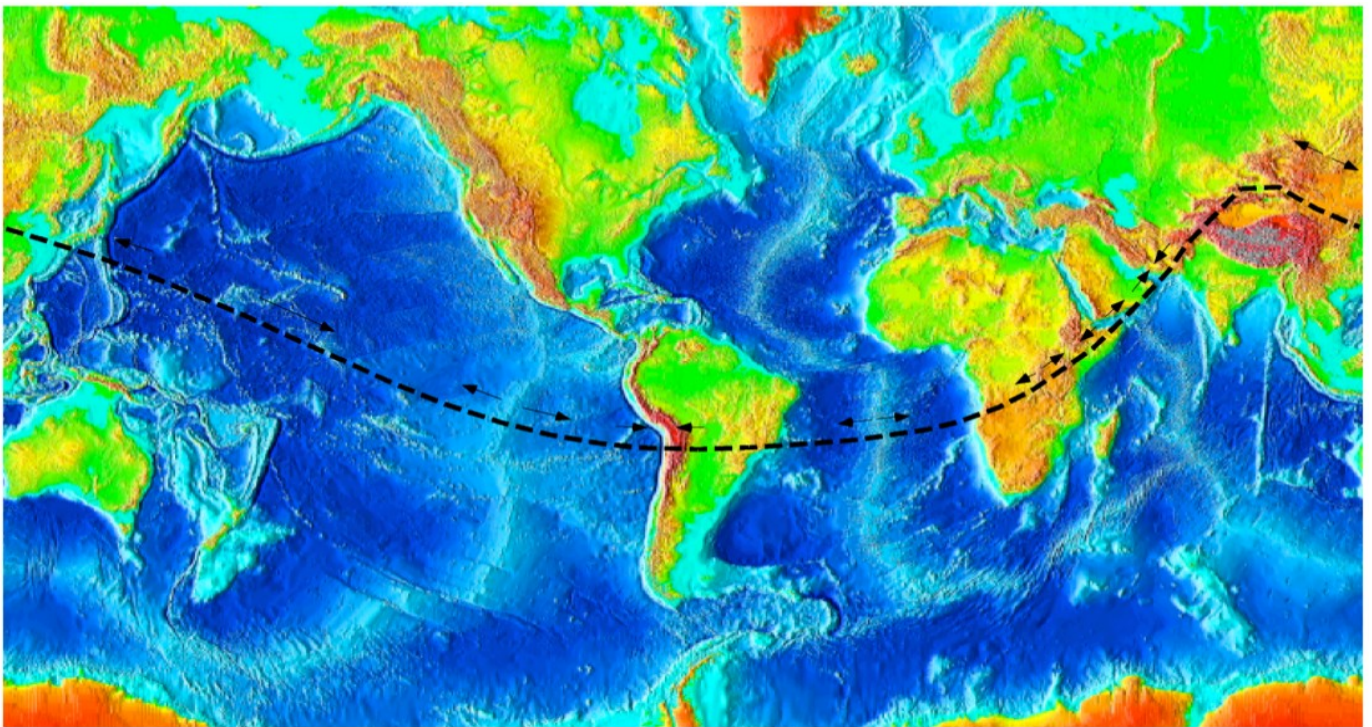


Figure 2.4: Morphological map National Geophysical Data Center. Dashed line represents the *tectonic equator*

Instead, if we consider other reference system as the so-called **hot spots** (they are magmatic manifestations which describe linear traces on Earth's surface, both underwater and subaerial, that rejuvenate going along a determined direction. These spots are presents both at boundaries like Iceland, Ascension and Tristan de Cuna and intraplate like Emperor-Hawaii), we can observe a net rotation of lithosphere compared to mantle, orientated towards West on average. This is evident if we consider velocity of Pacific plate towards WNW. It is so high that the sum of movements of all other plates is not able to compensate for it, provoking a residual of motion towards West.

Plates movements is faster in equatorial and tropical belts. Plates flux and its polarization towards West, combined with the high plates velocities at low latitudes, suggest that plate tectonics is influenced by Earth rotation. Dynamics of plates is influeced by four factors: the pulling made by mantle's convective movements, the **ridge push** (due to ridges' weight), the **slab pull** (due to subduction zones, see paragraph 2.2 and 2.5) and the Earth rotation. We now describe the first and the last factor. We know that mantle has a behaviour like fluid on geological time scales ( $10^{15}$  s) and we know that a fluid which is cooled on its top and is heated up on its bottom can transfer heat or by means of conduction or by means of convection. This last one is regulated by adimensional quantity, called **number of Rayleigh (Ra)**, which is given by:

$$\mathbf{Ra} = (\rho^2 g c_p \alpha (T_1 - T_0) h^3) / \mu \kappa \quad (2.1)$$

where  $\rho$  is the density,  $c_p$  is the heat capacity,  $\alpha$  is the coefficient of thermal

expansion,  $\mu$  is the viscosity,  $\kappa$  the thermal diffusivity,  $g$  the gravitational acceleration and  $T_1 - T_0$  the difference of temperature. If  $Ra$  is high, we have convection. If it is low, we have conduction. Mantle (its heat is due for 90% to inner radioactive decay and only for 10% for transfer from core) starts to be convective when  $Ra$  is equal to  $9 \times 10^6$ . Upper mantle is the most convective part. This happens because it is less viscous than lower mantle and it has a high thermal gradient respect to lower mantle. But the convection has an intrinsic lack, that is the assumption to have a mantle which is homogenous in its composition. Obviously, this situation is not real otherwise we should verify the presence of pieces of lithospheric mantle which fall down into astenospheric mantle, provoking a raising of lithosphere for effect of isostasy. Other conflict due to this evidence is that in convection models, we should have stationary convective current flows both upwards and downwards, but plates boundaries, rifting zones, subductions zones and transform zones obviously migrate. Then, all convection models divide the inner Earth in polygonal cells, but real plates boundaries have a linear form (for example, the Atlantic ridge). Therefore, convection of mantle is not the real because of a mantle drag. Other evidences are the movement of Hawaii hot spot in direction ESE respect to underlying lithosphere. Atlantic and Indian ridges were distanced from Africa during their formation, therefore there is a relative motion between them. This evidence underlines as a raising of mantle which should occur in a fixed distance between two ridges is not compatible with plates kinematics. A lateral motion of ridges explains why these last one are fed by a fertile mantle, situation which is not possible if

we assume a static configuration. By means of several seismic tomographies, we can observe the presence of two big areas where we can hypothesize a raising of lower mantle (that is, two big low velocity zones). They are in Central Pacific and in Central-Southern Africa (**Romanowicz & Yuancheng, 2002**). Seismic tomographies have also confirmed the presence of low velocity zones under oceanic ridges at a depth between 100 and 200 km. They should symbolize a partial fusion of upper mantle, while underlying mantle has greater seismic velocities. This result suggests the occurrence of a cold mantle and the fact that there is not a deep supply for the ridges.

The polarization towards West of lithosphere respect to mantle highlights as Earth's rotation give a strong contribution to plate tectonics both on their direction of motion and energy. In fact, this polarization is caused by luni-solar attraction on Earth. This last one provokes tides (both fluid ones and solid ones) and slows down the velocity of rotation (during of day grows up at a rate of 1,79 ms/century, **Denis, 2002**). We know that consolidation of Earth's inner core started 500 Ma and we already know that inner mantle presents an accumulation of denser material in its lower parts that cannot raise because of high pressure at which it is exposed at a depth of 2800-2900 km. Therefore, it means that in lower parts of core and of mantle there are heavy materials that contribute to drop the moment of inertia of Earth's rotation. The consequence of this is an increase of velocity of rotation, although this increase is not enough to compensate the slowing imposed by tides. The combination of tidal effects and of downgoing of denser material produce a couple of forces on asthenosphere.

The poor resistance of this layer could explain the motion of lithosphere towards West. In this model, plate tectonics should be a combination of rotational effects and mantle's convective motions (*Scoppola et al., 2004*). The importance of the rotational effects could increase if the theory that affirm that majority of terrestrial magmas come from the asthenosphere. If this theory were confirmed, then we could not have direct petrological informations on the composition of not-asthenospheric mantle. Thus, this last one should be richer in iron and denser. In this way, only convective effects (for example, slab pull, see paragraph 2.2 and 2.5) are not able to activate alone plate tectonics and therefore a contribution of astronomical effects should be very relevant.

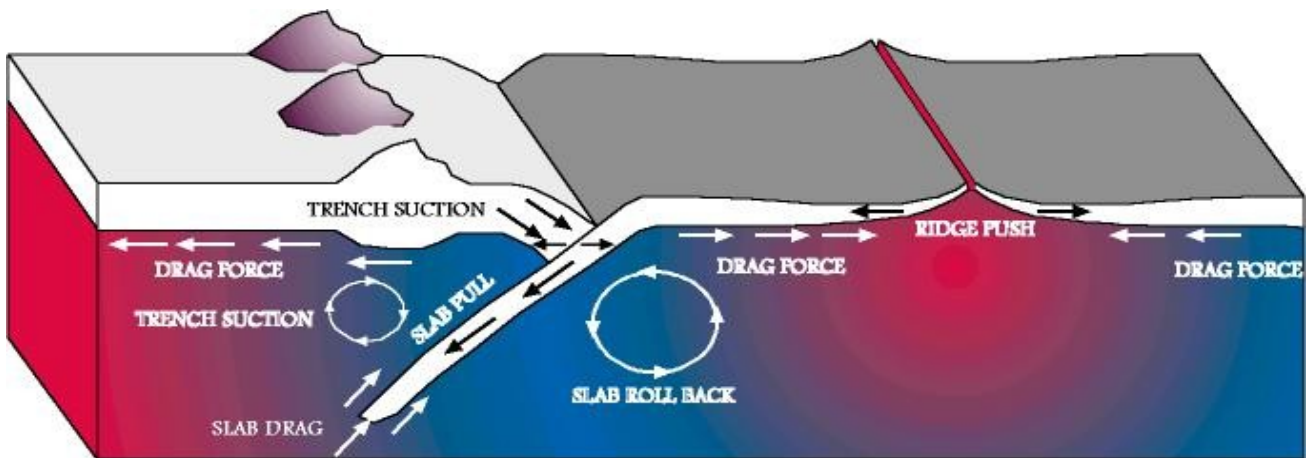


Figure 2.4: Forces acting on lithosphere

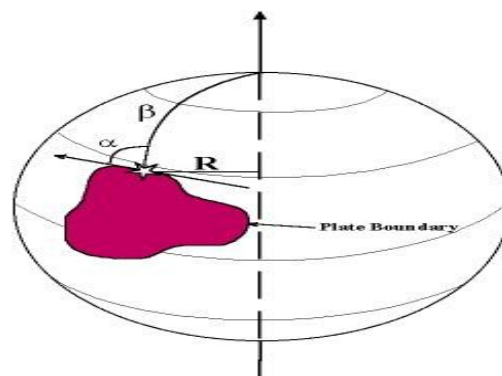


Figure 2.5: Effects of Earth's rotation on lithosphere

## 2.2 Subduction – qualitative description

As affirmed in previous paragraph, there are two types of convergent boundaries, subduction zones and continent-continent collision zones. These last ones are rare (although extremely important for producing major mountain ranges and plateaus). Currently, more than 90% of the world's convergent boundaries are subduction zones, which form at zones of oceanic-oceanic or oceanic-continental convergence. Convergence at these boundaries is accommodated by underthrusting of one lithospheric plate beneath another. The underthrust plate descends through the asthenosphere and represents “consumed” lithosphere, which balances the surface area of new lithosphere created at mid-oceanic ridges. Subduction of the lithosphere is one of the most important phenomena in global tectonics; no oceanic crust older than Jurassic (~ 200 million years) exists, yet we find continental crust 20 times as old. Summing the area of ocean floor that has opened since Jurassic time, we find that 20 billion km<sup>3</sup> of material has been subducted. At the present, based on the rate of subduction, an area equal to the entire surface of the Earth will be cycled into the interior in 160 million years. We briefly describe that two kinds of subduction zones previously introduced. a) We start from oceanic-oceanic collision. The characteristics of this kind of subduction were studied first by H. Benioff in the 40s. It is the most widespread kind of subduction in actual geodynamics situation. The subsidence gets involved the portion of lithospheric mantle of plate (that is chemically homogenous at underlying asthenospheric mantle) while rocks that construct the lithospheric crust start

to accumulate and a mountain chain taking shape: this structure is a so-called **accretionary wedge**. Near flexure line of subducting plate, an oceanic trench is building. It is parallel to arc of volcanic islands formed by upward raising of materials which derive from elaboration of subducting ones. Typical examples of this type of subduction are the Pacific island arc (Philippine, Japan, Marianna, Tonga). A little variation of this kind of subduction is the so-called **roll-back subduction** or **passive subduction**. In this particular case, we have not a real convergence between two plates in collision, but simply one of them starts to sink in an autonome way.

The reasons are not clear yet. Probably, the most relevant cause of this effect is that sinking of a plate happens because of its excessive weight. Then, plate starts to retrait carrying out an action of swallowing and consequent stretching with regard to other plate. The Southern Tyrrhenian, which will describe in Chapter 4, is a result of a roll-back subduction.

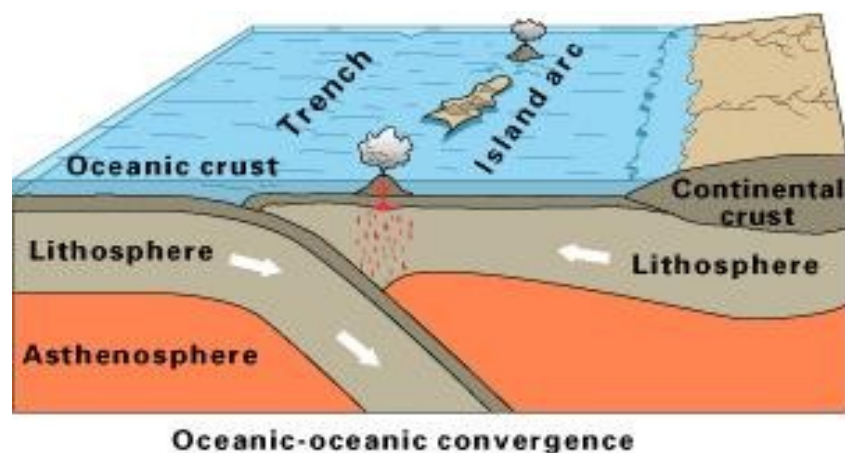


Figure 2.6: Illustration of oceanic-oceanic convergence

b) For oceanic-continental convergence, we consider if, for example, we could pull a plug and drain the Pacific Ocean. We would see a number of long narrow, curving trenches thousands of kilometers long and 8 to 10 km deep cutting into the ocean floor. Trenches are the deepest parts of the ocean floor and are created by subduction. Off the coast of the South America along the Peru-Chile trench, the oceanic Nazca Plate is pushing into and being subducted under the continental part of the South American Plate. In turn, the overriding South American Plate is being lifted up, creating the towering Andes mountains, that are the accretionary wedge of this subduction. Oceanic-continental convergence also sustains many of Earth's active volcanoes, such as those in the Andes and the Cascade Range in the Pacific Northwest. The eruptive activity is clearly associated with subduction, but scientists debate the possible sources of magma. There are two options in for a pound. First, magma could be generated by the partial melting of the subducted oceanic slab. Second, magma could be generated by the partial melting of the overlying continental lithosphere. Actually, the Earth's present subduction zones are consuming oceanic lithosphere of all ages, but the thermal buoyancy force in old, cold lithosphere is much larger than in young, warm lithosphere. Once subduction has started in a given zone, **ridge push**, that is the body force due to the cooling and sinking of lithosphere away from spreading centers, will help push the subducted plate into the asthenosphere. If the subducting plate is old lithosphere and the rate of convergence at the subduction zone is low, the negative buoyancy force is the dominant force acting on the plate and the plate will sink under its own weight, originating

the so-called *slab pull*. On the other hand, if the subducting plate is old but the rate of convergence is very high, the subducting plate is being pushed into the mantle faster than it would sink on its own. This is known as *forced subduction*. In the delicate balance between forced subduction and slab pull, the slab is neither strongly in compression nor in tension. This allows the residual stress field, which is much smaller than typical subduction stresses, to control the seismicity (see paragraph 2.3).

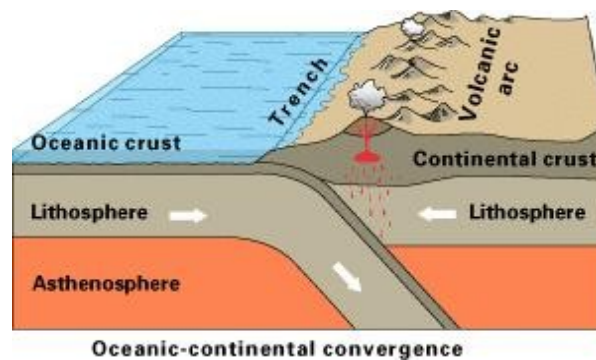


Figure 2.7: Illustration of oceanic-continental convergence

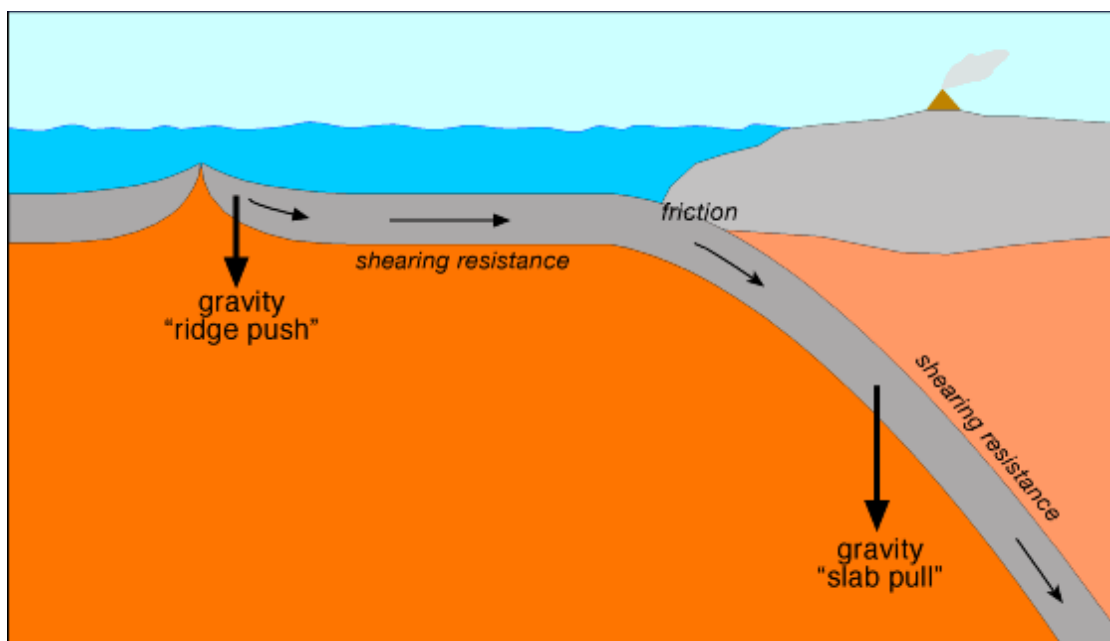


Figure 2.8: Illustration of "ridge push" and of "slab pull"

### 2.3 The slab seismicity in subduction zones

In subduction zones, there are three categories of seismic activity that we can individuate. They are:

- **Slab seismicity**, that is the seismicity related to the internal deformation of the overriding plate commonly associated with back-arc extension or upper-plate compression
- **Interplate seismicity**, that is the seismicity which happens between two converging lithospheric plates when a large contact zone occurs. Seismicity is caused by the frictional sliding between them
- **Intraplate seismicity**, that is the seismicity connected to internal deformation within the subducting plate that results from the slab's interaction with surrounding mantle

Among these three categories, first is that more described for the simple reason that slab seismicity is the principal source of entire world seismicity. History of study of slab seismicity starts in the early 1930s, when K. Wadati observed for first time deep zones of seismicity beneath Japan. With the advent of plate tectonics, these zones were recognized as an expression of the Pacific plate subducting beneath the Eurasian plate. H. Benioff detailed the occurrence of deep seismicity zone in many regions of the world in the 1940s, and we now refer to these deep seismic belts as **Wadati-Benioff zones**. Therefore, hypocenters of earthquakes are localized along these Wadati-Benioff zones and, according to their depth, we can

classificate them in four categories. They are:

- **Superficial earthquakes**, that occur in the range of depth 0-200 km
- **Intermediate earthquakes**, that occur in the range of depth 200-400 km
- **Deep focus earthquakes**, that occur in the range of depth 400-600 km
- **Lower mantle earthquakes**, that occur in the range of depth 600-700 km

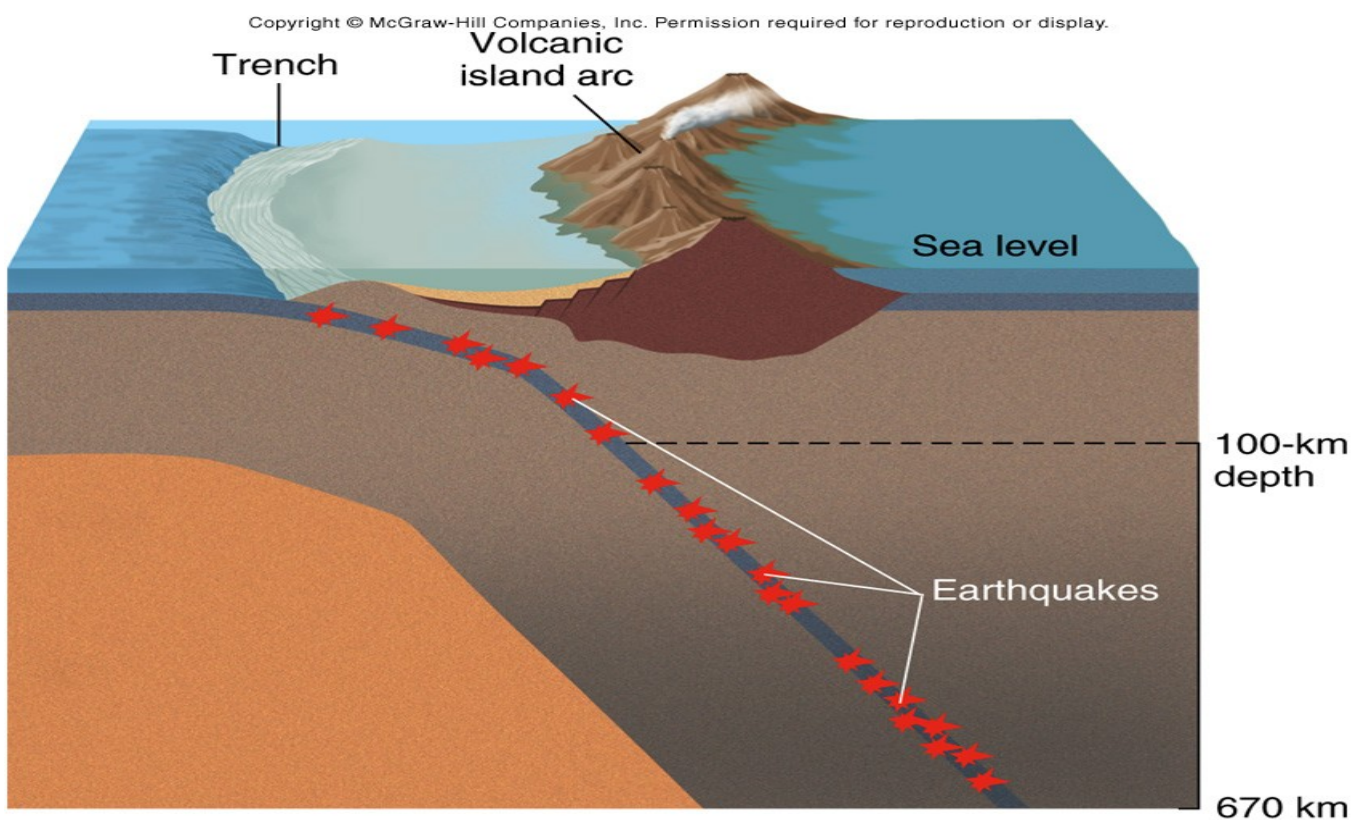
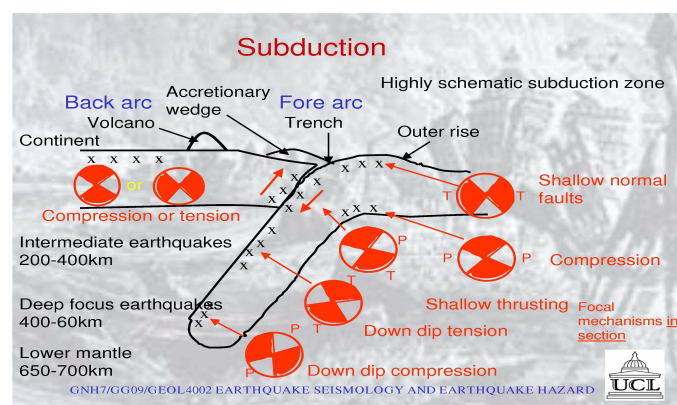


Figure 2.9: Illustration of a Wadati-Benioff zone with earthquakes distributed along a subduction slab

The state of stress in a subducting plate depends on the balance of two forces, the negative buoyancy of the descending slab and the resistance force of mantle that is being displaced by the subducting plate. These forces depend strongly on the viscosity structure, phase transformations in the slab, the rate of subduction, the age of the subduction zone, and the depth of slab penetration. The largest number of earthquakes are superficial and in the first 200 km of depth there is the largest energy release. The dominating process in this range of depth is normal frictional sliding between two plates. Below about 50 km all events are within the plate rather than on the plate interface. The earthquake activity is at a minimum between 200 and 400 km depth (intermediate earthquakes range), where the subducting lithosphere is interacting with weak asthenosphere. Frictional sliding may occur at these depths only if hydrous phases destabilize and release water or other fluids to allow high pore pressures to exist. Below 400 km (deep focus earthquakes range), the number of earthquakes increases with depth and some slabs strongly distort. Increasing resistance to slab penetration is often inferred, but frictional sliding mechanisms are generally not expected at these depths (unless further hydrous phases exist at these depths and release fluids as they destabilize), thus other mechanisms such as phase changes may be operating. All earthquakes activity ceases by a depth of 700 km. Some of the largest deep events are found near the maximum depth of seismicity in different slabs, thereby there is not a simple tapering off of activity. This maximum depth is conspicuously consistent with the velocity discontinuity near 660 km depth. A phase change in the slab may occur that suppresses

earthquake failure. The termination of seismicity is a first-order observation of the fate of the subducted slab, but its implication is controversial, because an aseismic slab extension may exist in the lower mantle (see paragraph 2.4). The focal mechanisms of the earthquakes along the Wadati-Benioff zone can be used to map the stress orientation in the slab. The stress orientation is controlled by the slab geometry and the balance of thermal, resistive, and negative buoyancy forces. If negative buoyancy dominates, the slab will be in downdip extension and the T axis as determined from the earthquakes will be parallel to the dip of the slab. As the resistive force becomes more important, the slab experiences downdip compression, and the P axis will be parallel to the trend of the Wadati-Benioff zone. To understand this phenomenon, consider a long rod held against the force of gravity. If the rod is supported at the top, the rod will be in extension. If the rod is supported at the bottom, its own weight will cause the rod to be in compression. If the rod is partially supported at the top of the bottom, the state of stress is transitional.



**Figure 2.10: Description of the slab seismicity**

This model was developed by Isacks & Molnar in 1971. They recognized a corresponding range of behavior in subducting slabs by examining numerous subduction zones. Even if it is to necessary explaining that there are some subduction zones which show a very interesting variation at depths of 50 to 200 km. The most interesting case is Japan, and in particular northern Japan. In this area, we have a **double** Wadati-Benioff zone. In this region, there are two planes have earthquakes with different focal mechanisms. The upper plane is predominantly in downdip compression, while the lower plane is in downdip extension.

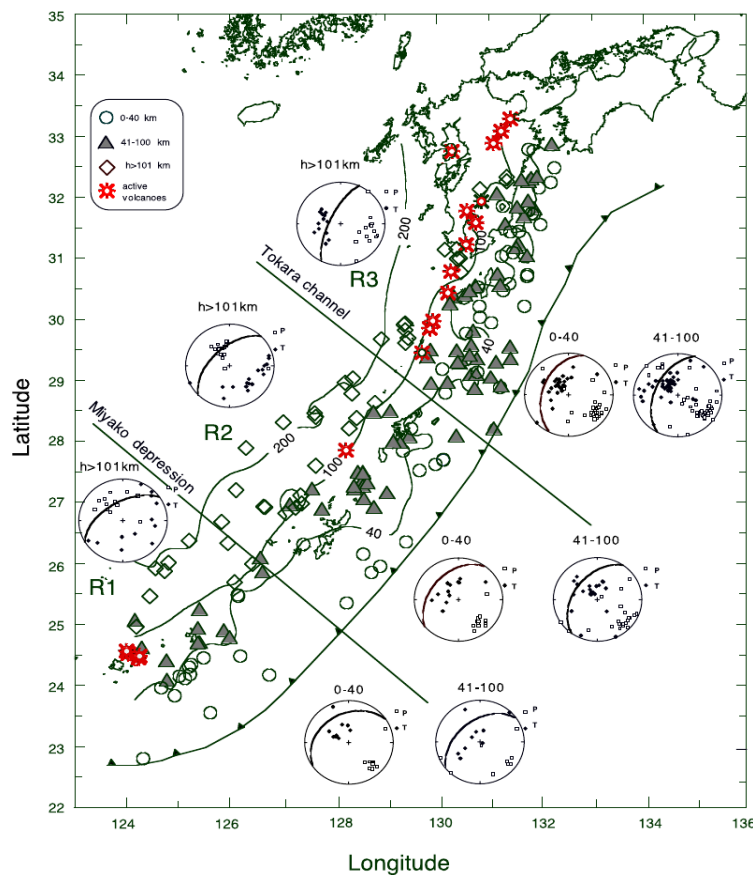


Figure 2.11: Illustration of earthquakes and of focal mechanisms in double Northern Japan Wadati-Benioff zones

There are several proposed models to explain double Wadati-Benioff zones that involve the unbending/bending of the plate and thermal stresses. In one model, bending a thin plate causes extension in the outer arc of the bend, while the underside of the plate is in compression. The extensional zone is separated from the compressional zone by a neutral surface. Shallow tensional events and deep compressional events are, in fact, observed in the outer rise of subduction zones. If the plate is suddenly released from the torquing force, it will “unbend” and experience forces opposite to those imposed during bending. This could explain the double Benioff zone stresses at intermediate depth. A second type of model for the double seismicity is based on a “sagging” force. This model affirms that if a plate sinks into the mantle at a shallow angle and if the leading edge of this subduction zone is supported, the middle may sag under its own weight.

The earthquakes in double Wadati-Benioff zones are small, rarely exceeding magnitude 5.5. Double Wadati-Benioff zones are not observed everywhere and are probably related to a balance between thermal buoyancy and rate of subduction.

Regarding to shallow seismicity in subduction zones, it marks the interaction of the subducting and overriding lithospheres and accounts for 70% of the annual global seismic energy release. Nearly all great earthquakes (magnitude > 8.0) occur in this region. Focal mechanisms of earthquakes from this region are typically shallow-dipping (15°-30°) thrust events. The variations between subduction zones in terms of maximum earthquake size and rupture length is remarkable. If we extend the concept

of asperity (that is a protusion on the fault surface that have locally high stress drops) to subduction zones, we are able to introduce the concept of ***coupling***, which is a measure of the seismogenic mechanical interaction between the subducting and overriding lithospheric plates. We can observe as a strongly coupled subduction zone will have a greater portion of its interface covered by asperities compared with less coupled zones. The motivation for this model of asperity coupling comes from the complexity of source time functions for large thrust events and the size of the fault zone inferred from aftershocks and surface-wave models of the source finiteness.

According to relative size of the asperities, we can divide the subduction zones into 4 categories (***Lay & Kanamori, 1981***). They are the following:

- ***Category 1***, where great earthquakes tend to occur regularly in time over approximately the same rupture zone (example Southern Chile)
- ***Category 2***, subduction zones with smaller rupture dimensions (example central portion of the Aleutian subduction zone)
- ***Category 3***, large earthquakes from repeated ruptures of the same portion of the subduction zone, which produces large earthquakes from repeated ruptures of the same portion of the subduction zone. However, it seldom fails simultaneously to generate larger events (example Kuril Islands subduction zone)
- ***Category 4***, absence of great earthquakes with a large component of aseismic slip (example Marianne subduction zone)

A number of factors, such as age of lithosphere, contribute to coupling. There is a relation between the maximum moment magnitude  $M_w$  event in a given zone, the convergence rate and the age of the subducted lithosphere (*Ruff & Kanamori, 1980*). It is:

$$M_w = -0.00889T + 0.134V + 7.96 \quad (2.2)$$

where  $T$  is the age of the subducted plate in millions of years and  $V$  is the convergence rate in cm/yr.

Equation (2.2) can also be used to predict the size of an earthquake expected in a subduction zone. For example, the Cascadia subduction zone along the coast of the Pacific Northwest (Oregon and Washington) is historically quiescent. However, the convergence rate between North America and the Juan de Fuca plate, along with the young age of the Juan de Fuca plate, suggests that a magnitude 9+ event is credible.

The nature of coupling on the shallow thrust plane in subduction zones appears to be influenced by the history of the subduction zones. An evolutionary subduction model was proposed by Kanamori in 1977. This model affirms that shallow-dipping, broad, strongly coupled zones (for example, Alaska) produce extensive ruptures. The thrust zone may be weakened and partially decoupled by repeated fracturing, yielding smaller rupture lengths and asperities. Large normal-faulting events that fracture the descending lithosphere represent a transition to tensional stress in the slab and complete decoupling of the plate interface. This phenomenon may result in the development of a back-arc (see chapter 4) basin by trench

retreat. These ideas about seismic coupling are very qualitative, and the actual frictional properties on the thrust faults are undoubtedly further complicated by the history of prior slip, hydrological variations, and thermal regime of the plate interface. The notion of asperities is useful primarily as a qualitative characterization of the stress heterogeneity, not as a model for dynamic slip processes.

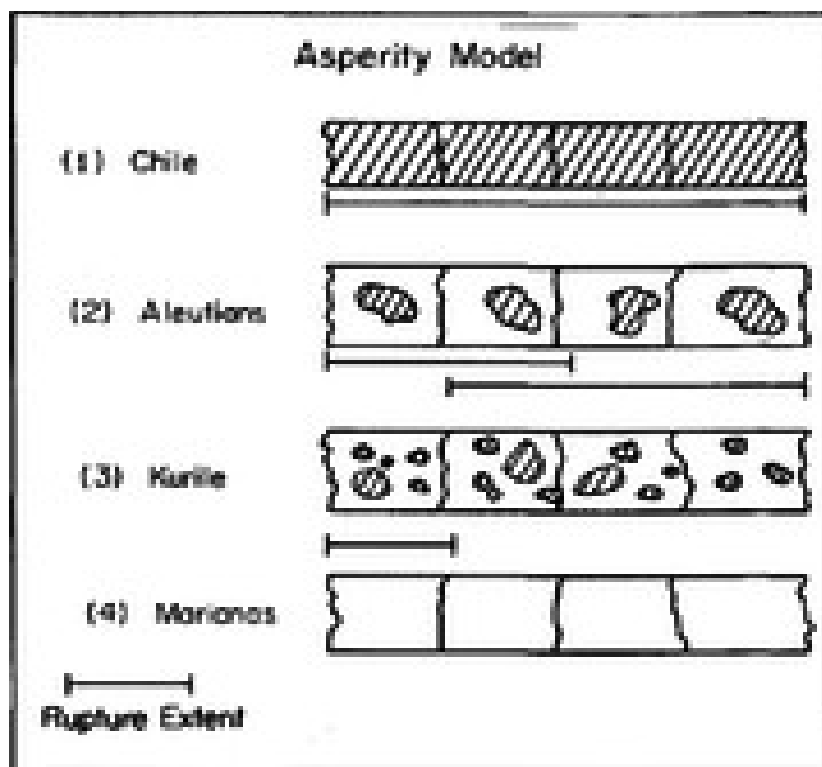


Figure 2.12: Schematic diagram of the asperity model for stress heterogeneity on the fault plane (Lay & Kanamori, 1981)

## 2.4 Ideas about the fate of a subducting slab and individuation of a slab in a seismic tomography

All the observations in seismicity indicate that the maximum depth at which earthquakes occur is about 670 km. Geophysicists associate this value at a boundary between upper and lower mantle and a big issue in scientific community is solving the problem about the fate of a subducting slab at this depth. That is, slab arrests at this depth or it is able to penetrate in lower mantle? And, if the answer to second question is “yes”, in which way does it penetrate? There are several hypothesis in relation to this topic. We can resume them in two theories. In the first theory, the 670-km discontinuity is viewed as impenetrable to subduction. When the slab encounters the boundary, it must flatten out, although it may depress the discontinuity. There are two options about the creation of this “strong” boundary. First one affirms that the 670-km discontinuity may be a boundary between chemically distinct lower and upper mantles. The lower mantle must have a composition with a high enough density to exceed the thermally induced density anomaly and inertial effects of the slab. Second one claims that the viscosity across the boundary may increase by more than several orders of magnitude, enough to prevent penetration. The existence of strong viscous or compositional stratification would cause mantle convection to be separated into upper and lower mantle convective regimes.

The second theory is that the 670-km discontinuity is a phase change, with conversions to high-pressure perovskite being expected at this depth.

Although viscosity may increase at this transition, the slab can usually penetrate the slab boundary, with seismicity terminating as the phase transformations occurs. Most geophysicists agree that the seismic boundary is such a phase change, but controversy still exists over whether any compositional change also occurs. By means of seismic tomographies, several studies have been elaborated to solve this controversy. Even if the opinion remain discordant. For example, Isacks & Molnar (1971), Zhou & Anderson (1989), Shearer & Mastner (1992) are in agreement with first theory, even if they supply different explanations about the “block” of subducting slab at 670 km. Instead, other scientists are in agreement with second theory. For example, Van der Hilst et al. (1991) showed that slabs beneath the northern Kuril and Marianne arcs may sink into the lower mantle. Slab deflection and penetration exist at different times in convection models characterized by an endothermic phase change in a chemically homogeneous mantle. The negative Clayeron slope of the phase change near the 670 km depth may preclude slabs from sinking easily, and undeformed, into the lower mantle. Summarising, we can affirm that slab could penetrate into the lower mantle but it depends on the chemical and physical properties of the individual slab. Some slabs appear to deflect and broaden at the 670-km discontinuity, while others appear to penetrate at least a few hundred kilometers.

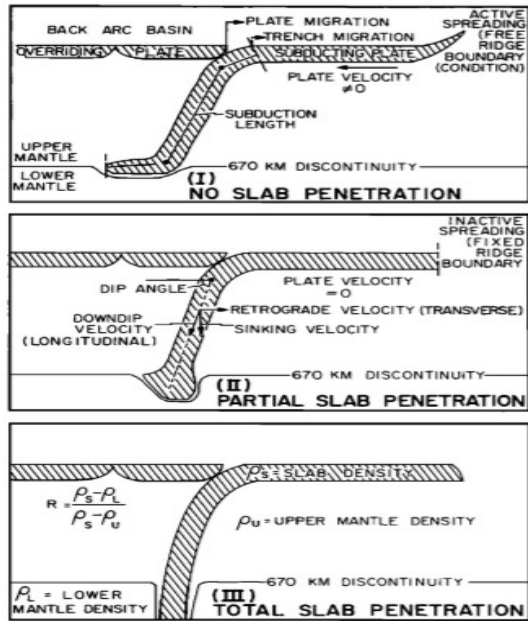


Figure 2.13: Description of fate of subducting slab according to Kincaid & Olson, 1987

Geophysicists are in perfect agreement among them about the role and the importance of seismic tomography to determine nature of subducting slab. It is extensively used to investigate upper-mantle structure beneath subduction zones, where old oceanic lithosphere sinks into the mantle. For over 25 years, seismic observations have revealed that the sinking tabular structure of the plate provides a high velocity, low-attenuation (high-Q) zone through which waves can propagate upward or downward through the mantle. Seismologists have expended extensive effort to determine properties of both the slab and the overlying mantle wedge. The arc volcanism overlying the cold slab is clearly associated with anomalous properties of the wedge, as has been known for several decades. Localized regions of very slow shear velocities and strong attenuation indicate partial melting in the mantle above the slab. The locations of anomalous zones have been constrained mainly by using phases (both local and teleseismic) from intermediate and deep-focus events.

Up until the mid-1970s subducting slabs were always shown as cartoons, geometrically constrained by the intraplate earthquake locations in Benioff zone. However, as vast numbers of body-wave travel times began to accumulate, making possible to develop tomographic images of the subducting high-velocity slab without a priori constraints. In developing velocity models, it should be necessary to implement relocation of sources (in case of passive local seismic tomography, see paragraph 1.5) by means of three-dimensional ray-tracing. This happens because the strong velocity anomalies can significantly deflect the raypath. Stable solution of the nonlinear inversion for structure and source location when raypath

perturbations must be included is a current area of active research in seismic tomography.

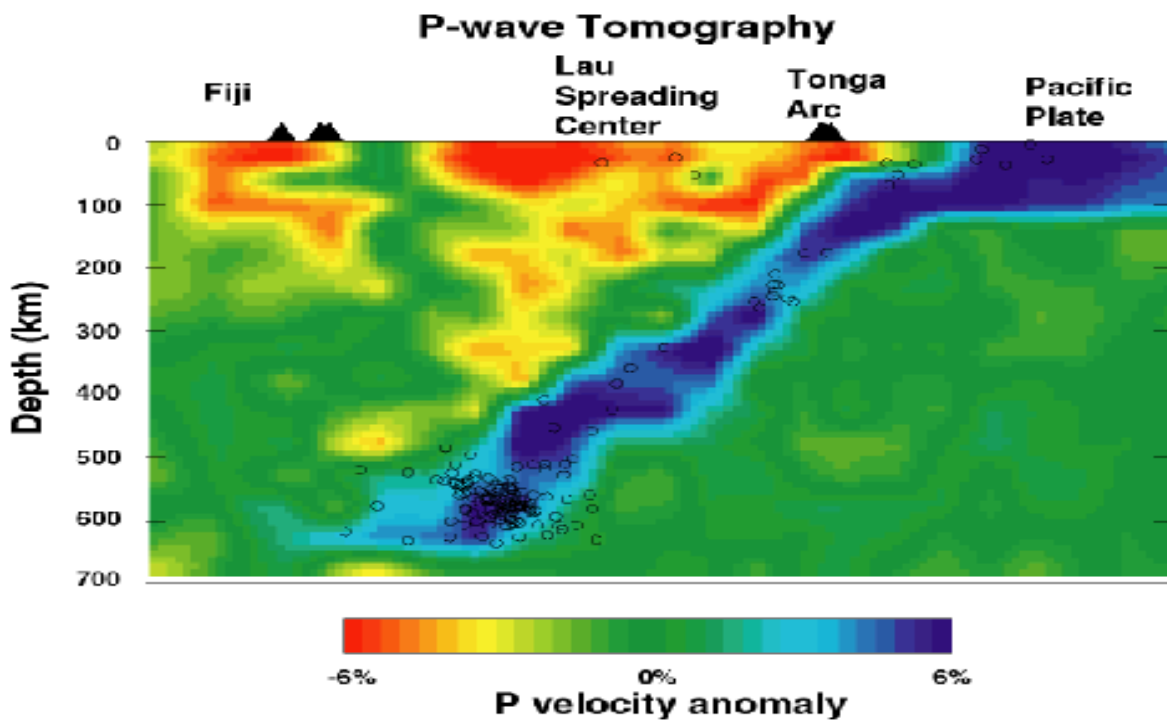


Figure 2.14: Example of seismic tomography which highlights the presence of Kermadec-Tonga subduction zone (Wiens & Smith, 2003)

## 2.5 Mathematical treatment of a subducting lithosphere

In paragraph 2.1, we affirm that the plate tectonics represents the motion of a rigid and elastic lithosphere on a viscous fluid, the asthenosphere. Thus, we can describe a subducting lithosphere in asthenosphere in a mathematic way by means of equation of a flexure of an elastic lamina.

We consider a horizontal (almost initially) homogenous lamina with thickness  $H$ . We apply a stress load  $Q_1(x)$  on top of the lamina and a stress load  $Q_2(x)$  on the bottom.  $Q_1(x)$  could represent any topographic structure, while  $Q_2(x)$  represents the upward buoyant force originating from the asthenosphere. We must do the following two assumptions:

1. Lamina is not subjected to strong deformations which are  $\ll$  thickness  $H$
2. Horizontal wavelengths both  $Q_1(x)$  and  $Q_2(x)$  are  $\gg$  thickness  $H$ , then the lamina is thin

Considering  $Q_1(x)$  and  $Q_2(x)$  and two previously written assumptions, our goal is to find the value of flexure  $w(x)$ , which is positive if considering a downward movement of surface respect to initial position. We establish that there are not physical quantities which depends on  $y$ , thus the components  $\epsilon_{xy}$ ,  $\epsilon_{yy}$ ,  $\epsilon_{zy}$  of the strain tensor  $\epsilon_{ij}$  are equal to 0. The same goes for the components  $\sigma_{xy}$  and  $\sigma_{zy}$  of the stress tensor  $\sigma_{ij}$ . We assume a situation where there is equilibrium and where we can ignore gravity forces, thus because the resultant surface force might be equal to 0 both

along x axis and z axis, then we have:

$$\partial\sigma_{xx}/\partial x + \partial\sigma_{zx}/\partial z = 0 ; \partial\sigma_{xz}/\partial x + \partial\sigma_{zz}/\partial z = 0 \quad (2.3)$$

The stress loads on external surfaces are:

$$\sigma_{zz}(z = H/2) = -Q_1(x) ; \sigma_{zz}(z = -H/2) = -Q_2(x) \quad (2.4)$$

The absence of shear stresses on external surfaces causes the following relation:

$$\sigma_{xz}(z = H/2) = 0 ; \sigma_{xz}(z = -H/2) = 0 \quad (2.5)$$

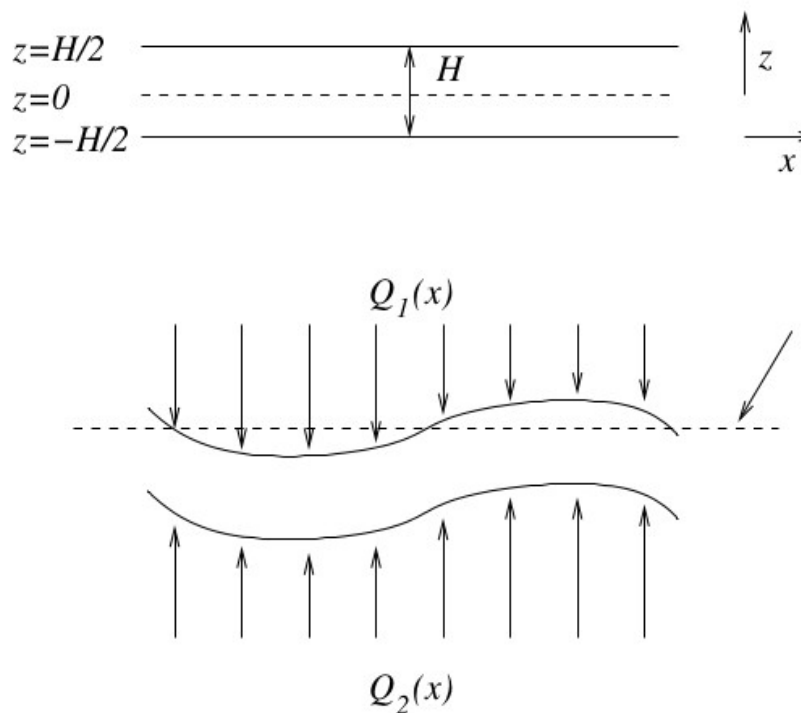


Figure 2.15: (a) Elastic lamina of thickness  $H$  in initial conditions with no stresses; (b) Elastic lamina after the application of stress load  $Q_1(x)$  and  $Q_2(x)$

Utilizing the constitutive equations between stress and strain (we omit them for simplicity) and the conditions (2.3), (2.4) and (2.5) we have a relation that connects the fourth derivative of flexure  $w(x)$  with the difference between the two stress loads  $Q_1(x)$  and  $Q_2(x)$  and the second derivative of flexure  $w(x)$

$$Q_1(x) - Q_2(x) - P(d^2w(x)/dx^2) = D(d^4w(x)/dx^4) \quad (2.6)$$

where  $P$  represents the horizontal pressure (if present) and  $D$  is the flexure rigidity. This parameter is given by:

$$D = [EH^3/12(1-\nu^2)] \quad (2.7)$$

where  $E$  is the Young's modulus and  $\nu$  is Poisson's modulus.

Considering now the case of an oceanic lithosphere in subducting. According to (2.6), if we exclude any horizontal loads, we have:

$$D(d^4w(x)/dx^4) + (\rho_m - \rho_a)gw = 0 \quad (2.8)$$

where  $\rho_a gw$  stands for  $Q_1(x)$ , with  $\rho_a$  which represents density of subducting oceanic lithosphere, while  $\rho_m gw$  stands for  $Q_2(x)$  where  $\rho_m$  stands for density of mantle in which oceanic lithosphere sinks. Quantity  $(\rho_m - \rho_a)gw$  represents the “slab pull”.

The solution of (2.8) is:

$$w = \exp(x/a)[c_1 \cos(x/a) + c_2 \sin(x/a)] + \exp(-x/a)[c_3 \cos(x/a) + c_4 \sin(x/a)] \quad (2.9)$$

where  $a$  is named “flexure parameter” and its expression is:

$$a = [4D/(\rho_m - \rho_a)g]^{1/4} \quad (2.10)$$

and the constants  $c_1, c_2, c_3, c_4$  are determined by initial conditions. Since  $w \rightarrow 0$  when  $x \rightarrow \infty$ , thus  $c_1 = c_2 = 0$ . If there are a load  $V_0$  on point of lamina at  $x = 0$  (see figure) and a flexing momentum  $-M_0$  in that point, we could demonstrate that there are:

$$c_4 = -(M_0 a^2)/2D \quad (2.11)$$

$$c_3 = (V_0 a + M_0)(a^2/2D) \quad (2.12)$$

and thus we have:

$$w = (a^2/2D)\exp(-x/a)[(V_0 a + M_0)\cos(x/a) - M_0\sin(x/a)] \quad (2.13)$$

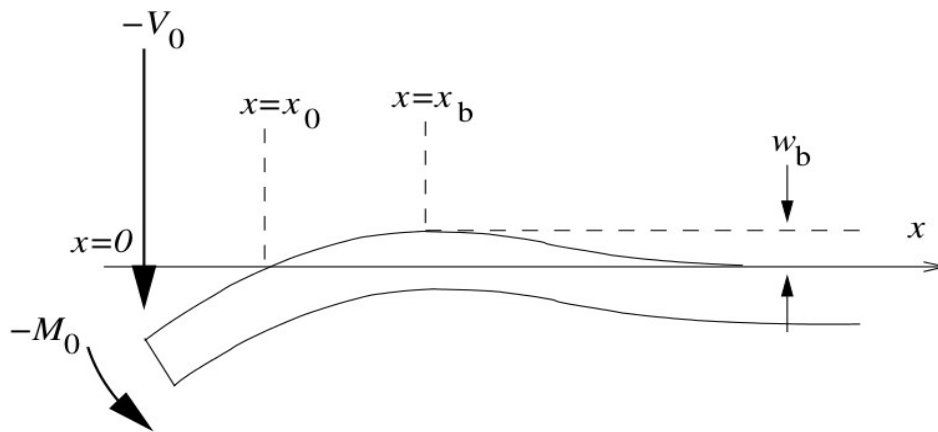


Figure 2.16: Elastic lamina where on it acts a load  $V_0$  and a flexing momentum  $M_0$

This solution is not a practical one. This occurs because we can not directly measure  $V_0$  and  $M_0$ . To solve this question, considering figure, the point  $x_b$  and its corresponding flexure  $w_b$ . We are able to measure the values of  $w_b$  and the difference  $x_b - x_0$ . It is simple to understand why I might execute the first derivative of (2.9) and put it equal to 0 to obtain value of  $x_b$  and, consecutively, value of  $w_b$ . Operating in this way, we could obtain that:

$$x_b - x_0 = (\pi/4)a \quad (2.14)$$

Previous equations could be made more compact in the following form:

$$w/w_b = \sqrt{2} \exp(\pi/4) \exp\{-\pi/4[(x - x_0)/(x_b - x_0)]\} \sin\{(\pi/4)[(x - x_0)/(x_b - x_0)]\} \quad (2.15)$$

This relation is in good agreement with observed data. For example, considering Mariana subduction zones. Observed data indicate  $x_b - x_0 = 55$  km and  $w_b = 500$  m. Thus,  $a = 70$  km. Considering  $\rho_m - \rho_a = 2300$  kg/m<sup>3</sup> and  $g \approx 10$  m/s<sup>2</sup>, we have  $D = 1,4 \times 10^{23}$  Nm. Fixing  $E = 70$  GPa and  $\nu = 0,25$ , according to (2.7) we have  $H = 28$  km. A result that is in perfect agreement with other observed data.

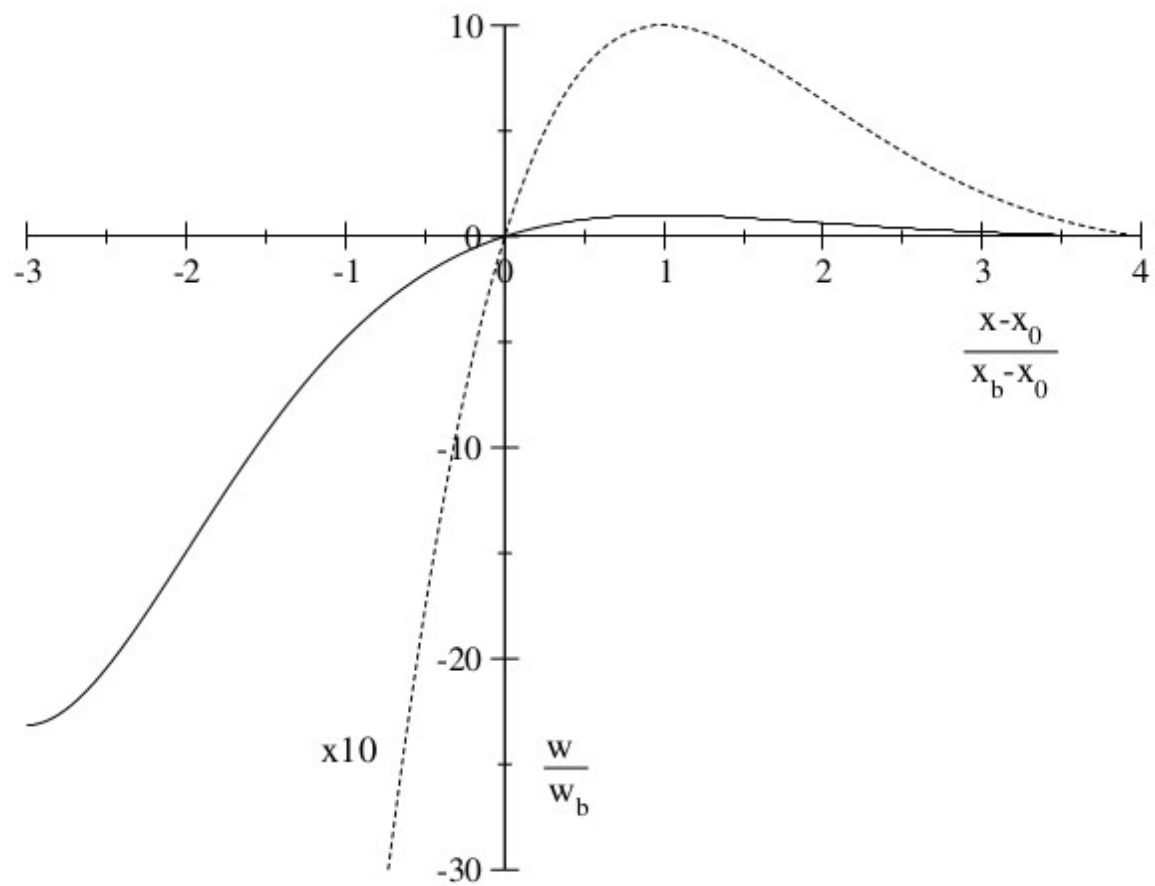


Figure 2.17: Graphical representation of relation (2.15)

# Chapter 3

## The Teleseisms

### 3.1 Classification of earthquakes depending on epicentral distance

An **earthquake** is a natural phenomenon which occurs when, at a certain depth in Earth's inner, one of two blocks that constitute a **fault** (this last one is a fracture in the crust) moves relative to one another parallel to fracture because of excessive accumulated stress and strain. Energy that is released during this movement arrives on Earth's surface by means of so-called **seismic waves**. The point on fault which is the source of these waves is called **hypocenter**. Its surface projection is named **epicenter**.

A seismic station is the designated device for registering the occurrence of an earthquake. It consists of a seismograph, that is an instrument used to detect and record earthquakes (generally, it consists of a mass attached to a fixed base), and of an instrument of data capture.

The **epicentral distance** is the effective spatial distance that is between the epicenter of an earthquake and the seismic station where has been recorded. And, depending on epicentral distance, we can proceed with a classification of earthquakes. We indicate with  $X$  the epicentral distance in kilometers and with  $\Delta$  the epicentral distance in degrees. We have classified the earthquakes in four categories.

- **Local earthquakes:** representing all earthquakes where  $X < 100$  km

- **Regional earthquakes:** constituting all earthquakes where  $X$  is included in range [100 km ; 1400 km] and therefore  $\Delta$  is included in range [ $1^\circ$  ;  $13^\circ$ ]
- **Upper mantle earthquakes:** composing all earthquakes where  $\Delta$  is included in range [13;30]
- **Teleseisms:** being regarded as all earthquakes where  $\Delta$  is  $> 30^\circ$

A seismogram is a record written by a seismograph in response to ground motions produced by an earthquake, explosion, or other ground-motion sources. Its correct interpretation of phases allows us to know which kind of earthquake is. For example, seismic recordings at local distances are strongly affected by shallow crustal structure, and relatively simple direct P and S phases (see paragraph 3.2) are followed by complex reverberations. Regional-distance seismograms are dominated by seismic energy refracted along or reflected several times from the crust-mantle boundary (see paragraph 3.2). The corresponding waveforms tend to be complex because many phases arrive close in time. Seismograms of upper mantle earthquakes are dominated by seismic energy that turns in depth range of 70 to 700 km below the surface. This region of the Earth has a very complex velocity distribution for the presence of a low velocity zone (see paragraph 2.1) and at least two major velocity discontinuities (400 and 670 km depths) within what is called the transition zone. The direct P and S phases at upper-mantle distances have complex interactions with the discontinuities. Instead, for the teleseisms, the direct P and S wave arrivals recorded at teleseismic distances out to  $\Delta \approx 95^\circ$  are relatively simple,

indicating a smooth velocity distribution below the transition zone, between 700 and 2886 km depth. The simplicity of teleseismic direct phases between  $30^\circ$  and  $95^\circ$  makes them invaluable for studying earthquake sources because few closely spaced arrivals occur that would obscure the source information (see paragraph 3.3). The overall seismogram at these distances is still complex because of the multiplicity of arrivals that traverse the mantle, mainly involving surface and core reflections. Beyond  $95^\circ$ , the direct phases become complicated once again due to interactions with the Earth's core (see paragraph 3.2).

<b>Nomenclature</b>	<b>Epicentral distance</b>	<b>Characteristics</b>
Local	$< 100$ km	Seismograms affected by crustal structure
Regional	$100 \text{ km} < X < 1000 \text{ km}$	Evidence of Moho reflections
Upper Mantle	$10^\circ < \Delta < 30^\circ$	Complex velocity distributions for the presence of three transition zones
Teleseisms	$\Delta > 30^\circ$	If $30^\circ < \Delta < 95^\circ$ , seismograms register P and S direct waves. Core “shadow zone” for P waves for $105^\circ < \Delta < 140^\circ$

**Table 3.1: Summary of Classification of earthquakes depending on epicentral distance**

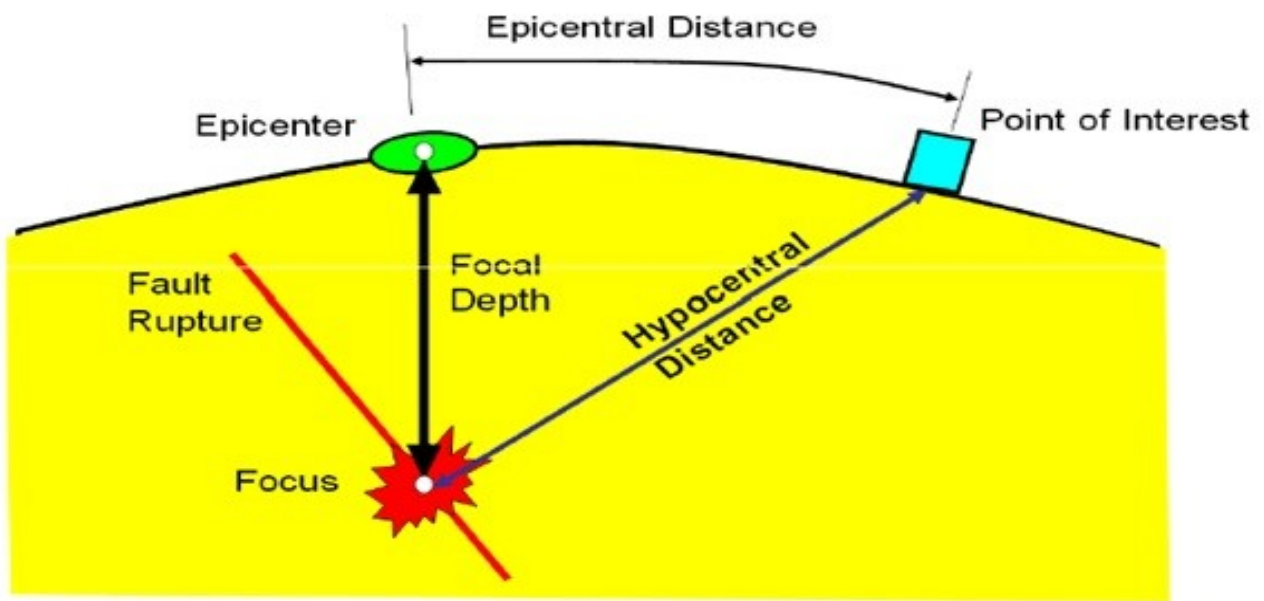


Figure 3.1: Graphical representation of Epicentral and Hypocentral Distance



Figure 3.2: Intuitive representation of difference between a Local Earthquake and a Telesism

## 3.2 Nomenclature of seismic body waves

A body wave is a seismic wave that moves through the interior of the earth, as opposed to surface waves that travel near the earth's surface. The simplest and most frequently studied body-wave phases are the direct arrivals. They travel the minimum-time path (following the Fermat's principle) between source and receiver and are usually just labeled P or S. The P-wave is a longitudinal one and it is the first that seismographs record. Its equation is:

$$(\mathbf{1}/v_P^2)(\partial^2 \mathbf{s}_P / \partial t^2) = \nabla^2 \mathbf{s}_P \quad (3.1)$$

where  $v_P$  is the velocity of P-wave,  $s_P$  is a curl-free scalar potential field and  $t$  is the time. Expression of  $v_P$  is explicited in the following formula:

$$v_P = [(\lambda + 2\mu) / \rho]^{1/2} \quad (3.2)$$

where  $\lambda$  and  $\mu$  are so-called “Lame's parameters” and  $\rho$  is the density.

The S-wave is a trasversal one and it is the second that seismographs record. Its equation (where  $s_S$  is a divergenceless vector potential field and  $t$  is the time) is:

$$(\mathbf{1}/v_S^2)(\partial^2 \mathbf{s}_S / \partial t^2) = \nabla^2 \mathbf{s}_S \quad (3.3)$$

where  $v_S$  is:

$$v_s = [\mu/\rho]^{1/2} \quad (3.4)$$

At epicentral distances greater than a few tens of kilometers in the Earth direct arrivals usually leave the source downward, or away from the surface, and the increasing velocities at depth eventually refract the wave back to surface. The angle that the *seismic ray* (that is the geometrical construction that approaches seismic wave, right until epicentral distance is greater than wavelength) makes with a downward vertical axis through the source is known as the takeoff angle. If the takeoff angle of a ray is less than  $90^\circ$ , the phase, or that segment of the raypath is labeled with a capital letter: P or S. If the seismic ray has a takeoff angle greater than  $90^\circ$ , the ray is upgoing, and if it reflects from the surface or is a short upgoing segment of a composite raypath, it is signified by a lowercase letter: p or s. Upgoing rays that travel from the source up to the free surface, reflect, and travel on to the receiver are known as *depth phases*. The various portions of the path a ray takes, for example, between the source and the free surface, are known as legs. Each leg of a ray is designated with a letter indicating the mode of propagation as a P or S-wave, and the phase is designated by stringing together the names of legs. Thus, there are four possible depth phases that have a single leg from the surface reflection point to the receiver: pP, sS, pS and sP. The relative timing between the direct arrivals and the depth phases is very sensitive to the depth of the seismic sources. At local and regional distances a special nomenclature is used to describe the travel paths. The direct arrivals at these short distances are usually referred to as  $P_g$  and  $S_g$ . Depending on the source depth, the velocity

gradient within the shallow crust, and the distance between the source and the station, these arrivals may be either upgoing or downgoing phases. The  $g$  subscript is from early petrological models that divided the crust into two layers: an upper granitic layer over a basaltic layer. The majority of nomenclature of seismic body waves depends on *surfaces of discontinuity*. Indeed, body waves could be reflected and/or refracted by these surfaces. Otherwise, there are body waves that travel along a surface of discontinuity because incident angle on it is a critical angle that does not allow an incident ray on it to have a refraction. These particular body waves are named *head waves*. For example, considering **Mohorovičić** discontinuity (best known as **Moho**), that is the discontinuity between the crust and the mantle. Its name is due to its discoverer, the Croatian geophysicist Andrea **Mohorovičić**, who introduced the concept of this discontinuity in 1909. Waves that travel as head waves along, or just below, the Moho are known as  $P_n$  and  $S_n$ . Moho reflections are labeled  $P_mP$ ,  $P_mS$ ,  $S_mP$  or  $S_mS$  (note that each leg of the ray is named and “m” denotes a reflection at the Moho). At distances less than about 100 km,  $P_g$  is the first arrival. Beyond 100 km (depending on the crustal thickness),  $P_n$  becomes the first arrival.

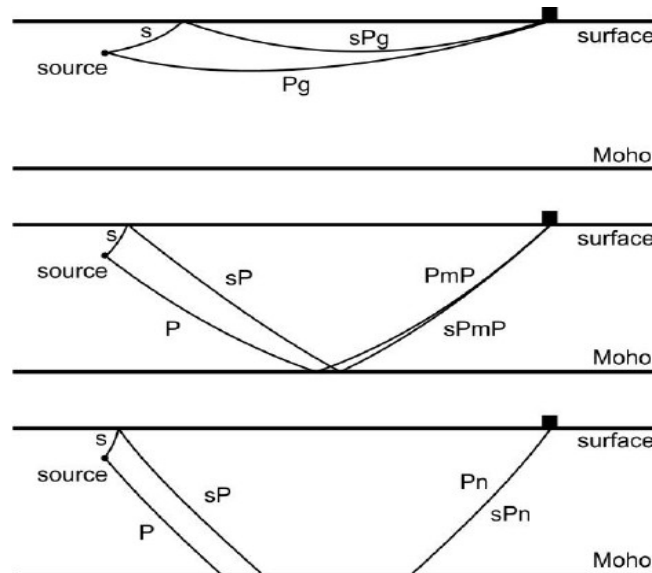


Figure 3.3: Sketch figures for regional depth phases  $sPg$  (upper panel),  $sPmP$  (middle panel), and  $sPn$  (bottom panel)

In many regions of the Earth additional regional arrivals are observed that have classically been interpreted as head waves traveling along a midcrustal velocity discontinuity, usually known as the **Conrad discontinuity**, named after the austrian seismologist Victor **Conrad**. This discontinuity is present in some parts of continental crust at 15-20 km of depth and it divides a more rigid part of crust from a less one. The arrivals associated with the Conrad are labeled  $P^*$  and  $S^*$  or  $P_b$  and  $S_b$ , respectively. At distances beyond  $13^\circ$ ,  $P_n$  amplitudes typically become too small to identify the phase, and the first arrival is a ray that has bottomed in the upper mantle. The standard nomenclature for this arrival is now just  $P$  or  $S$ , although subscripts are used to identify different triplication branches for the transition zone arrivals. Seismic phases that reflect at a boundary within the Earth are subscripted with a symbol representing the boundary. For example,  $P_cP$  indicates a  $P$ -wave subject to reflection at the

core. In a spherical Earth it is possible for a ray to travel down through the mantle, return to the surface, reflect and then repeat the process. Because the original ray initially traveled downward, the phase is denoted by a capital letter. The free-surface reflection is not denoted by a symbol; rather, the next leg is just written P or S. This type of phase is known as a surface reflection. Some common surface reflections are PP, PS and PPP where PP and PS each have one surface reflection (involving conversion for PS), and PPP has two surface reflections. Multiple reflections from both the core and surface occur as well, such as  $P_cPP_cP$ ,  $S_cSS_cS$  and  $S_cSS_cSS_cS$ . Both reflected phases and surface reflections can be generated by depth phases. In this case the phase notation is preceded by a lowercase s or p, for example,  $pP_cP$  and  $sPP$ . All of these phases are a natural consequence of the Earth's free surface and its internal layering, combined with the behavior of elastic waves. The amplitude of body-wave phases varies significantly with epicentral distance. This occurs both because reflection coefficients depend on the angle of incidence on a boundary and because the velocity distribution within the Earth causes focusing or defocusing of energy, depending on behavior of geometric spreading along different raypaths. Thus, the fact that a raypath can exist geometrically does not necessarily mean it will produce a measurable arrival. For example, the P-wave reflection coefficient for a vertically incident wave on the core is nearly zero (the impedance contrast is small), but at wider angles of incidence the reflection coefficient becomes larger. Thus,  $P_cP$  can have a large amplitude in the distance range  $30^\circ < \Delta < 40^\circ$ . The surface reflections PS and SP do not appear at distances of less than  $40^\circ$ , but they

may be the largest-amplitude body waves beyond  $100^\circ$ . Progressive energy losses due to attenuation cause multiple reverberations to become smaller. Amplitudes are further complicated by variability of excitation, which depends on the orientation of the seismic source.

Direct P-waves that travel beyond  $95^\circ$  show rapidly fluctuating, regionally variable amplitudes. Beyond  $100^\circ$  the amplitudes decay rapidly, and short-period energy nearly disappears beyond  $103^\circ$ . Short-period P-waves reappear beyond  $140^\circ$  but with a discontinuous travel-time branch. The distance range  $103^\circ < \Delta < 140^\circ$  is called the **core shadow zone** and is caused by a dramatic drop in seismic velocities that occurs going from the base of the mantle into the core. Body waves that pass through the core have their own nomenclature. The legs of P-waves traversing the outer core are denoted by a K (from *Kernwellen*, the German word for core). The outer core is a fluid, so only P waves can propagate through it. Thus a P-wave that travels to the core, traverses it and reemerges as a P-wave is denoted as PKP. Similarly, it is possible to have phases PKS. The leg of a P wave that traverses the inner core (which is solid) is denoted with an I (for example, PKIKP); a S wave that traverses the inner core is written as J (for example, PKJKP). A reflection from the inner core-outer core boundary is denoted with an i (for example, PKiKP). Since the core-mantle boundary is such a strong reflector, it produces both topside (for example, PcP) and bottomsides (for example, PKKP) reflections. P waves reflected once off the underside of the boundary are denoted PKKP, and other phases include SKKS, SKKP and PKKS. Paths with multiple underside reflections are identified as  $P_mKP$ ,  $S_mKS$ , ecc..., where m gives the number of K legs and

$m-1$  gives the number of underside reflections. Seismic arrays have provided observations of P7KP. The outer core has little P-wave attenuation, so short-period P signals can be observed even for phases with long path lengths in the core. Multiple PKP branches can be observed at a given distance due to the spherical structure of the core and velocity gradients within it. P, PcP and PkiKP phases decrease in amplitude. This results mainly from geometric spreading in the Earth and from weak reflection coefficients at different boundaries for the latter phases. An important consideration is that the multiplicity of seismic arrivals should be not confused with complexity of the source process or with the existence of more than one initial P and one initial S spherical wavefront released from the source. First of all, seismic rays are an artifice for tracing a three-dimensional wavefront and that wave interactions with any boundary or turning point in the Earth have frequency-dependent effects. Interactions with the Earth strongly distort the initial outgoing P wavefront, folding it back over on itself and begetting secondary wavefronts as energy partitions at boundaries. The body wave nomenclature simply keeps track of the geometric complexity involved. The energy that arrives at one station as P may arrive at another station as PP with additional propagation effects. It is thus constructive to think of this as a wavefield that has been selectively sampled at different locations as a function of time rather than as discrete energy packets traveling from source to receiver. If we knew the Earth's structure exactly, we could reverse the propagation of the entire wavefield back to the source, successfully reconstructing the initial outgoing wavefront. Of course,

sources can also have significant temporal and spatial finiteness, often visualized as subevents, each giving rise to its own full set of wave arrivals that superpose to produce very complex total ground motions. Because of our imperfect knowledge of planetary structure, there are limits to how well we can separate source and propagation effects.

<b>Nomenclature of a phase</b>	<b>Meaning</b>
P, S	Direct P-wave, direct S-wave
pP, sP, sS, sP	Depth phases
$P_g, S_g$	P and S at local and regional distances
$P_n, S_n$	P and S along the Moho as head waves
$P_mP, P_mS, S_mP, S_mS$	P and S reflected at Moho and that remain P (analogous S) or change to S (analogous P)
$P_b$ (or $P^*$ ), $S_b$ (or $S^*$ )	P and S reflected at Conrad discontinuity
$P_cP, S_cS, P_cS, S_cP$	P and S reflected at core and that remain P (analogous S) or change to S (analogous P)
PP, PS, SS, SP	P and S reflected at Earth's free surface and that remain P (analogous S) or change to S (analogous P)
$P_cPP_cP, S_cSS_cS$ and $S_cSS_cSS_cS$	P and S which are reflected both at core and Earth's free surface more times
pP <sub>c</sub> P, s <sub>c</sub> P and other similar	Depth phases P and S which are reflected both at core and Earth's free surface more times
PKP, PKS	P-wave which travel in outer core

	and or remain P or change to S
PKIKP	P-wave which travel in inner core
PKiKP	P-wave which are reflected at boundary inner core – outer core
$P_m$ KP, $S_m$ KS and other similar	P-wave (analogous S-wave) with m “K legs” due to m-1 underside reflections
PKJKP	P-wave that in inner core becomes a S-wave

Table 3.2: Summary of body-wave nomenclature

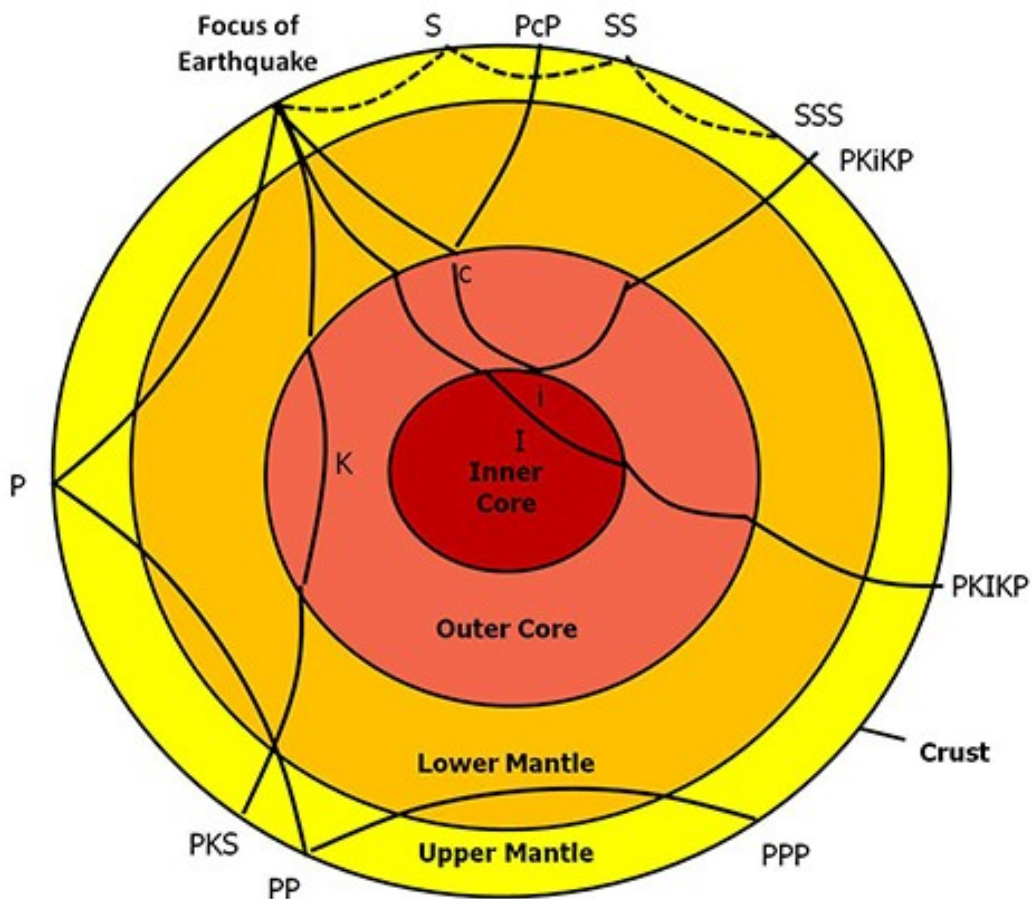


Figure 3.4: Graphical representation for various surface reflections observed in the Earth and raypaths for various core phases

### 3.3 Interpretation of a teleseismic seismogram

A seismogram is influenced by three factors: propagation effects, source effects and characteristics of the seismometer itself. It is possible to model each of these effects mathematically and, therefore, to develop a procedure to predict the character of a seismogram in a realistic model of the Earth. Such a mathematical construction is known as a synthetic seismogram. The formalism of comparing synthetic and observed seismogram is known as waveform modeling. Mathematically, the construction of synthetic seismogram happens following the linear filter theory. That is, the seismogram is treated as the output of a sequence of linear filters. Therefore, we can write the following relation:

$$u(t) = s(t)*g(t)*i(t) \quad (3.5)$$

where  $u(t)$  is the seismogram,  $s(t)$  is the signal from the seismic source,  $g(t)$  is the propagation filter and  $i(t)$  is the seismometer response. Symbol “\*” stands for *convolution*.

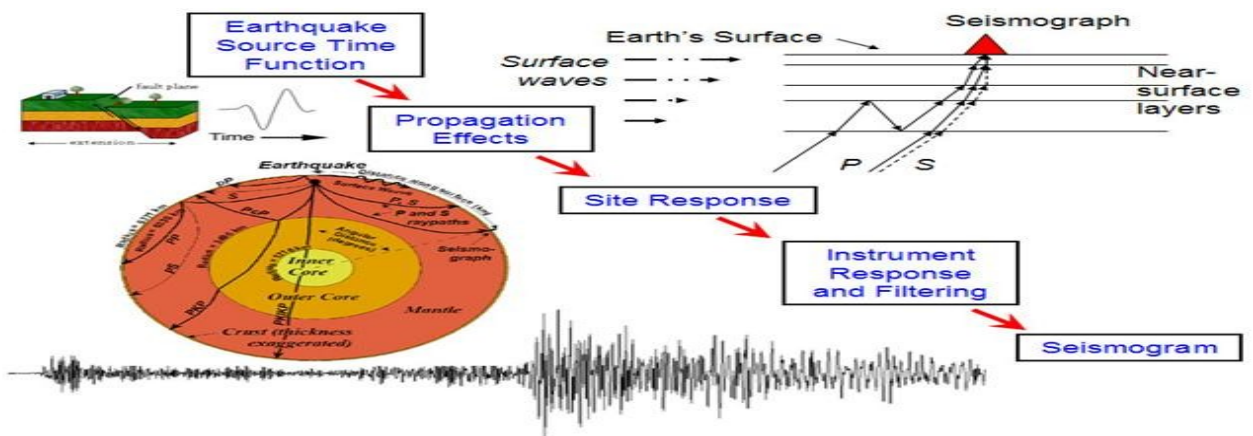


Figure 3.5: Graphical representation of the construction of a seismogram

In (3.5) the most complex filter is  $g(t)$ . It is often named Earth transfer function. This filter accounts for all propagation effects such as reflections, triplications, diffractions, scattering, attenuation, mode conversions, as well as geomeric spreading.

The usual procedure is to divide  $g(t)$  into a filter that accounts for **elastic phenomena**,  $R(t)$ , and a filter that accounts for **attenuation**,  $A(t)$ . At teleseismic distances,  $R(t)$  is a time series with a sequence of impulse temporally distributed to account for the variability in arrival times. More specifically, since P, pP and sP are the most important P-wave arrivals at teleseismic distance,  $R(t)$  is a “spike train” with three pulses spaced to account for the difference in arrival times. The amplitude of a given spike depends on the angle of incidence at the surface and the seismic-radiation pattern. For a point source (therefore, in a so-called far field approximation, see appendix 2),  $R(t)$  has the form:

$$\mathbf{R}(t) = (1/4\pi\rho r\alpha^3)\sum_{k=1,N}\sum_{i=1,3}\mathbf{A}_i\mathbf{c}_i\mathbf{R}_{Mok}\mathbf{\Pi}_k \quad (3.6)$$

where  $\rho$  is the density,  $r$  the distance source-receiver,  $\alpha$  stands for velocity of P-wave (3.2),  $A_i$  and  $c_i$  are respectively the coefficients of horizontal radiation pattern and the coefficients of vertical radiation pattern,  $R_{Mok}$  is the receiver function (that is a parameter which describe crustal layering beneath isolated three-component stations) and  $\Pi_k$  is the product of all the transmission and reflection coefficients that the  $k$ -th ray experiences on its journey from the source to receiver.

As written previously, the relative amplitudes of the spikes in  $R(t)$  vary greatly depending on source orientation. This variability produces

waveforms that are diagnostic for different fault orientations. Waveform modeling is much more powerful for constraining fault orientation than first-motion focal mechanisms because it provides more complete coverage of the focal sphere and uses relative-amplitude information. A realistic  $R(t)$  actually contains many more than just three wave arrivals. For a layered Earth structure, multiple reflections and conversions occur both near the source and beneath the receiver. In general, these multiples are much less important than the primary three rays at teleseismic distances unless the earthquake occurred beneath the ocean floor. In this case, water reverberations, rays bouncing between the surface and ocean floor, can produce significant additional spikes.

The attenuation filter,  $A(t)$ , is usually represented by a  $t^*$  operator (where  $t^*$  indicates the ratio between the traveltime  $t$  and the Quality factor  $Q$ , see Appendix 2). At teleseismic distances,  $t^*$  is nearly constant over much of the body-wave frequency band and is thus easy to parameterize as a filter. As  $t^*$  increases, the high frequencies are more effectively removed (remember that the amplitude of the short-period signal is affected by changes in  $t^*$  to a much greater degree than the long-period signal).

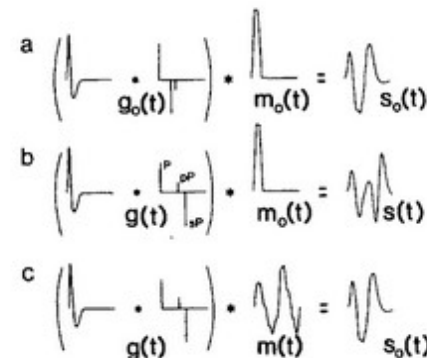


Figure 3.6: Illustration of the trade-off between source depth and source time function duration for teleseismic P waves (“Analysis of trade-off between hypocentral depth and source time function”, Christensen & Ruff, 1995)

Now, we consider a full moment tensor source (see Appendix 2) where all moment tensor terms have an identical source time history  $s(t)$ . Operating in this way, equation (3.5) can be written as:

$$\mathbf{u}_n(\mathbf{x},t) = s(t)*\mathbf{i}(t)*\sum_{i=1,5}(\mathbf{m}_i \cdot \mathbf{G}_{in}(t)) \quad (3.7)$$

where  $u_n$  is the vertical, radial, or tangential displacement and the Earth transfer function has been replaced by the summation operator. The summation is the product of the seismic moment tensor, and precisely we have  $m_1 = M_{11}$ ,  $m_2 = M_{22}$ ,  $m_3 = M_{12}$ ,  $m_4 = M_{13}$ ,  $m_5 = M_{23}$ , and  $G_{in}(t)$  are the corresponding Green's functions (see Appendix 2). These last one are impulse displacement responses for a seismic source with orientation given by each corresponding moment tensor element. We can observe as the  $i$ -th moment tensor Green's function will give three components ( $n$ ) of displacement. Any arbitrary fault orientation can be represented by a specific linear combination of moment tensor elements, thus the summation in (3.7) implies that any Earth transfer function can also be constructed as a linear combination of Green's functions. This is an extremely powerful representation of the seismic waveform because it requires the calculation of only five (or with some recombination of terms, four) fundamental Green's functions to produce a synthetic waveform for an arbitrary moment tensor at a given distance. The computation of Green's function is not a problem at teleseismic distance. In fact, the rays P, pP and sP have simple structural interactions and turn in the lower mantle where the seismic velocity structure is smooth. Although “ringing”

can occur in a sedimentary basin, for the most part teleseismic Green's functions for isolated body-wave arrivals are simple.

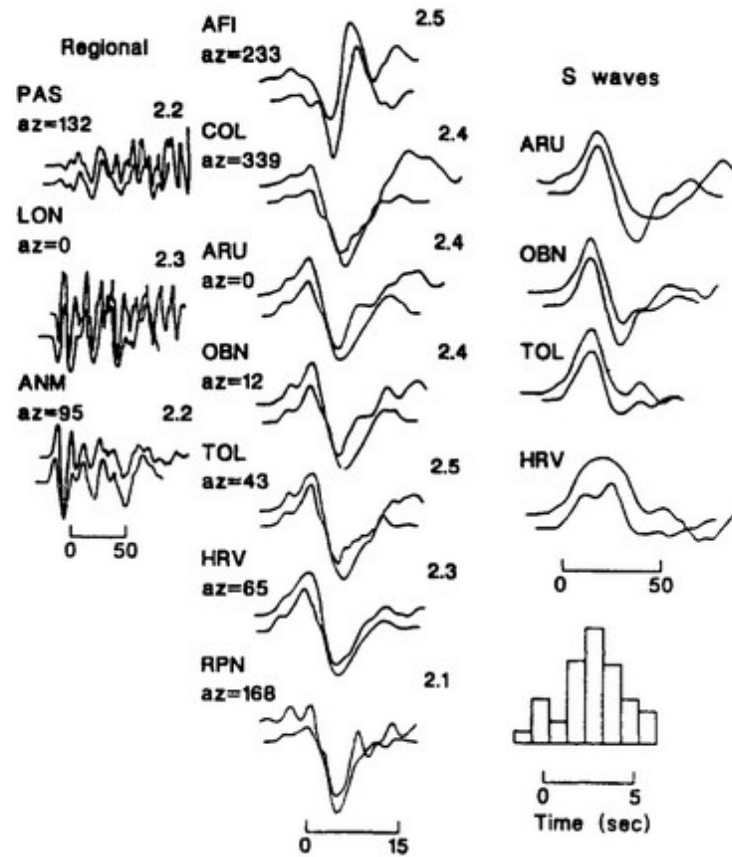


Figure 3.7: An example of waveform modeling for the 1989 Loma Prieta earthquake. Ground displacements are for the  $P_n$  and teleseismic P and SH waves (“A broadband seismological investigation of the 1989 Loma Prieta, California earthquake; evidence for deep slow slip?”, Wallace et al., 1991)

## Chapter 4

### Teleseismic tomography of Southern Tyrrhenian: procedure description, methods and results

#### 4.1 The Southern Tyrrhenian: tectonic settings

The Tyrrhenian Sea is a back-arc basin (that is, it is a basin made up of oceanic crust associated to a roll-back subduction, see Chapter 2.2) that is a result of the subducting Ionian slab since Tortonian Age (10 Ma).

For understanding in a better way the tectonic settings of Southern Tyrrhenian, we start from 65 Ma, when the complex and slow convergence (0.5-0.8 cm/yr) between Eurasian and Africa plates, began to be active.

This process provoked the Alpine orogenesis first in Eocene-Oligocene period (around to 38 Ma) and after the origin of the eastward migration of the subduction hinge that drove the geodynamic evolution of the Tyrrhenian-Apennine system (Malinverno & Ryan, 1986). During that period (around to 26 Ma), the block Corsica-Sardinia-Calabria broke off the Europe because of a distensive stress field and this result caused the opening of the Ligurian Sea and of the Gulf of Lion and a roll-back toward southeast of an older northwest dipping subduction zone (Faccenna et al., 1996; Rosenbaum and Lister, 2004). A direct consequence of this opening was a counter-clockwise rotation of the block Corsica-Sardinia-Calabria together with the former western margin of Apulia and the formation of the Apenninic chain (Patacca & Scandone, 1989; Patacca et al., 1992).

Another important consequence was the starting of a roll-back subduction

of the Ionian slab, which we can consider as an oceanic portion of African plate. It started to sink under Apenninic chain and this fact caused the opening of the Southern Tyrrhenian basin. This opening began almost 10 Ma during Tortonian Age and its advancement reached a rate of 6 cm/yr (Faccenna et al., 2001). At that time the lithospheric rifting separated the Calabria block from the Sardinia basement. This process of separation caused the formation of new oceanic crust generating westward the Vasilov Basin (4.3-2.6 Ma according to Sartori, 1989 ; 8.5-4.5 Ma according to Argnani, 2000) and then southeastward the Marsili Basin (1.6 Ma according to Kastens et al., 1988; 2.0-1.7 Ma according to Argnani, 2000). The last chapter of this evolutive history starts 700000 years ago, at the origin of so-called Pleistocene age. It was a crucial moment for evolution of Mediterranean Sea. In fact, during this period both Vasilov Basin and Marsili Basin, which were the principal nodes of expansion of Southern Tyrrhenian, finished their activity. They had been replaced by a new center of opening, the Marsili volcano and direction of Calabria's migration changed from NW-SE to a similar WE. This factor caused the formation of currently active Aeolian Island Arc (Marani & Trua, 2002). At this point, there was the formation of two great lithospheric lines which had a transcurrent flow: the Pollino line and the Taormina line. The first one is the cause of division between Southern Tyrrhenian and Apenninic chain and along it there was the surge of a big submarine and effusive volcano, the Palinuro. Along the second line there was the formation of Etna volcano. At the present day, the most of the oceanic lithosphere in the Tyrrhenian-Apennine system has been consumed with exception of the

Calabrian arc sector where there is still subducting Ionian lithosphere, confined to the southwest by the Malta Escarpment (Calò et al, 2009).

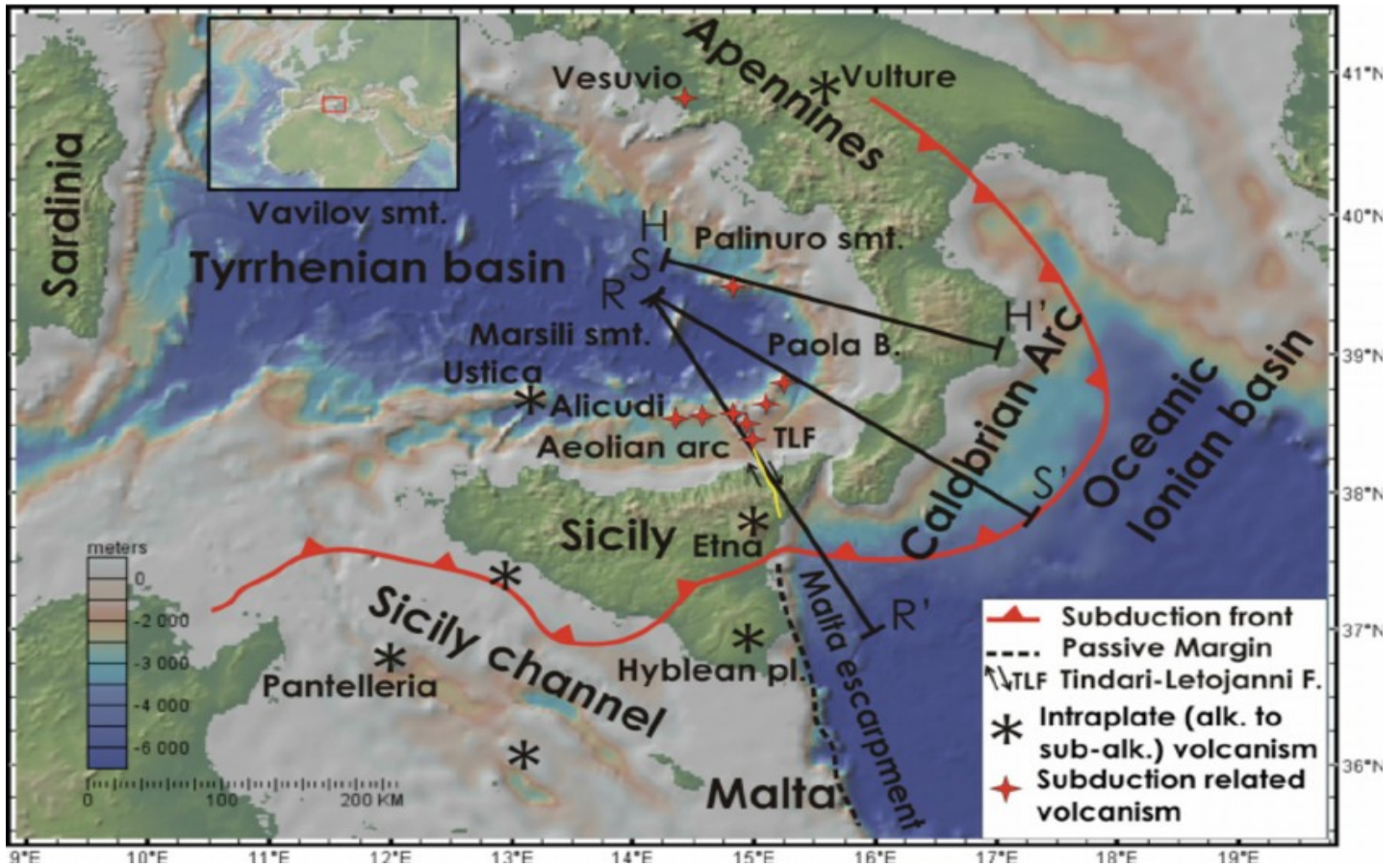


Figure 4.1: Schematic geological map of Southern Italy (“Seismic velocity structures of Southern Italy from tomographic imaging of Ionian slab and petrological interferences”, Calò et al., 2012)

## 4.2 A qualitative description of procedure and methods for a teleseismic tomography of Southern Tyrrhenian

The aim of this work is to perform a teleseismic tomography of Southern Tyrrhenian to investigate its inner structure until 500 km of depth. The majority of seismic tomographies carried out in this area have been done using local earthquakes. Thus, the 3D models obtained only describe in a good way the crust and the first part of upper mantle (maximum reached depth of Southern Tyrrhenian local tomographies is 350 km).

To perform the teleseismic tomography subject of this research, first of all we have selected a set of teleseismic events and their P-wave travel times to invert them. These data have been taken from International Seismological Centre (ISC) arrival times catalogue available online at website:

<http://www.isc.ac.uk/iscbulletin/search/arrivals/>.

We have gathered 2979 teleseisms recorded by 285 Italian ISC seismic stations since 1980 to 2012 with a total of 99503 arrival times relating to P phases. The gathered teleseisms satisfy the following parameters:

- magnitude > 6
- epicentral distance included in the range [20° ; 100°]
- station residual included in the range [-2 seconds ; 2 seconds]
- each teleseism must be recorded by almost 10 stations

The code used to invert the arrival times has been *FMTT (Fast Marching*

*Teleseismic Tomography*). This, code developed by Nick Rawlinson, will be described in paragraph 4.3. The huge quantity of data at our disposal made the process of inversion very difficult because of high computational cost for our computers. Thus, we have made a decision of cutting the first 10 years (1980-1990) of data and of considering only ISC southern Italy seismic stations. In this way, we have inverted 18515 P phases. A clear cut respect to initial database which has compromised inevitably the resolution of our work.

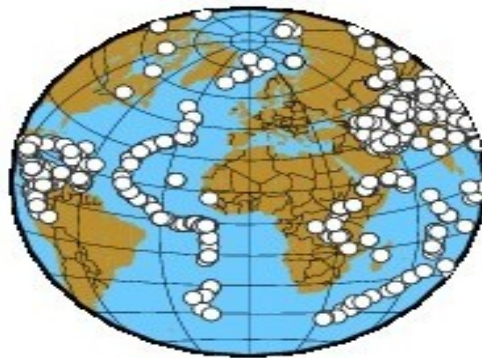


**Figure 4.2: GMT image of gathered teleseisms (white dots) used for this work**

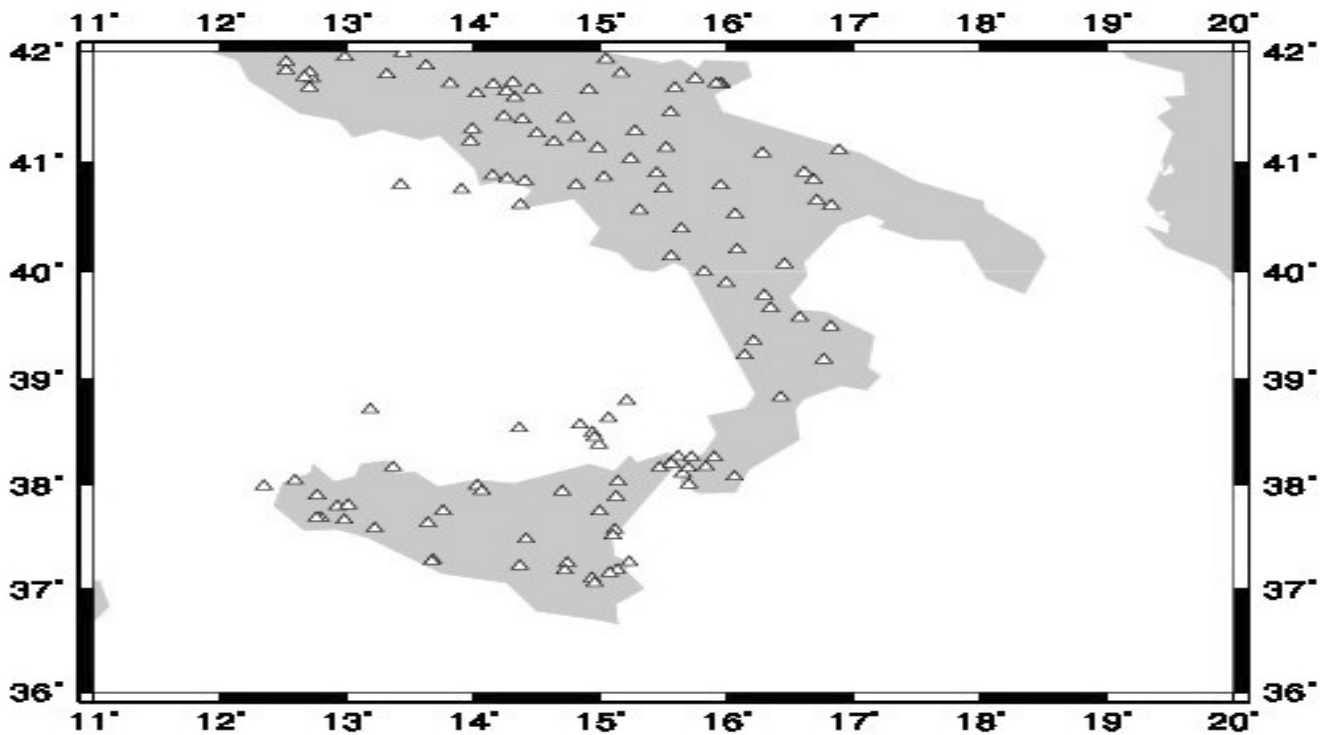


Figure 4.3: GMT image of ISC Southern Italy seismic stations (white triangles) used for this work

Tomographic images (horizontal, vertical and transversal sections) have been graphed using **GMT** (*Global Mapping Tools*, Wessel & Smith, 1987) and **Golden Surfer** (Smith & Madison, 1983).

During the whole procedure, we have written some codes in Matlab language for the preparation of input files and for adapting output files to a legible form for Golden Surfer software.

### 4.3 The FMTT code

As previously written, the code used for this work about teleseismic tomography of Southern Tyrrhenian is the **FMTT**, acronym of ***Fast Marching Teleseismic Tomography***. This code was developed by Nick Rawlinson and Nicholas Sambridge in 2006 and perfected in 2008. It consists in a series of softwares written in Fortran 90 language. Its method of working could be summarized in the following two points:

- Solving of Forward Problem (see Chapter 1) computing theoretical traveltimes solving (1.23) by means of Fast Marching algorithm (Sethian & Popovici, 1999, see Appendix 3) and using ak135 1-D velocity model (see appendix) as starting model.
- Solving of Inverse Problem (see Chapter 1) inverting theoretical traveltimes by means of Singular Value Decomposition using Subspace inversion (Kennett, Sambridge & Williamson, 1998, see Appendix 4).

First of all, code computes teleseismic traveltimes to the base of a local 3-D model beneath a receiver array using ak135 predictions. At this point, Fast Marching algorithm starts from the base of the model computing theoretical traveltimes to receivers located within it. Model has the framework of a grid where the position of a single node is in spherical coordinates (this because it should be considered the effect of Earth curvature in case of teleseisms). Fast Marching algorithm interpolates

nodes with a tri-cubic B-spline technique (see Appendix 2) which produces a continuous, smooth and locally controlled velocity medium. Next step is the inversion by means of SVD and subspace method (see Appendix 4). Two parameters are very important in this step: *smoothing* and *damping*. The first one controls the smoothness of the solution model, while the second ensures that the solution model is not too far from the initial model. An appropriate choice of the values to assign to these parameters – according to quality of data at his own disposal – allows to obtain inversions with a good resolution. Tables 4.1 and 4.2 describe the framework of FMTT's input and output files.

<b>Input files</b>	<b>Content</b>
<b>Sources.dat</b>	Number of events, localization (latitude, longitude and depth) of each event and its phase
<b>Receivers.dat</b>	Localization (latitude, longitude and height) of receivers
<b>Gridi.vtx</b>	The initial model. Its first three records specify the numbers of grid nodes for latitude, longitude and depth, the coordinate of grid origin and grid spacing in latitude, longitude and depth
<b>Otimes.dat</b>	Observed arrival time residuals (in seconds)
<b>Rtimes.dat</b>	Theoretical traveltimes (in seconds)

**Table 4.1: Description of input files of FMTT code**

<b>Output files</b>	<b>Content</b>
<b>Gridc.vtx</b>	The solution model with the same framework of gridi.vtx
<b>Rtravel.out</b>	Observed traveltimes (in seconds)
<b>Frechet.out</b>	Frechet matrix used during process of solving of inverse problem
<b>Raypath.out</b>	Paths of seismic rays of considered events
<b>Residuals.dat</b>	Two columns of data. First contains RMS value (in ms, for each iteration) computed on traveltimes residuals. Second contains variance on traveltimes residuals (in s <sup>2</sup> , for each iteration)

**Table 4.2: Description of output files of FMTT code**

This table describe the softwares which constitute the FMTT package and their work:

<b>Software</b>	<b>Work</b>
<b>Aktsurf</b>	It computes theoretical traveltimes
<b>Itimes</b>	It computes observed traveltimes
<b>Fm3dt</b>	It solves forward problem by means of Fast Marching algorithm and produces Fréchet matrix
<b>Grid3dtg</b>	It produces a 3D grid for the Fm3dt
<b>Subinv</b>	It solves inverse problem by means of subspace method
<b>Residualst</b>	It computes RMS and variance of traveltimes residuals
<b>Gmtslicet</b>	It changes the content of output files in a legible form for GMT

**Table 4.3: Description of software which constitute the FMTT code**

#### 4.4 Description of method of adjustment of data to FMTT code

In a way to obtain the best possible resolution for our work, according to database at our disposal, we have made an opportune choice of grid spacing and of smoothing and damping parameters (see paragraph 4.3). We will describe the procedure of this choice in this paragraph. But, first of all, we must do a right and proper mention to our preparation of input file `otimes.dat` (see paragraph 4.2). As previously written, this file contains observed arrival times residuals. It is organised in three columns. First one has the value “1” if the residual is valued into inversion, otherwise has the value “0”. Second one has the observed arrival times residuals in seconds. Third one has the error associated with the single pick (also in seconds). The total number of records is the product between the number of sources and the number of receivers.

According to data at our disposal, there are two problems to solve. First, we consider our 122 ISC southern italian seismic stations as an array of stations which have recorded seismic events in the same period of time. Obviously, this is a strong approximation because our stations have not recorded seismic events in the same period of time. That is, each earthquake has been recorded by a subset of all seismic stations and these subsets are different from each other. We have solved this problem sorting the stations and the teleseisms and putting “1” when that station had effectively recorded that teleseism, “0” otherwise. Second problem is the error associated with the single pick. We have not at our disposal these errors because they are not present on ISC catalogue where we have

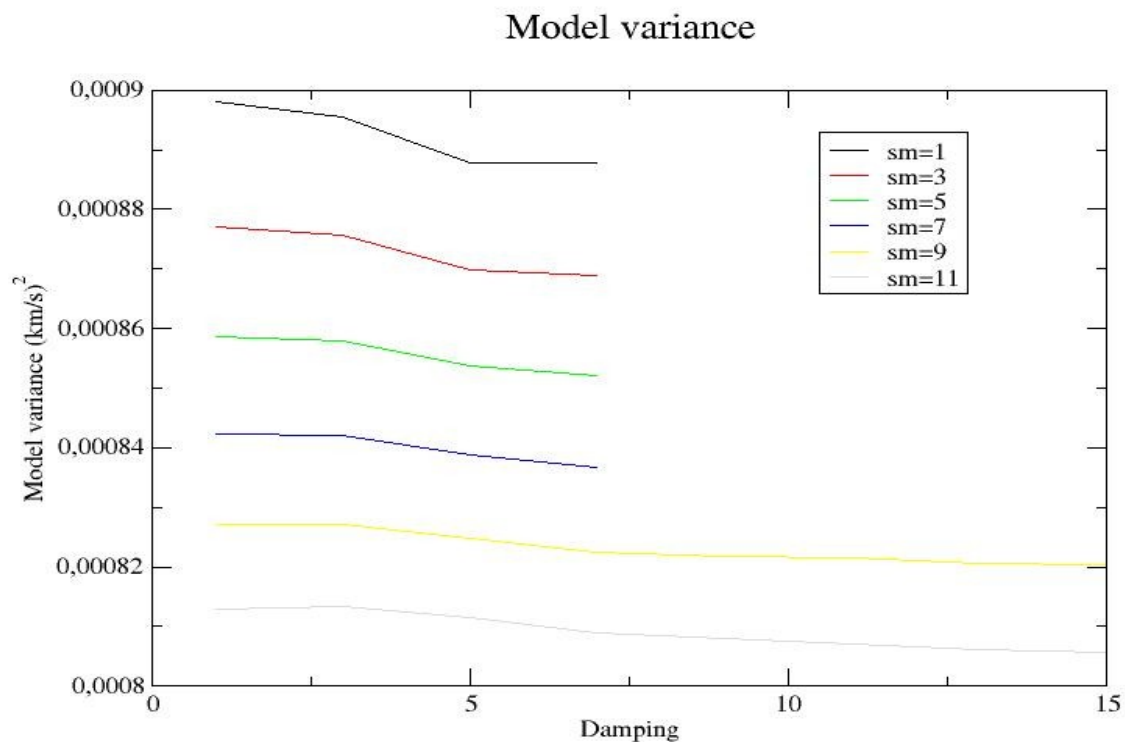
gathered our arrival times. Thus, we have made the following approximation. We have considered the errors that are present in examples supplied by Rawlinson in the FMTT package and we have computed their mean. Thus, we have fixed the error associated at value 0.045 seconds. The second question is the appropriate choice of grid spacing. As we can observe from figure 4.3 and as previously written, we have not a good distribution of seismic stations in Southern Tyrrhenian. In this way, it would be appropriate the choice of a grid spacing not too narrow to obtain a better uniformity to the network of seismic stations at our disposal. Thus, we have made a choice of grid spacing which is described in the following table:

<b>Limits of grid in depth (km)</b>	0-500
<b>Limits of grid in longitude (degrees)</b>	7°E - 20°E
<b>Limits of grid in latitude (degrees)</b>	35°N-48°N
<b>Grid spacing in depth (km)</b>	50
<b>Grid spacing in longitude (degrees)</b>	0.8
<b>Grid spacing in latitude (degrees)</b>	0.48
<b>Grid nodes in depth</b>	10
<b>Grid nodes in longitude</b>	17
<b>Grid nodes in latitude</b>	28

**Table 4.4: Description of characteristics of grid used for the inversion**

Next step is the choice of the values for the parameters of smoothing and damping. To obtain it, we have tested the model roughness and the model variance fixing smoothing values and changing damping values. Results of tests suggest us that the optimal choices according to data at our disposal is smoothing equal to 10 and damping equal to 15. We have made

these choices because model roughness and model variance decrease for smoothing fixed to 1, 3, 5, 7, 9 till damping is equal to 5. After this value, these parameters grow up. Instead, for smoothing fixed to 9 and to 11, damping trend become constant and has its minimum at damping equal to 15. Thus, we have made the choice to fix smoothing to mean value between 9 and 11, that is 10. Figure 4.4 explains what it has been previously written.



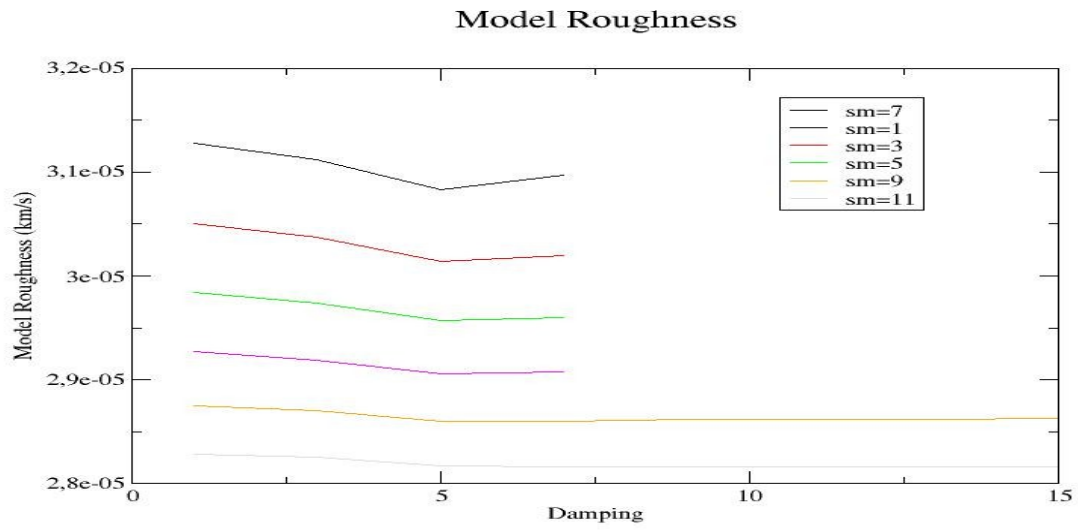


Figure 4.4: Model variance and model roughness for various values of damping fixing values of smoothing

## 4.5 Tomographic images and results

We have made six inversions of our data by means of FMTT. We have stopped the procedure at sixth step because the RMS and the variance of data present in residuals.dat (see paragraph 4.3) do not change in a substantial way as we can see in following table.

<b>RMS (ms)</b>	<b>VARIANCE (s<sup>2</sup>)</b>
849.35	0.72144
765.23	0.58561
762.13	0.58088
758.62	0.57554
756.29	0.57200
756.00	0.57156
754.98	0.57003

**Table 4.5: Description of file “residuals.dat”**

As we can observe in table 4.5, RMS and variance change in a significative way of 10% and of 20% respectively. In last iteration, they change of about 0,01% and about 0,02% respectively. These variations confirm our idea to fix to 6 the number of iterations of FMTT code. Then, we have tested the behaviour of relative residuals for each seismic phase. We can see the results of these tests comparing two histograms where we have inserted the number of rays in function of relative residuals.

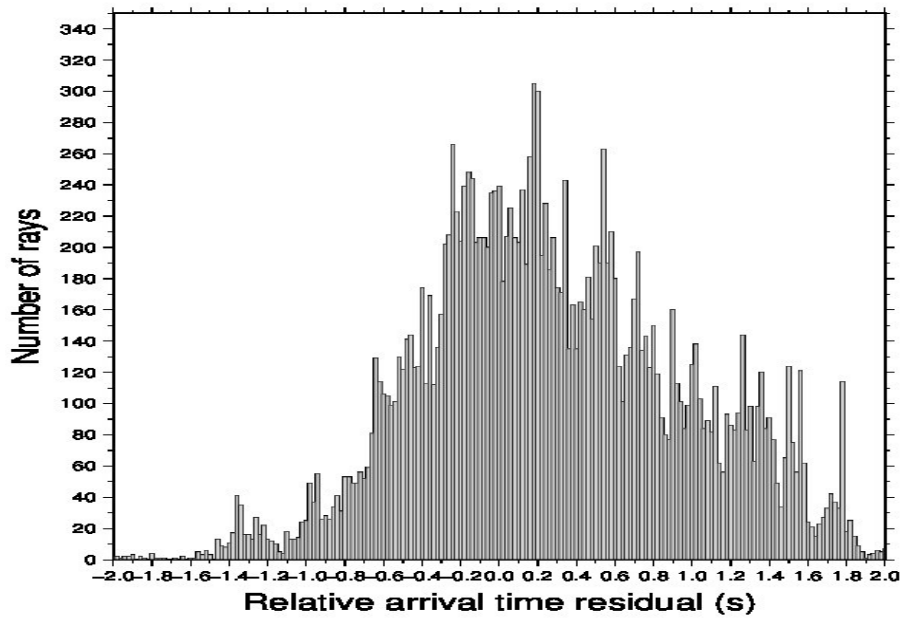
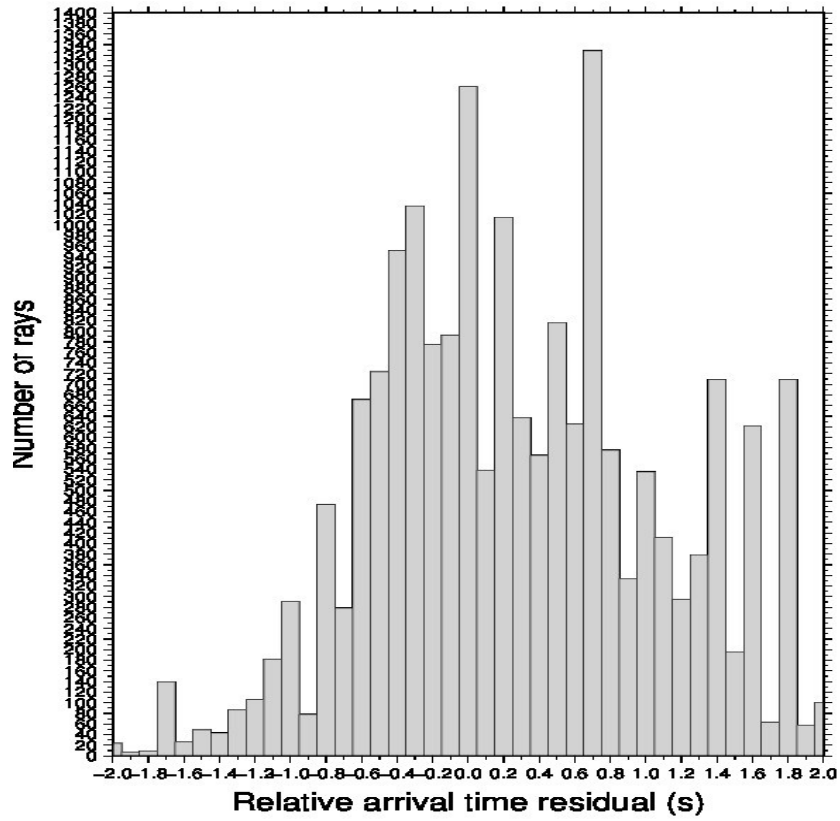


Figure 4.5: Histograms of relative arrival time residuals of observed traveltimes for initial model (up) and final model after six iterations (down)

Two histograms contain only relative arrival time residuals referred to effective inverted traveltimes (see paragraph 4.4). The up histogram is referred to effective inverted traveltimes for initial model, while down histogram is referred to effective inverted traveltimes after six iterations. We can see that the trend of them is more or less similar with a greater quantity of relative arrival time residuals gathered in the range  $[-0.6 \text{ s} ; 0.6 \text{ s}]$  and, as regards to greater deviations, there is a major quantity in the range  $[1.6 \text{ s} ; 2.0 \text{ s}]$  respect to range  $[-2.0 \text{ s} ; -1.6 \text{ s}]$ . But there is an important difference between two figures. In the histogram related to initial model, we can observe that we have a greater frequency at  $0.6 \text{ s}$  rather than  $0 \text{ s}$ . Instead, in the histogram related to model after six iterations, we have that the frequency at  $0.6 \text{ s}$  makes smaller while the frequencies in the range  $[0.2 \text{ s} ; 0.4 \text{ s}]$  increase. This result is coherent with the reduction of RMS and variance of residuals (see table 4.5). Then, we have plotted traveltimes field, to verify the effective ray coverage at various levels of depth and precisely at 50, 150, 250, 400 and 500 km of depth. We can observe them in the following figures, made by GMT.

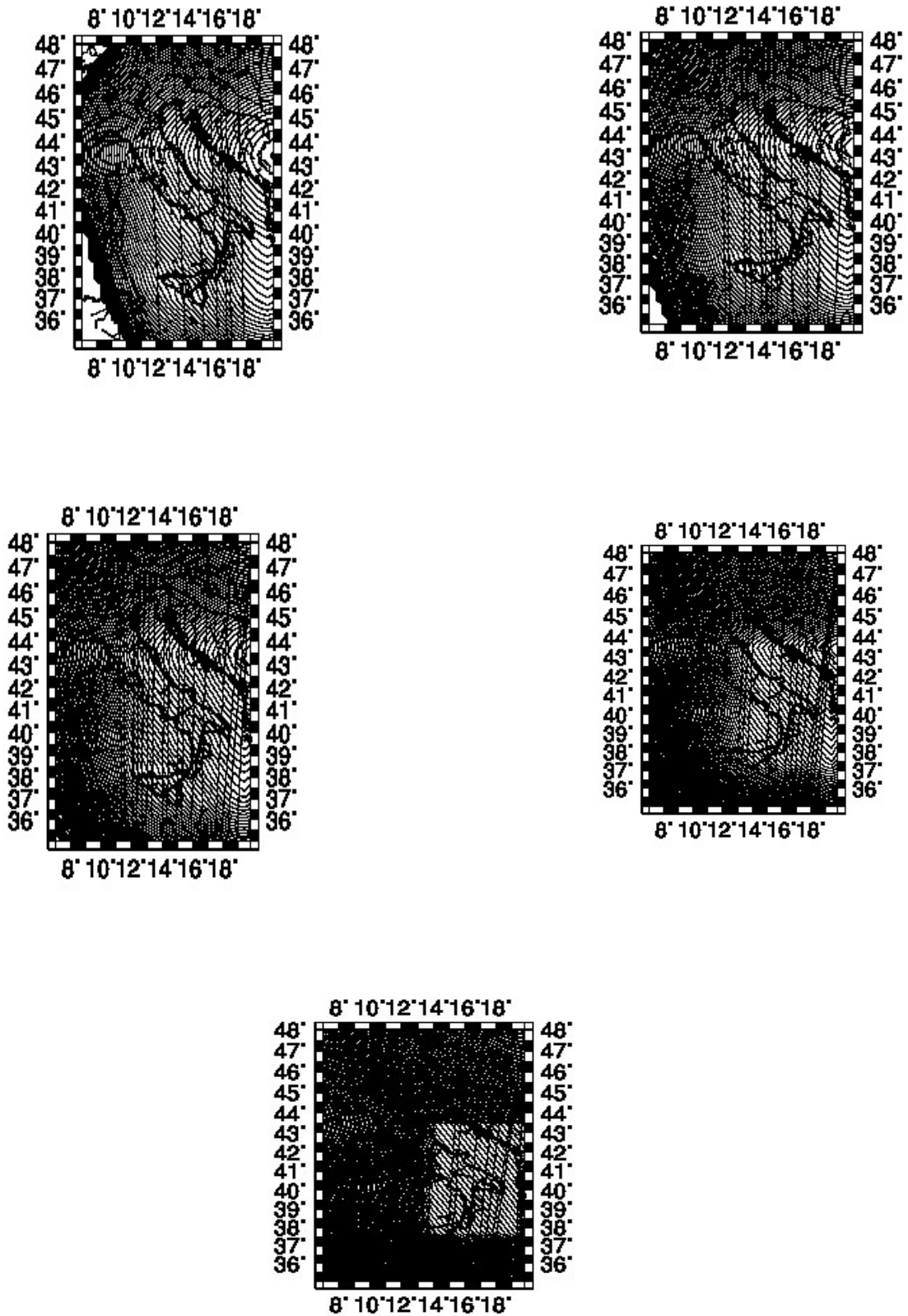


Figure 4.6: Horizontal sections of traveltimes field at various levels of depth. 1st row, 50 km (left) and 150 km (right); 2nd row, 250 km (left) and 400 km (right); 3rd row, 500 km

As we could expect, traveltimes field (precisely, in the pictures we see its iso-contours) increases when depth increases. We can observe that for the area of Southern Tyrrhenian distance among iso-contours is about  $0.2^\circ$  degrees (22 km more or less) for almost all considered levels of depth. Following the gradient of the traveltimes field from each receiver, back to the source, the FMTT allows the computation of ray paths. They are shown in the following image.

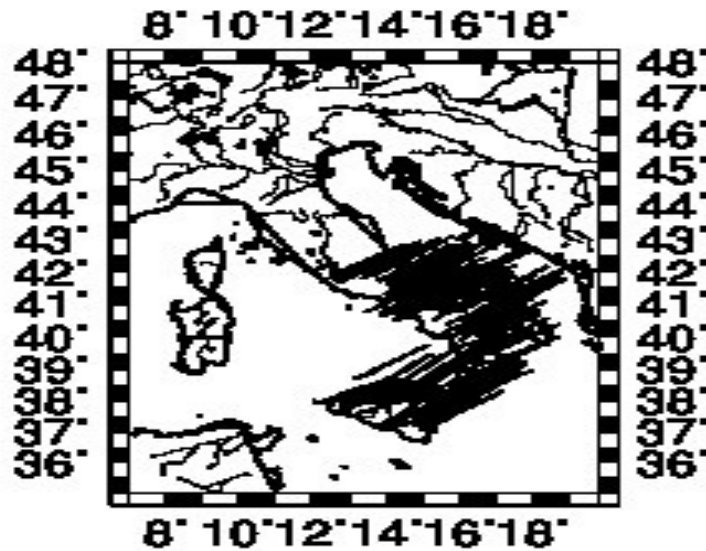
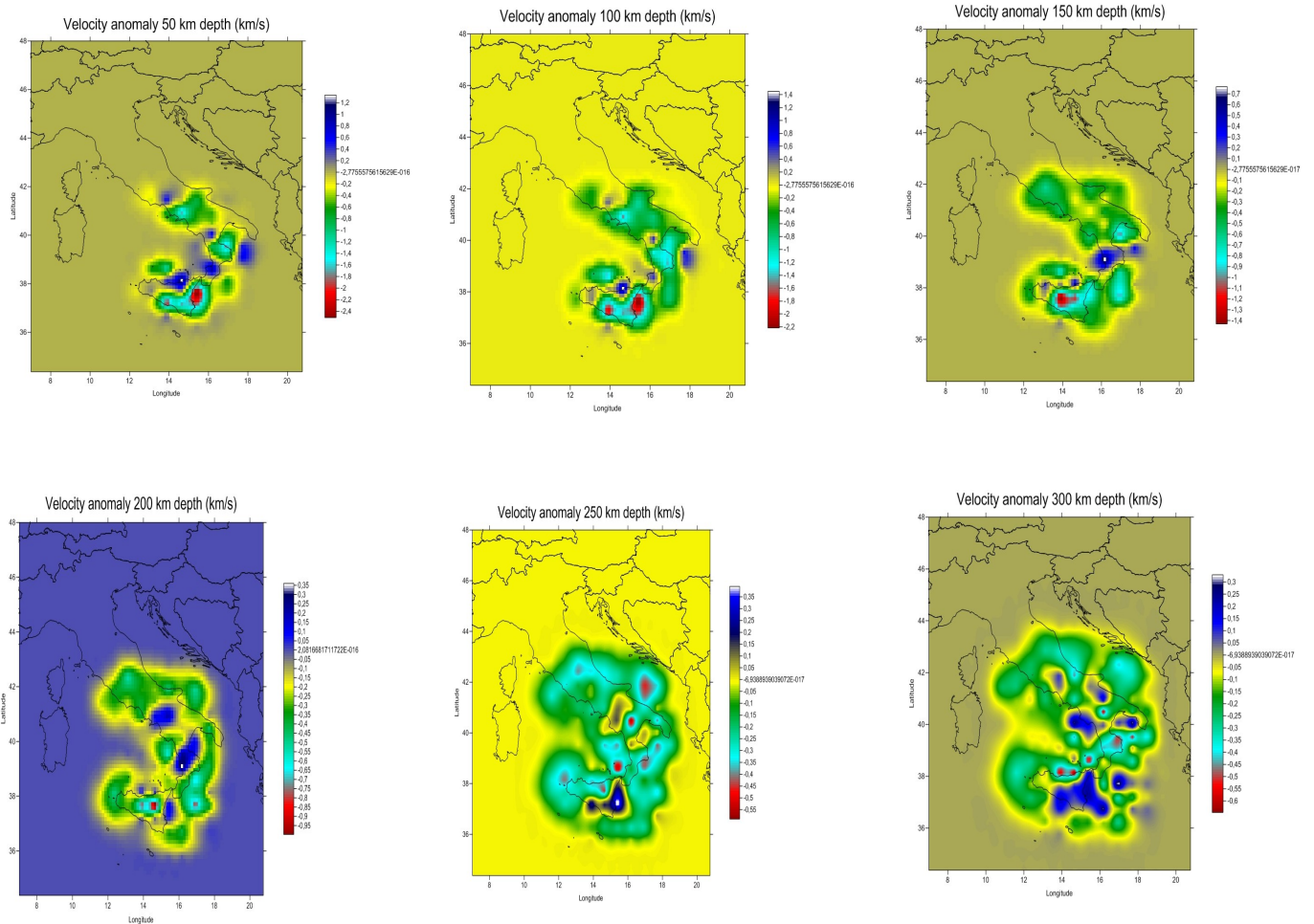
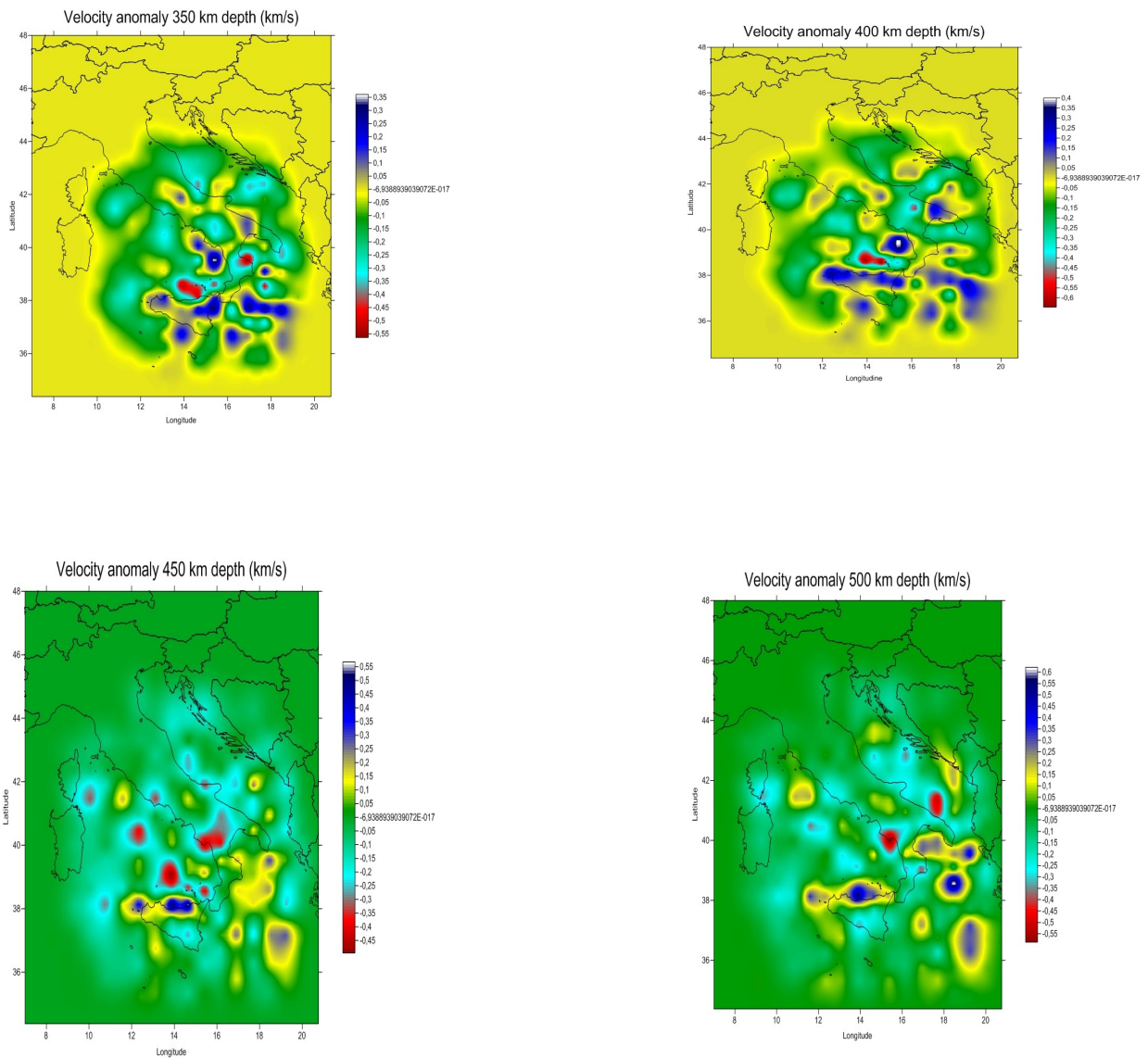


Figure 4.7: Horizontal sections of ray paths

Then, we have plotted tomographic images, where we can observe the velocity anomaly (that is the difference between final velocity model after 6 iterations and starting model) expressed in km/s. We have made 20 horizontal sections regarding a specific depth, starting from 50 km to 500 km with a step of 50 km each other. We have made 8 vertical sections, and precisely 4 NS sections (at fixed longitudes of 14°, 15°, 15,5° and 16,2°) and 4 WE sections (at fixed latitudes of 39°, 39,5°, 40° and 40,5°). All the figures have been realised by Golden Surfer, after having prepared the grids in a legible format for it by means of specific codes written in Matlab.

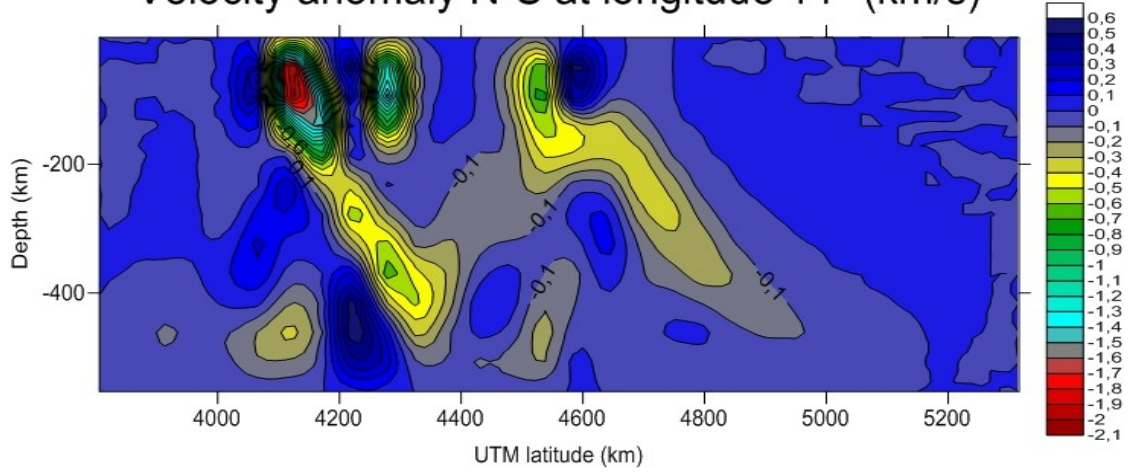




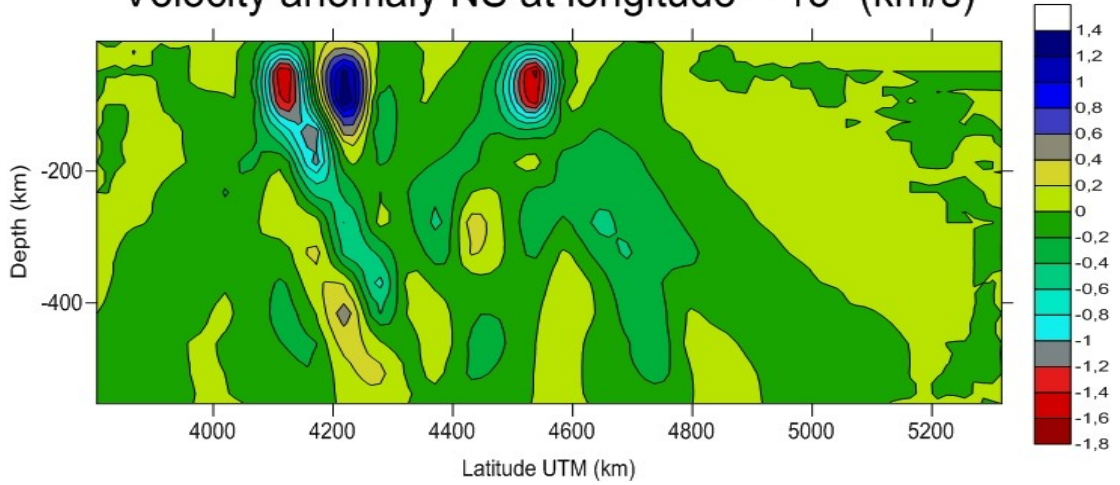
**Figure 4.8: Horizontal sections of velocity anomaly made by Golden Surfer. 1st row: 50, 100, 150 km depth; 2nd row: 200, 250, 300 km depth; 3rd row: 350, 400 km depth; 4th row: 450, 500 km depth**

Following figure regards the NS and WE vertical sections that we have previously mentioned. We want to underline that in these sections we consider the ranges of latitude and longitude expressed in table 4.4 and converted in UTM coordinates.

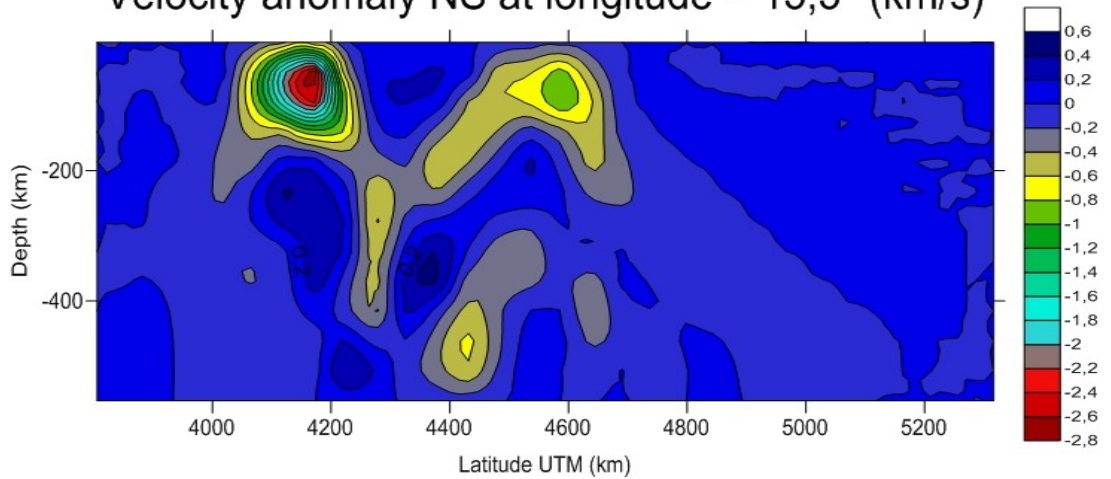
Velocity anomaly N-S at longitude 14° (km/s)



Velocity anomaly NS at longitude = 15° (km/s)



Velocity anomaly NS at longitude = 15,5° (km/s)



### Velocity anomaly NS at longitude = 16°

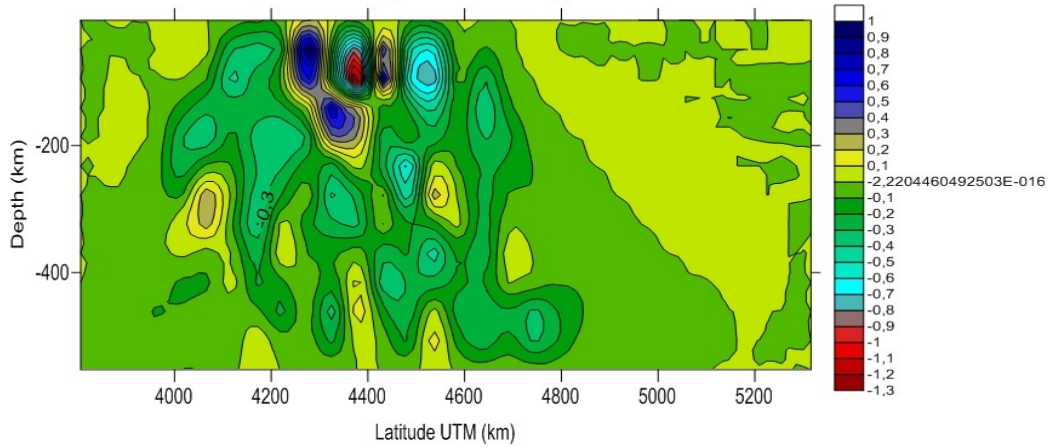
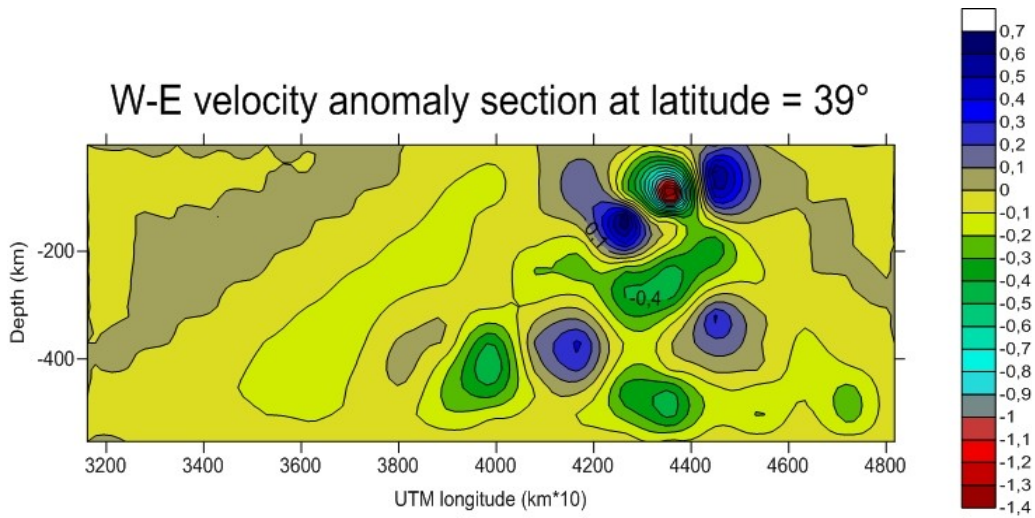
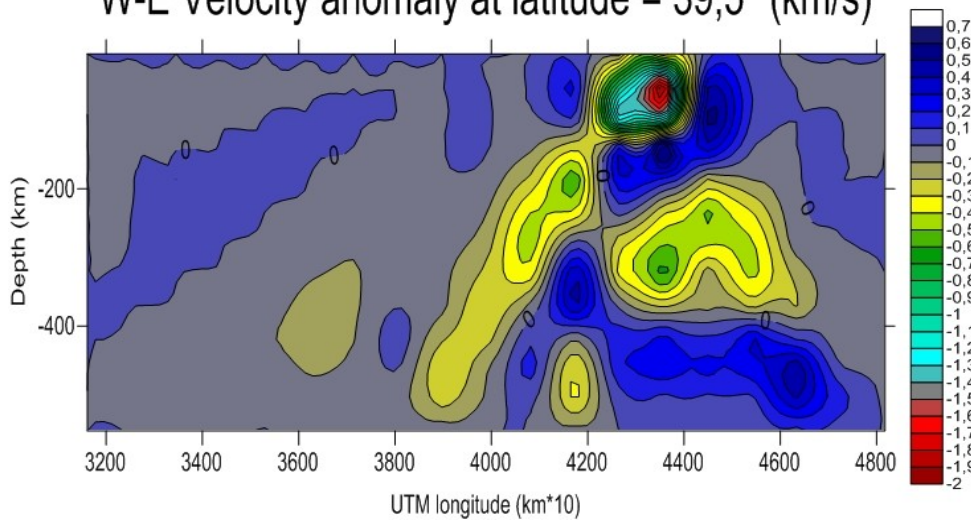


Figure 4.9: Vertical sections NS of velocity anomaly made by Golden Surfer at fixed longitude of 14°, 15°, 15,5° and 16°

### W-E velocity anomaly section at latitude = 39°



### W-E Velocity anomaly at latitude = 39,5° (km/s)



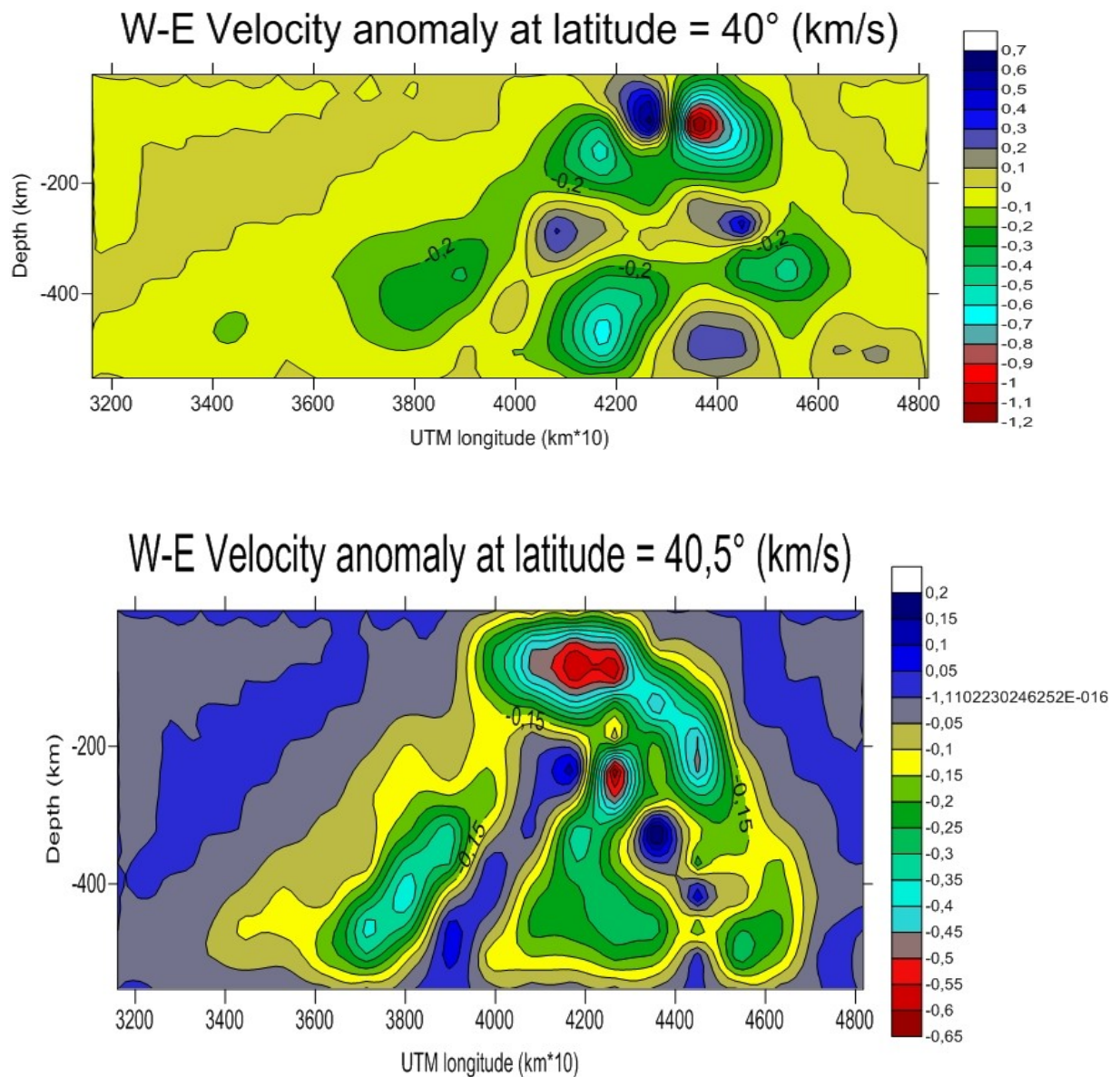


**Figure 4.10: Vertical sections WE of velocity anomaly made by Golden Surfer at fixed latitude of 39°, 39.5°, 40° and 40.5°**

Observing the horizontal sections, we see that at depth of 50 and 100 km there is a HVA (High Velocity Anomaly) of 0.6-0.8 km/s that interests the Calabrian arc and arrives until to northern Sicily beneath Aeolian arc. An other HVA is present in Ionian sea just beneath the southern Apulia. A LVA (Low Velocity Anomaly) is present under Etna zone with a maximum of -2

km/s in Western Sicily. The Calabrian HVA reduced itself in extension at depth of 150 and 200 km, remaining only at centre of Calabria and join it with southern Apulia HVA one. In the rest of zone covered by seismic rays, there are only LVA, except for a strong HVA of 0.4 km/s that appears in northern Campania. At 250 km of depth, the HVA in Tyrrhenian disappear, substituted by a LVA with maximum of -0.5 km/s in some points between Aeolian and Calabria (there is a strong LVA in Adriatic sea in Northern Apulia, too). At 300 km of depth, two strong HVA re-appear in Sicily and along southern Campania with a value of 0.3 km/s, divided by a LVA along Calabrian arc and Aeolian Islands in a range [0.4 ; 0.6] km/s. This situation continues to happen at 350 and 400 km of depth, where there is a new HVA with a maximum of 0.3 km/s in Ionian Sea at SE of Calabria. At 450 and 500 km of depth we can observe only some spots of HVA and of LVA in the zones previously named. This because of a poor ray coverage at those depths.

To understand the lateral extensions of these HVA and LVA, we must interpret the NS and WE vertical sections. For the before mentioned HVA in the range 50-100 km of depth, we can notice a lateral extension of about 100-150 km (for that of Calabrian Arc) and of about 100 km (for that of the Ionian sea, as we can notice for the WE section at slice of fixed latitude of 39° and 39.5°, around at 4500 km\*10 in UTM coordinate). The LVA present in Sicily in the range 50-100 km of depth shows an extension of maximum 150-180 km, as we can appreciate in NS section at slice of fixed longitude at 15.5°. Observing the WE section at fixed latitude of 39.5°, we can see the “link” between Tyrrhenian and Ionian HVA at 200 km of depth

with an extension of 200 km (from 4200 to 4400 km\*10 in UTM coordinate). For the LVA that we can see in Tyrrhenian at 250 km of depth, we can observe it with an extension of 70-80 km at WE section of slice at fixed latitude of 39.5° (from 4000 to 4100 km\*10 in UTM coordinate) and in NS section of slice at fixed longitude of 15° (from 4200 to 4300 km in UTM coordinate). For the 300-400 km range of depth, we can observe – above all from NS slices at fixed longitude of 15° and 15.5° respectively – a very thin LVA with an extension of 60-70 km which divides two HVA (from 4200 to 4400 km in UTM coordinate). For the 450-500 km range of depth, both NS and WE sections show a dappled situation for Southern Tyrrhenian, because of the reason of poor ray coverage at that depth in that zone as previously written.

The reliability of the obtained tomographic images has been tested by a checkerboard test. We have made by means of Golden Surfer software three horizontal sections respectively at 50, 250 and 500 km of depth after six iterations of a model where we have applied on grid a checkerboard of size 34 x 56, where 34 is the double of nodes in longitude (17) and 56 is the double of nodes in latitude (28) (see table 4.4). The comparison with the respective “true” final models at 50, 250 and 500 km of depth symbolize as the reconstructed checkerboard models shows a good coherence with the “true” final models with a maximum discrepancy of 0.2 km/s.

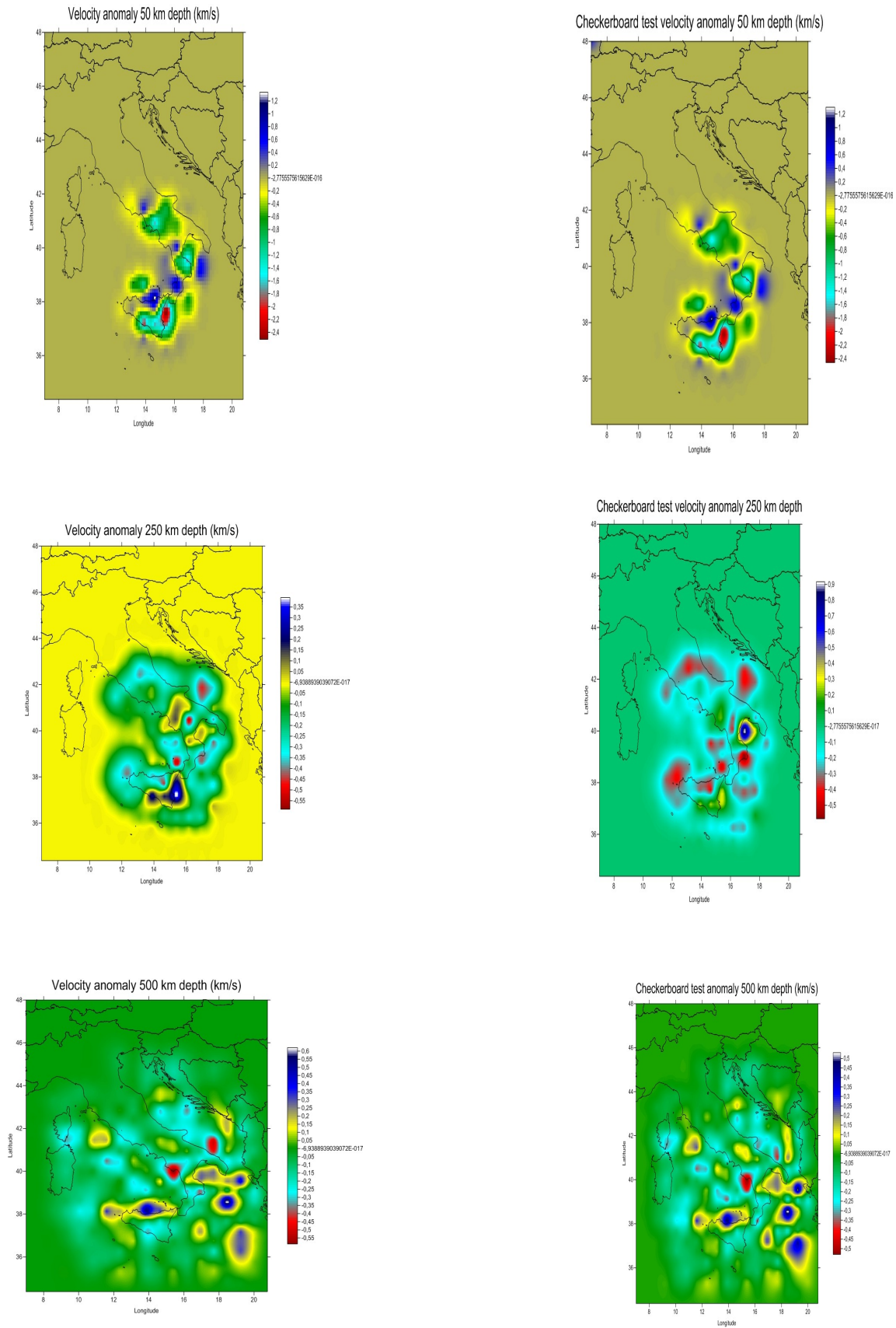


**Figure 4.11: At left of three rows, horizontal sections at 50 (1st row), 250 (2nd row) and 500 km (3rd row) of depth; at right checkerboard reconstructed model at 50 (1st row), 250 (2nd row) and 500 km (3rd row) of depth**

#### 4.6 Comparison with previous works and comments to obtained results

We want compare our results with that obtained by previous works. Above all, we want compare them with results of work “*Teleseismic tomography of the southern Tyrrhenian subduction zone: new results from seafloor and land recordings*”, Montuori et al., 2007. We choose this work as landmark because it is the latest which interests the zone of Southern Tyrrhenian where there is the use of a teleseismic tomography. Our work has in common with Montuori's work not only the specific technique, but also the choice of ak135 as 1-D starting model. Substantial differences are the choice of a grid with an increasing grid spacing in depth (starting from 35 km at depth of 0 km to 75 km at depth of 500 km) instead of our fixed grid spacing (see table 4.4), the use of another algorithm to performing teleseismic tomography technique (that is, minimum travelttime ray tracing algorithm by Steck and Prothero) and the use not only of P phases but of PKPdf phases.

Summarising, Montuori's work show in horizontal sections a high-velocity body extending from the uppermost mantle down to the bottom velocity model with a dip of 70°-75° NW. For the lateral extension, three transversal sections show a lateral extension of about 200 km in the depth range 150-300 km, and with a smaller extension (about 100 km of depth) at uppermost mantle depths. This high-velocity body represents the roll-back subduction Tyrrhenian slab (see paragraph 4.1).

For obtaining a better comparison, we have realised by means of Golden Surfer software, three transversal sections that have the same extremities of

Montuori's ones. Following figures concern respectively the Montuori's transversal sections and ours' ones.

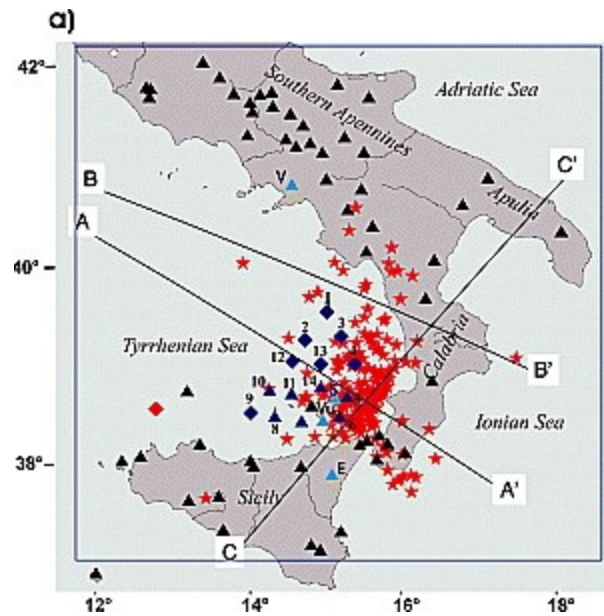


Figure 4.12: The “segments” of the three transversal sections AA', BB' and CC' for Montuori's work and for our work (“Teleseismic tomography of the southern Tyrrhenian subduction zone: new results from seafloor and land recordings”, Montuori et al., 2007)

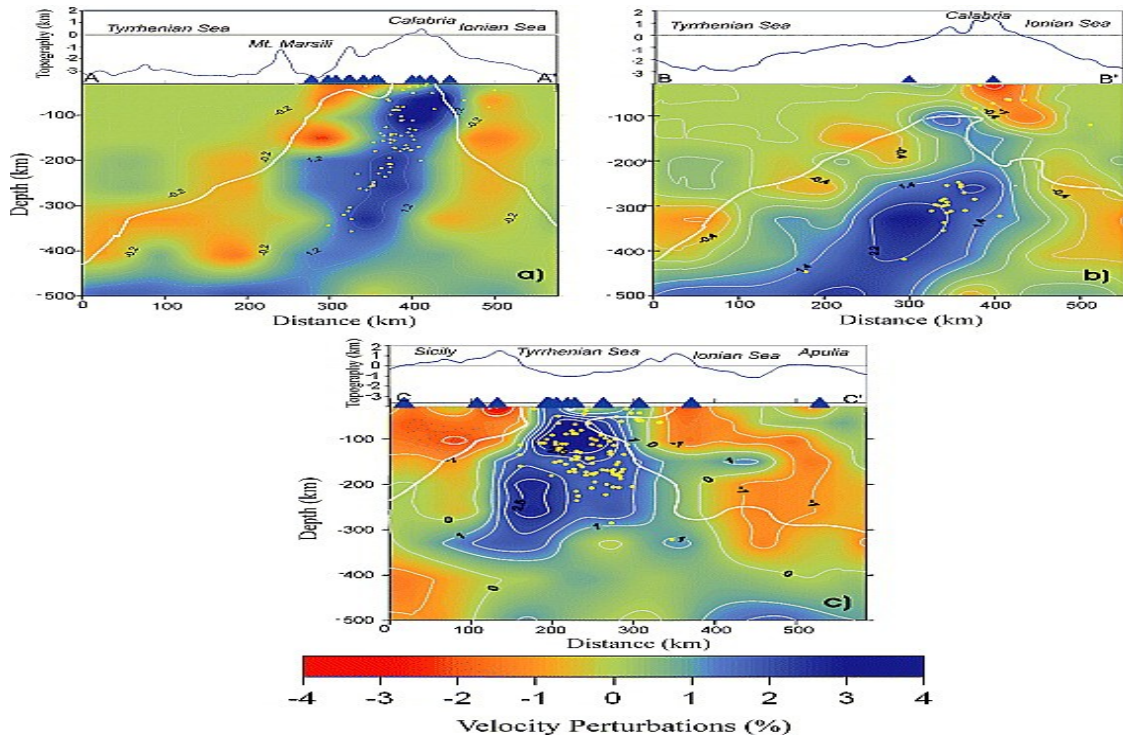
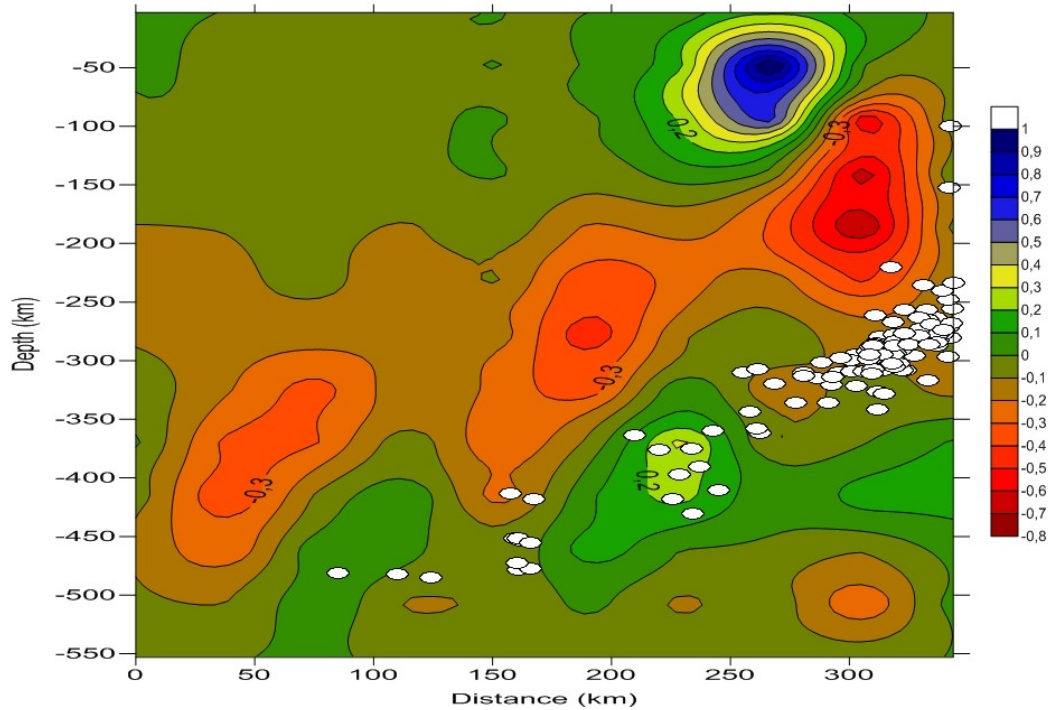
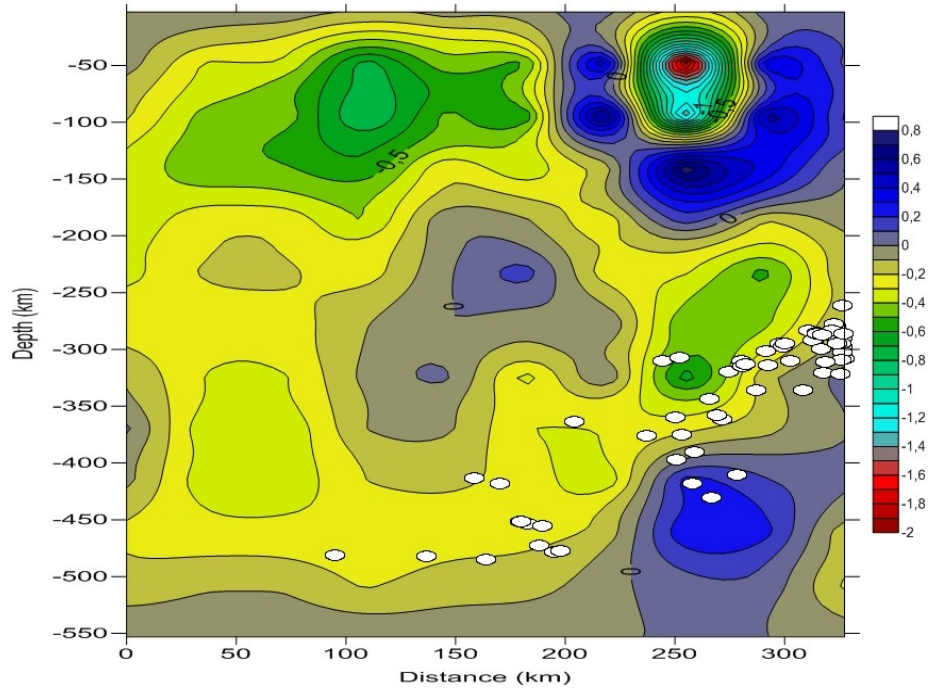


Figure 4.13: Images of the three transversal sections AA', BB' and CC' for Montuori's work ("Teleseismic tomography of the southern Tyrrhenian subduction zone: new results from seafloor and land recordings", Montuori et al., 2007)

### Transversal velocity anomaly section AA' (km/s)



### Transversal velocity anomaly section BB' (km/s)



### Transversal velocity anomaly section CC' (km/s)

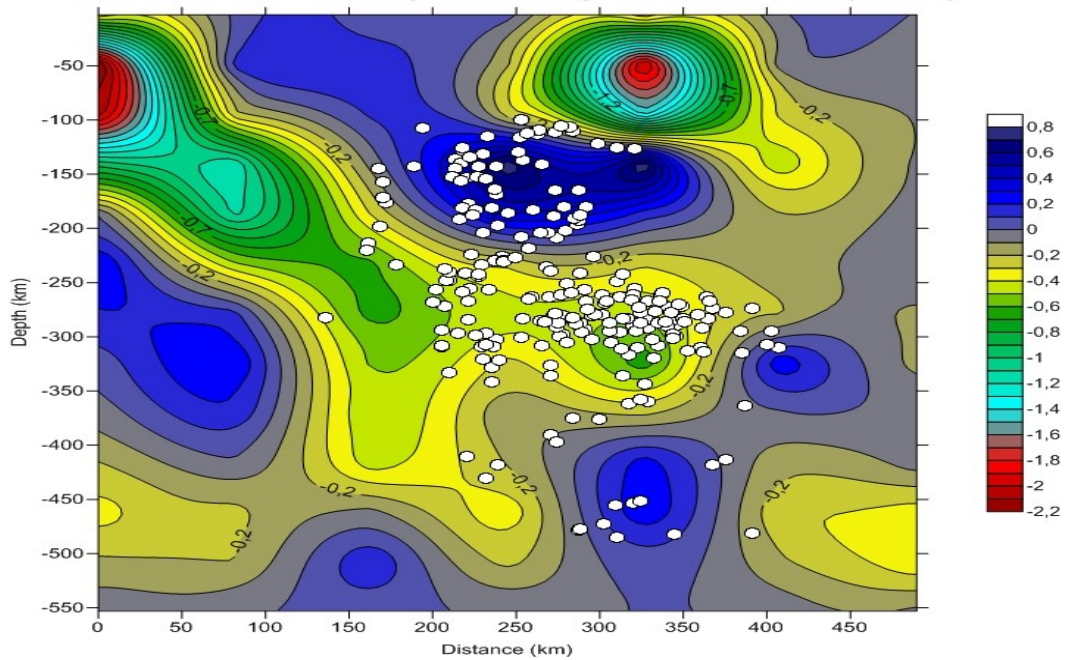


Figure 4.14: Images of the three transversal sections AA', BB' and CC' for our work

Both for Montuori's transversal sections and for ours transversal sections, there is the presence of dots which symbolize the deeper seismicity of Southern Tyrrhenian (in our case, they are the sources of events recorded by ISC seismic stations in a period from 1964 to 2003). Comparing the our transversal sections with Montuori's one we first notice a substantial coherence with the seismicity. Then, we notice a good coherence with the collocations and the spatial orientation of two HVA respectively in [0 ; 250] km depth interval and in [400 ; 500] km depth interval. And there is a good coherence for the lateral extensions of these two HVA. This for all three transversal sections, but in particular for CC' transversal sections, where we can notice a maximum lateral extension of HVA at 150-200 km of depth of about 200 km both for Montuori's work and for our work. Thus, we can interpret these two HVA as the evidence of the Tyrrhenian slab previously mentioned. Another coherence is the presence of two LVA that surround the HVA in two depth intervals previously written, to confirm the idea of a three-dimensional circulation of asthenospheric flow caused by retreat and roll-back of the slab.

The big difference with Montuori's work is a sort of “slab” interruption which we verify in depth interval [250 ; 400] km. The LVA that we observe both in horizontal and vertical sections (see previous paragraph), has observed in three transversal sections, too. This sort of “slab window” has been verified by two previous local Southern Tyrrhenian tomographies: ***“The southern Tyrrhenian subduction zone: Deep geometry, magmatism and Plio-Pleistocene evolution”*** Chiarabba et al. (2008), and ***“Seismic velocity structures of southern Italy from tomographic imaging of the***

***Ionian slab and petrological inferences***” Calò et al. (2012). Although there are significant differences between the collocation of these “windows slab”. According to Chiarabba's results, it is situated in a depth interval between 100 and 300 km and it divides two independent high  $V_p$  slabs lie beneath the Neapolitan region and the southern Tyrrhenian sea. Chiarabba suggests that this 150 km-wide slab window opened after a tear occurring within a composite subduction system, formed by the Apulian continental lithosphere and the Ionian oceanic slab. Instead, Calò – although his tomography reaches a maximum depth of 180 km – observes presence of lateral and vertical tears in slab. According to him, they could be interpreted as traces of fluids released during the subduction process. The presence of “slab window” in our work at depth interval [250 ; 400] km should feel like to confirm Chiarabba's hypothesis. There is a good coherence with the extension of this window, that is 150 km. There is not, instead, a good coherence with the depth collocation of this window. But this difference could be depend on the different tomographic technique, local for Chiarabba and teleseismic for us, on the different typologies of gathered data, ecc.... Anyway, the review of our data joined with other teleseismic data and other different tomographic techniques (attenuation in particular) represents the most important future development that this work could have. It will be important to compare this teleseismic tomography and its future updates with local tomographies. At this proposal, next paragraph describes a comparison with a local tomography of Southern Tyrrhenian.

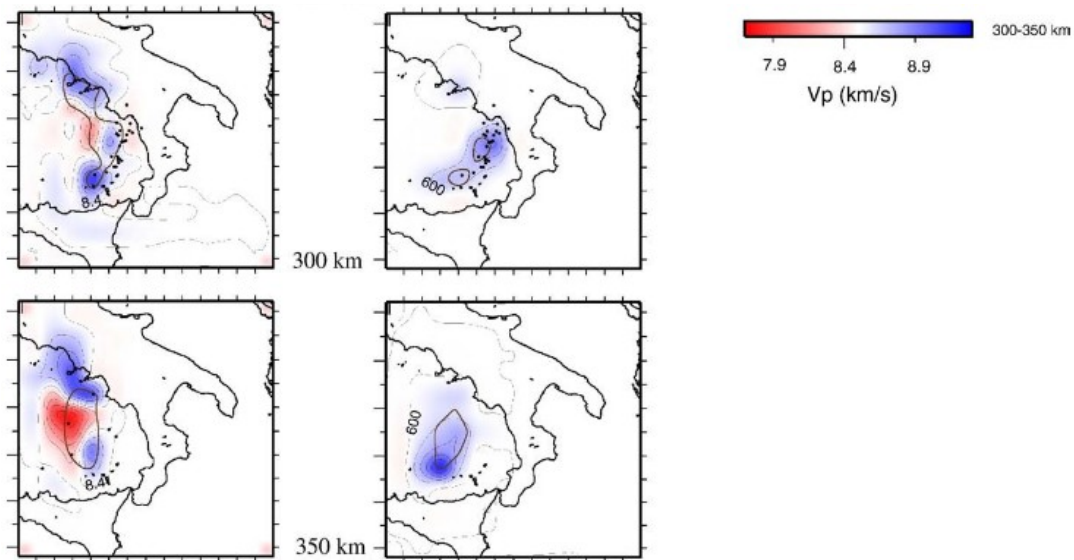


Fig. 3 (continued).

Figure 4.15: Images of the horizontal sections at 300 and 350 km of depth in mentioned Chiarabba's work (“The southern Tyrrhenian subduction zone: Deep geometry, magmatism and Plio-Pleistocene evolution”, Chiarabba et al., 2008)

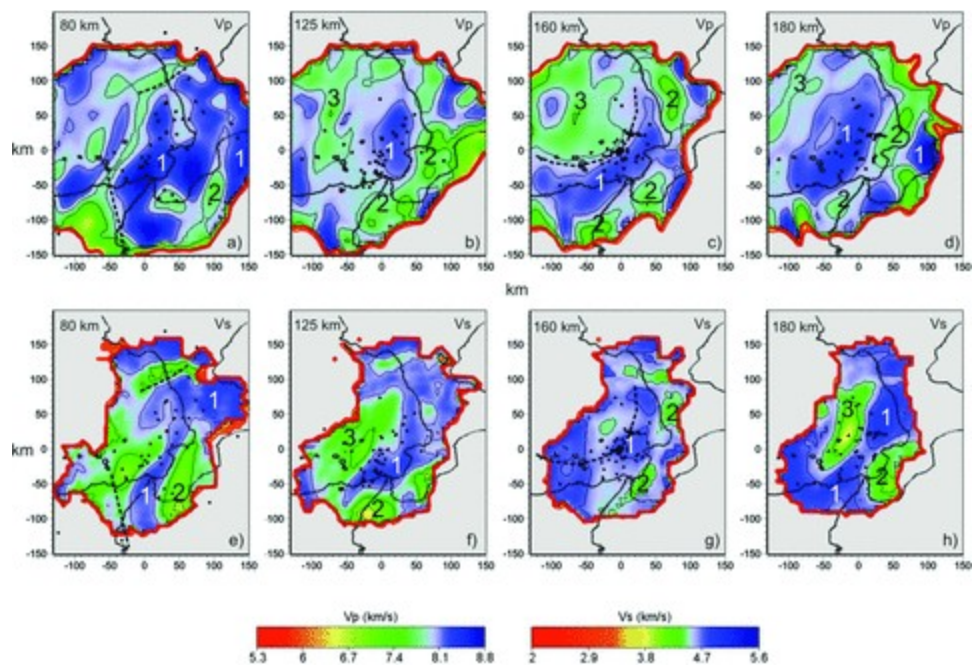


Figure 4.16: Images of the horizontal sections in mentioned Calò's work (“Seismic velocity structures of southern Italy from tomographic imaging of the Ionian slab and petrological inferences”, Calò et al., 2012)

## 4.7 A comparison with a local tomography of Southern Tyrrhenian

In a way to obtain a more appreciable estimate of our results, we have made a comparison between them and results of a local tomography of Southern Tyrrhenian, made by Cristina Totaro (University of Messina) in April 2017. This tomography has been made using LOTOS code (Koulakov, 2009). The dataset is made up of 2797 local seismic events registered by 394 ISC southern Italy seismic stations in a period from 1981 to 2014. The gathered local seismic events satisfy following parameters:

- Depth included between 20 km and 400 km
- Magnitude  $\geq 2.0$
- Each seismic event must be recorded by almost 12 stations (summing P and S)

Starting 1D model has been obtained by Orecchio & al. Model, BGTA 2011. Choice of it has been made repeating a location procedure through a dozen of different 1D models parameterized with 4-6 parameters (constant  $V_p/V_s$  ratio and 3-5 velocity values in different depth levels). Model which supplies the maximum number of events and picks and minimum average deviation of residuals has been choiced. The entire dataset is made up of 47,586 P-arrival times and 19,938 S-arrival times with maximum residual of 1.5 seconds (P-wave) and of 2 seconds (S-wave).

The LOTOS inversion procedure consists of a 3D ray tracer based on the bending method to obtain the seismic events sources localizations. For 3D

velocity distribution, it is parameterized with a set of nodes distributed in the study area according to the distribution of rays. The grid spacing is not fixed, but it is variable according to the data density. Only constrain is that it cannot be smaller than the predefined value of 10 km. The inversions have been performed changing basic orientation to the grid ( $0^\circ$ ,  $22^\circ$ ,  $45^\circ$  and  $67^\circ$  have been the used basic orientations). This choice has been made to avoid any bias related to the basic orientation of the grid. The results computed for these grids are averaged in a regular mesh which is then used as an updated 3D velocity model in the successive iteration. The inversion is performed simultaneously for the P- and S- velocity distributions, source corrections (four parameters for each source) and station corrections and it is obtained using the LSQR algorithm (Paige and Saunders, 1982; Nolet, 1987). Solution is regularized by minimizing the gradient between neighboring nodes. The value of smoothing coefficients is estimated considering the results of synthetic modeling.

In the following figure, we can see the results of this local tomography. At 30 km of depth, there is a low velocity belt from the Southern Apennines to Northern Sicily. It indicates the presence of lower continental crust in Sicily and a probable crustal reduplication in Calabria (top of Ionian slab subducting Tyrrhenian crust). At 50 km of depth, there is a High Velocity Anomaly that should corresponds to ionian lithosphere with an extension to Tyrrhenian off-shore in Southern Calabria. It should indicate the more advanced part of Ionian slab. The more the depth increases, the more this High Velocity Anomaly extends and it advances towards Tyrrhenian in NW direction.

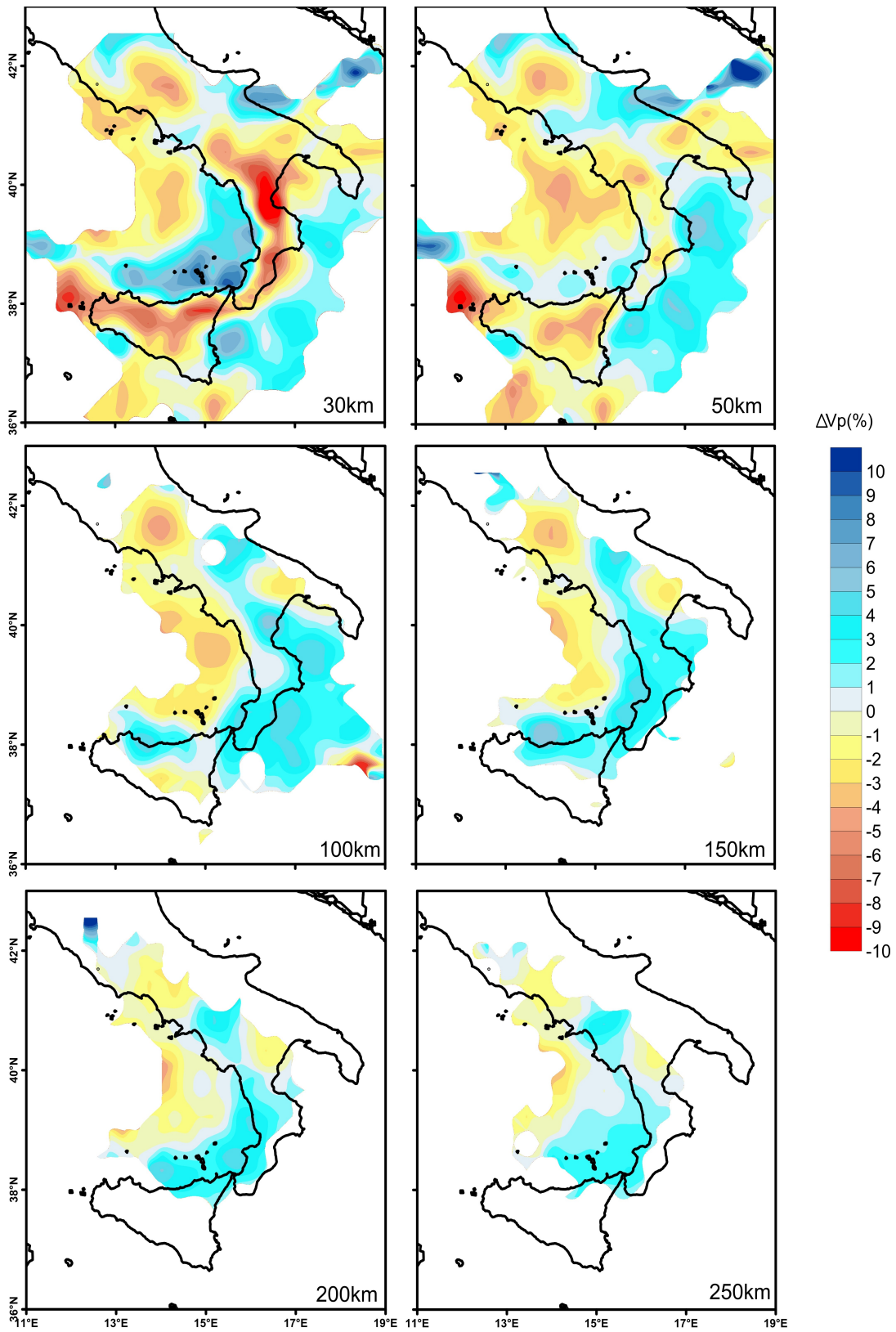


**Figure 4.17: results of a local tomography of Southern Tyrrhenian (Totaro, 2017)**

## Conclusions

We have performed a teleseismic tomography of Southern Tyrrhenian, one of the most interesting area to study in Geophysics. This because in that area a process of roll-back subduction, which provoked the opening of this basin 10 Ma in Tortonian Age, is still ongoing along Calabrian arc. We can observe it by means of several local seismic tomographies that have investigated that area a body of high seismic velocity in Calabrian zone which represents subducted Ionian lithosphere, confined to the southwest by the Malta Escarpment. But, since the maximum reached depth for local seismic tomographies is about 250-300 km, the development of a teleseismic tomography is useful to reach greater depths, until 500 km. Our teleseismic tomography has made use of arrival times of 1929 teleseisms recorded by 122 Southern Italy ISC (International Seismological Centre) with a total of 18515 P phases (although original database was richer). Software FMTT (Fast Marching Teleseismic Tomography, N. Rawlinson, 2006) has been used for inversion of these arrival times. After various tests on model roughness and on model variance, we have implemented the more correct parameters of smoothing and damping for code, fixing them respectively to 10 and to 15. And we have implemented a grid of 0-500 km in depth, 7°E-20°E in longitude and 35°-48° in latitude, with a grid spacing of 50 km in depth, 0.8 degrees in longitude and 0.4 degrees in latitude. Consequently, grid nodes are 10 in depth, 17 in longitude and 28 in latitude. We have implemented this code for six iterations, stopping it when there are not more significant changes

in RMS and in variance of theoretical traveltimes (at last iteration, we have a RMS of 754.98 ms and a variance of 0.57003 s<sup>2</sup>).

The tomographic images have been realised by means of Golden Surfer software. We have made 10 horizontal sections of final model from 50 km of depth to 500 km of depth, with an interval of 50 km of depth from each other. We have made 8 vertical sections, 4 NS vertical sections at fixed longitude respectively of 14°, 15°, 15.5° and 16° and 4 WE vertical sections at fixed latitude respectively of 39°, 39.5°, 40° and 40.5°. Then, we have made 3 transversal sections, choosing as extreme points of 3 segments for them the same chosen by Montuori et al. (2007), in their work that is another teleseismic tomography of Southern Tyrrhenian. This work, together with Chiarabba et al.'s work (2008) and Calò et al.'s work (2012), has been chosen as landmark for a comparison of results.

Summarising, our horizontal sections show an evolution of the high-velocity body that represents the Tyrrhenian slab. Both at depth of 50 km and at depth of 100 km, it interests the Calabrian arc and arrives until to northern Sicily beneath Aeolian arc with a maximum of 0.6-0.8 km/s. At these some depths, other HVA is present in Ionian sea just beneath the southern Apulia. At depth of 150 and 200 km, the Calabrian HVA reduced it, remaining only at centre of arc and join it with southern Apulia HVA one. At 250 km of depth, there is a sort of “transition” because we do not notice more in Southern Tyrrhenian HVA, but we observe a LVA with maximum of -0.5 km/s in some points between Aeolian and Calabria. In depth interval included between 250 km and 400 km, the situation in

Southern Tyrrhenian becomes the following one. There are two strong HVAs in northern Sicily and along southern Campania with a value of 0.3 km/s, divided by a LVA along Calabrian arc and Aeolian Islands in a range [0.4 ; 0.6] km/s. At 450 and 500 km of depth, the situation is not well defined because we can observe only some spots of HVA and of LVA spread out on entire grid in a not better specified way. This because of a poor ray coverage at those depths.

Extensions of HVAs and LVAs previously mentioned have been estimated by means of vertical and transversal sections. Through the first ones, we observe an extension of 100-150 km of HVA along Calabrian arc in 50 km and 100 km of depth and it reaches a maximum extension of 200 km when there is the “fusion” with the Ionian HVA at 200 km of depth. Through the second ones, we want to obtain a direct comparison with Montuori's work, as previously written. We observe coherence with the spatial position of sources of typical Tyrrhenian seismic events and with extensions, between 150 and 200 km, (and spatial orientation, too) of two HVAs present respectively in [0 ; 250] km depth interval and in [400 ; 500] km depth interval. As Montuori's work, we notice the presence of two LVAs that surrounding the HVAs in two depth intervals previously written. A result that could be interpreted as the idea of a three-dimensional circulation of astenospheric flow provoked by slab roll-back. The strong different result is the presence of a LVA in [250 ; 400] km depth interval with an extension of 100-150 km that practically divides into two parts the Tyrrhenian slab, one in Neapolitan region and other in southern Calabria-northern Sicily region. This evidence is partially in agreement with Chiarabba (2008), that

in his work showed the presence of a “window slab” with an extension of 150 km, in a depth interval included between 100 and 300 km of depth. Therefore, there is an agreement with spatial extension of this “window slab” but there is not an agreement with its collocation in depth. The presence of this “window slab” could be interpreted as a tear in which unperturbed mantle insert itself. The occurrence of this “window slab”, which represents the most interesting result of this work, could be a starting point for potential future developments. This because this result could become a relevant “talking point” in geophysical community. We need only consider the example of several local tomographies of Southern Tyrrhenian, with present different results from each other. In this work, we mentioned two examples of that previously written. Totaro's local tomography (maximum reached depth 250 km) shows a compact HVA that extends and advances towards Tyrrhenian in NW direction. Calò's local tomography, instead, reveals the occurrence of vertical and lateral tears in Tyrrhenian slab. Two straightforward examples that explain as the area of Southern Tyrrhenian presents lots of aspects, and many of them are yet to study and to interpret.

## Appendix 1

### The *ak135* velocity model

The *ak135* velocity model is one of the most widespread 1-D velocity model in Geophysics. It was developed by **B.L.N Kennett**, **E.R Engdahl** and **R. Buland** in 1995. They elaborated this model for improving their previous 1-D velocity model, the *IASP91*. The model – that is available at following link <http://rses.anu.edu.au/seismology/ak135/intro.html> – contains 8 travel time tables. Five tables for body waves according to 5 distinct ranges of epicentral distance. Respectively, they are: 0°-25°, 25°-50°, 50°-75°, 75°-100° and 100°-124°. The remaining three tables are for core phases (even these one according to 3 distinct ranges of epicentral distance). Respectively, they are: 110°-135°, 135°-160°, 160°-180°. Then, there are 12 graphs which represent the trend of different seismic phases according to 4 depths: 0 km, 100 km, 300 km and 600 km. For each depth, there are three graphs: traveltime as a function of epicentral distance, slowness (reciprocal of seismic velocity) as a function of epicentral distance, traveltime as a function of slowness.

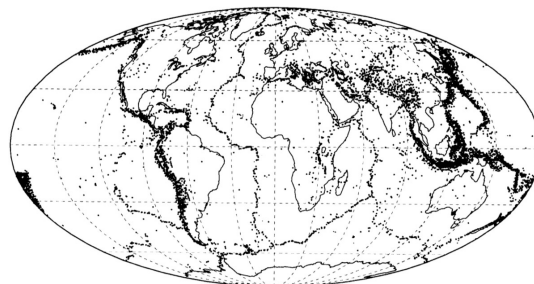


**Figure A.1.1: Geographical distribution of selected events used in constructing the smoothed empirical traveltimes for *ak135* velocity model (from “Constraints on seismic velocities in the Earth from traveltimes”, Kennett, Engdahl & Buland, *Geophys. J. Int* (1995), 122, 108-124)**

Using **ISC** (International Seismological Centre) catalogue of events and arrival times (computed by means of Jeffreys & Bullen traveltime tables, 1940), in 1991 Kennett & Engdahl developed the IASP91 model, for which the mantle velocity distributions were designed to match the observed times of P and S seismic phases, while the core structure was taken from **PEM** (Parametric Earth Model, **Dziewonski, Hales & Lapwood, 1975**). Subsequently, in 1993, **Morelli & Dziewonski** developed the velocity model **SP6**, including PKP and SKS (see Chapter 3) observations in order to provide an improved core structure. But the observed differential times between the branches of PKP measured from the same digital seismograms were in disagreement with those one both of IASP91 and of SP6.

An other problem was the attempt of constraining the compressional wave velocities in the core using body wave arrivals. For obtaining this goal, a high confidence in both the P and S velocity distributions in the mantle occurred. But this problem is compounded by the traveltime cross-over between S and SKS near  $80^\circ$ , which makes it difficult to obtain direct information on the S velocity distribution in the lower part of the mantle. To deal with these problems, Kennett & Engdahl developed new empirical traveltime curves for the major seismic phases. They derived them from the ISC catalogues by relocating events by using P readings, depth phases and IASP91 traveltimes. This set of smoothed empirical times was then used to construct a range of radial velocity profiles based on different measures of the level of fit between the empirical times and the predictions of the models. These misfit measures have been constructed by using a

weighted sum of  $L_2$  misfits for individual phases. The weights were chosen to provide a measure of the likely reliability of the picks for the different phases. By combining information from different phase branch selections, attention can be focused on selected aspects of the velocity structure. In order to assess the potential resolution of velocity structure, Kennett & Engdahl carried out a non-linear search procedure in which 5000 models have been generated in bounds about ak135. Misfit calculations are performed for each of the phases in the empirical traveltime sets. The models are then sorted using different overall measures of misfit, and the best 100 models for each criterion are displayed in a model density plot.

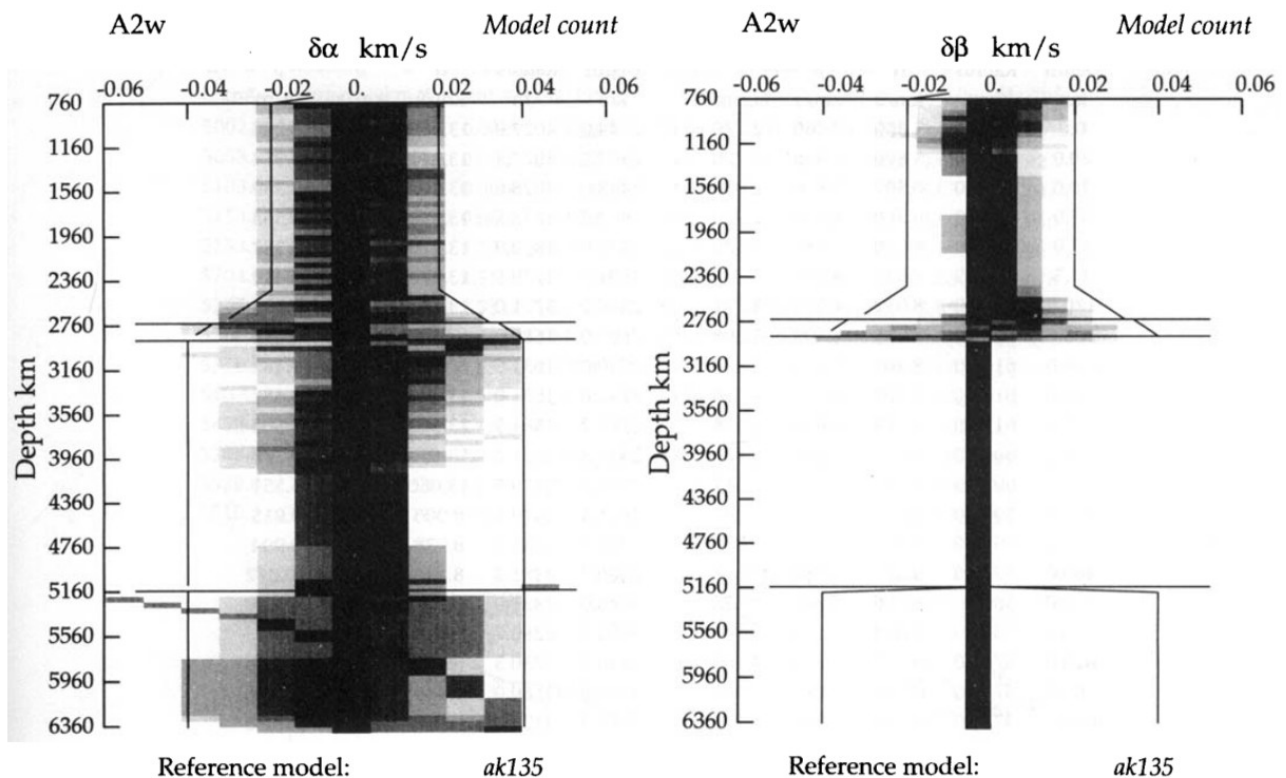


Figure A.1.2: Model density plots for the best 100 models for both P and S wavespeeds (respectively,  $\alpha$  and  $\beta$ ) for a specific misfit measure (A2w) (from “Constraints on seismic velocities in the Earth from traveltimes”, Kennett, Engdahl & Buland, *Geophys. J. Int.* (1995), 122, 108-124)

To solve the two IASP91 previously written problems, Kenneth & Engdahl took the SP6 core structure to create a new composite model that they named *IASP93A*. The S and PKP residuals were reduced as expected, but the misfit for SKS increased and the differential time behaviour corresponded directly to SP6. Thus, Kenneth & Engdahl tried to reconcile the P and S refracted phases from the mantle with the reflections from the core-mantle boundary. They reached this goal by means of a slight modification in the P and S velocity distribution in the lower mantle together with a 0.5 km reduction in core radius from the SP6 value to 3479,5 km. Also, they decreased the P velocity in the lowermost mantle below the IASP91 value but not by as much as in SP6. This last procedure was applied to reduce the PcP misfits. After, they modified the core structure to give a good fit to the core phases. The aims of this particular moment in the development of model were: considering the constraints imposed by SKS and SKKS phases and matching to the differential times for the PKP phases. First aim was reached slight modifying the traveltime in the mantle for S phase in SP6. For the second aim, Kenneth & Engdahl proposed a structure similar to that one realised by Song & Helmberger (1994), where there was a consideration of an anisotropy in the boundary between the inner core and the outer core, where the velocity gradient is relatively low. Such a model had a satisfactory pattern of differential times.

A large number of models were tested during this construction process in order to assess the trade-offs between different aspects of the velocity structure. For each model, a full calculation of the traveltime residuals was

carried out for all phases, and for promising models differential-time residual plots were also prepared. The ak135 model was the product of this procedure.

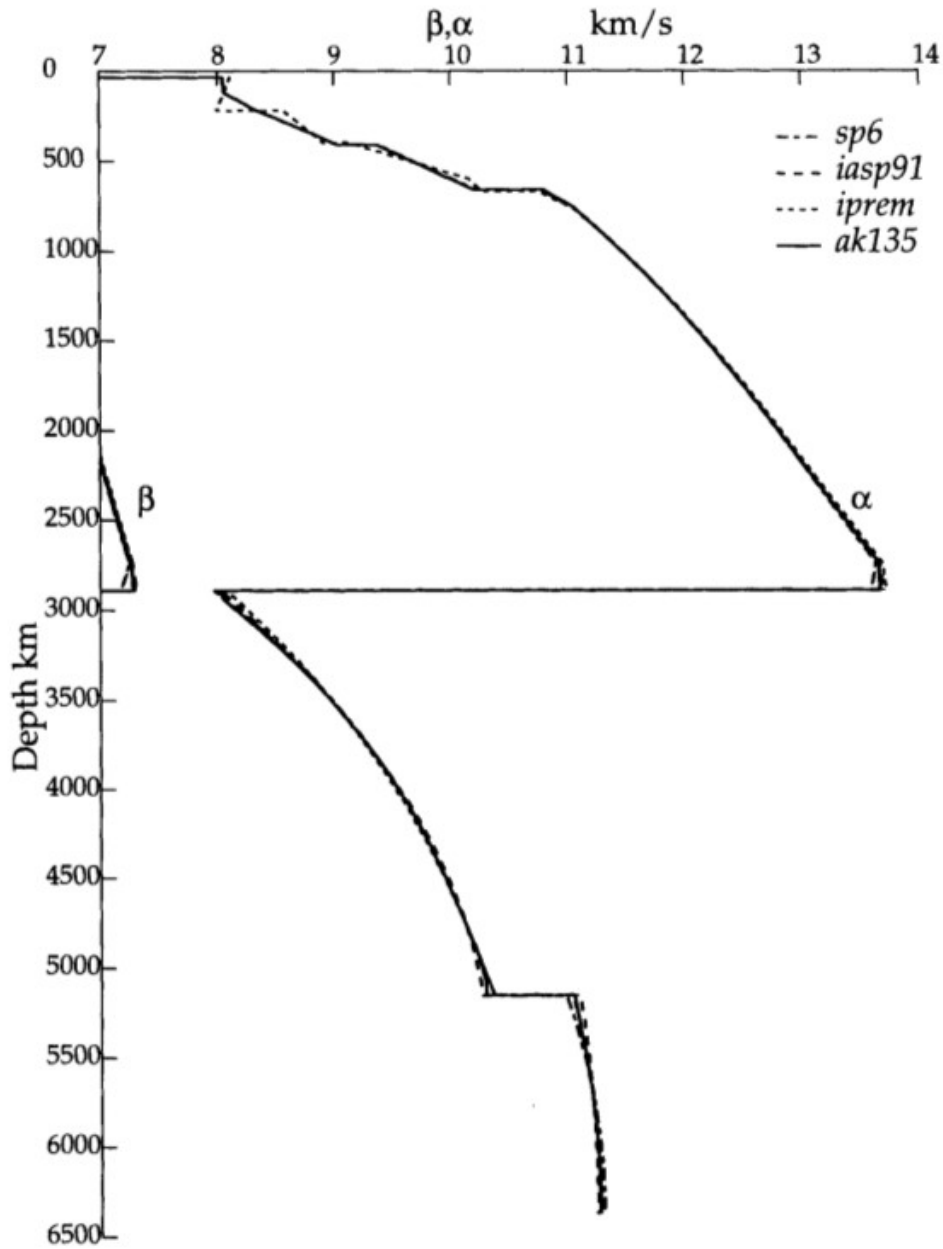


Figure A.1.3: Comparison of model ak135 for both P and S wavespeeds (respectively,  $\alpha$  and  $\beta$ ) with other 1-D velocity models (from “Constraints on seismic velocities in the Earth from traveltimes”, Kennett, Engdahl & Buland, *Geophys. J. Int* (1995), 122, 108-124)

## Appendix 2

### Glossary of mathematical and geophysical notations used in thesis

***B-spline interpolation:*** A B-spline (where B stands for “basic”) interpolation is a kind of interpolation which differs from polynomial one because it divides the entire interval of  $N$  values to interpolate in more subintervals  $l_k = [x_k ; x_{k+1}]$  with  $k = 1, \dots, N-1$ . For each of them, interpolating polynomial has a different form, but they must be continuous at knots of various subintervals. A theorem states that every B-spline function of a given degree, smoothness and domain partition, can be uniquely represented as a linear combination of B-splines same degree and smoothness, and over that same partition.

***Euler's theorem:*** This theorem, developed by the Swiss scientist Leonhard Euler in 1775, states that if there is a rigid body and a point which we fix on it, any its displacement is equivalent to a single rotation about some axis that runs through the fixed point. That means that the composition of two rotations is a rotation and therefore rotation has a group structure. In linear algebra terms, the theorem states that, in 3D space, any two Cartesian coordinate system with a common origin are related by a rotation about some fixed axis. This also means that the product of two rotation matrices is again a rotation matrix and that for a non-identity rotation matrix it must happen that: one of its eigenvalues is 1 and the other two are -1, or it has only one real eigenvalue which is equal to unity. The eigenvector

corresponding to this eigenvalue is the axis of rotation connecting the two systems. To prove it, we know that a spatial rotation is a linear map in one-to-one correspondence with a  $3 \times 3$  rotation matrix  $\mathbf{R}$  that transforms a coordinate vector  $\mathbf{x}$  into  $\mathbf{X}$ , that is  $\mathbf{R}\mathbf{x} = \mathbf{X}$ . Therefore, another version of Euler's theorem is that for every rotation  $\mathbf{R}$ , there is a nonzero vector  $\mathbf{n}$  for which  $\mathbf{R}\mathbf{n} = \mathbf{n}$ ; this is exactly the claim that  $\mathbf{n}$  is an eigenvector of  $\mathbf{R}$  associated with the eigenvalue 1. Hence it suffices to prove that 1 is an eigenvalue of  $\mathbf{R}$ ; the rotation axis of  $\mathbf{R}$  will be the line  $\mu\mathbf{n}$ , where  $\mathbf{n}$  is the eigenvector with eigenvalue 1.

A rotation matrix has the property that its transpose is equal to its inverse, that is:

$$\mathbf{R}^T\mathbf{R} = \mathbf{R}\mathbf{R}^T = \mathbf{I} \quad (\text{A.2.1})$$

where  $\mathbf{R}^T$  is the transpose of  $\mathbf{R}$  and  $\mathbf{I}$  is the identity matrix  $3 \times 3$ . Since determinant of  $\mathbf{I}$  is equal to 1, according to (A.2.1) we can write:

$$1 = \det(\mathbf{I}) = \det(\mathbf{R})^2 ; \det(\mathbf{R}) = \pm 1 \quad (\text{A.2.2})$$

We know that for a generic matrix  $\mathbf{A}$   $3 \times 3$  the following relation is valid:

$$\det(-\mathbf{A}) = -\det(\mathbf{A}) \quad (\text{A.2.3})$$

Assembling (A.2.3) with the result that  $\det(\mathbf{R}^{-1}) = 1$  since  $\det(\mathbf{R}) = 1$ , it is possible to demonstrate that:

$$\det(\mathbf{R}-\mathbf{I}) = 0 \quad (\text{A.2.4})$$

This shows that  $\lambda = 1$  is a root (solution) of the characteristic equation, that is:

$$\det(\mathbf{R} - \lambda\mathbf{I}) = 0 \text{ for } \lambda = 1 \text{ (A.2.5)}$$

In other words, the matrix  $\mathbf{R} - \mathbf{I}$  is singular and has a non-zero kernel, that is, there is at least one non-zero vector, say  $\mathbf{n}$ , for which:

$$(\mathbf{R}-\mathbf{I})\mathbf{n} = \mathbf{0} \text{ that is } \mathbf{R}\mathbf{n} = \mathbf{n} \text{ (A.2.6)}$$

The line  $\mu\mathbf{n}$  for real  $\mu$  is invariant under  $\mathbf{R}$ , i.e.,  $\mu\mathbf{n}$  is a rotation axis. This proves Euler's theorem.

**Far-field:** considering the seismic wave equation (3.1) (but the question is analogous per equation (3.2)) and we rewrite it in this way:

$$\nabla^2 \mathbf{s}_p - (1/v_p^2)(\partial^2 \mathbf{s}_p / \partial t^2) = -4\pi F(\mathbf{t})\delta(\mathbf{r}_e) \text{ (A.2.7)}$$

where  $\mathbf{s}_p$  is the P wave displacement potential while the term right the equal is the *seismic source term* which can be represented as an impulse (for this reason there is the presence of  $\delta(\mathbf{r}_e)$ ) multiplied by the effective pressure force  $F(\mathbf{t})$  produced by the inelastically deformed interior.  $R_e$  is the elastic radius, that is the radius of a hypothetical spherical surface with the center at the seismic source where infinitesimal strain theory is valid and on which we can predict the elastic displacements and strains due to

$F(t)$ . The solution of (A.2.7) is:

$$s_p(\mathbf{r}, t) = -F[\mathbf{t} - (\mathbf{r}/v_p)]/r \quad (\text{A.2.8})$$

where  $r$  is the distance from  $r_e$ . Thus, seismic waves propagate outward with equal amplitude in all directions on a spherical wavefront. The spherically symmetric displacement field  $u(\mathbf{r}, t)$  is given by:

$$\mathbf{u}(\mathbf{r}, t) = (\partial s_p(\mathbf{r}, t)/\partial \mathbf{r}) = (1/r^2)F[\mathbf{t} - (\mathbf{r}/v_p)] + (1/rv_p)[\partial F(\mathbf{t} - (\mathbf{r}/v_p))/\partial \tau] \quad (\text{A.2.9})$$

where  $\tau = \mathbf{t} - (\mathbf{r}/v_p)$  is the *retarded time*. The first term is called *near-field term*. This term involves displacements that are directly proportional to the reduced displacement potential and that decay rapidly (proportional to  $1/r^2$ ) with distance from the source. The second term is called *far-field term*, which is proportional to the time derivative of the reduced displacement potential. Thus, a step in effective pressure at the source produces an impulsive far-field ground motion. This is a characteristic which allows to find far-field motions from other sources. Generally, if we consider an approximation of point source, that is when epicentral distance is greater than seismic wavelength, in (A.2.9) the only term which we consider is the far-field term.

**Fault:** a fault is a quasiplanar break in the lithosphere across which some previous displacement has occurred and which are hence relatively weak. When the strain (see item in this appendix) accumulation reaches a

threshold imposed by the material properties of the rock and the fault surface, abrupt frictional sliding occurs, releasing the accumulated strain energy. Much of the strain energy is consumed in heating and fracturing of the rocks, but a portion is converted in seismic waves that propagate outward from the fault zone, communicating the disturbance to distant regions (that is, generating an earthquake). The regional deformations continue, leading to many cycles of strain accumulation and release during the active lifetime of the fault. The distinction of the various kinds of fault is based on three parameters. The first is the *strike* ( $\phi$ ), that is the azimuth of the fault's projection onto the surface measured from the north. The second is the *dip* ( $\delta$ ), that is the angle measured downward from the surface to the fault plane in the vertical plane perpendicular to the strike. The third is the *rake* ( $\lambda$ ), that is the angle of slip measured in the plane of the fault from the strike direction to the slip vector showing the motion of the block above the fault, named *hanging wall*, relative to the block below, named *footwall*.

A fault is a *pure strike slip* if  $\lambda = 0^\circ$  (*left-lateral slip*) or  $180^\circ$  (*right-lateral slip*) and if  $\delta = 90^\circ$ , then the fault is called *vertical strike slip*. If  $\lambda = 90^\circ$ , the fault is called *thrust* with the hanging wall which moves upward. If  $\lambda = 270^\circ$ , the fault is called *normal* with the hanging wall which moves downward. In general, the rake will have a value different than these special cases and the motion is then called *oblique slip* with the predominant character being described by stringing together appropriate modifiers (e.g, *right-lateral oblique normal faulting*, for  $180^\circ < \lambda < 270^\circ$ )

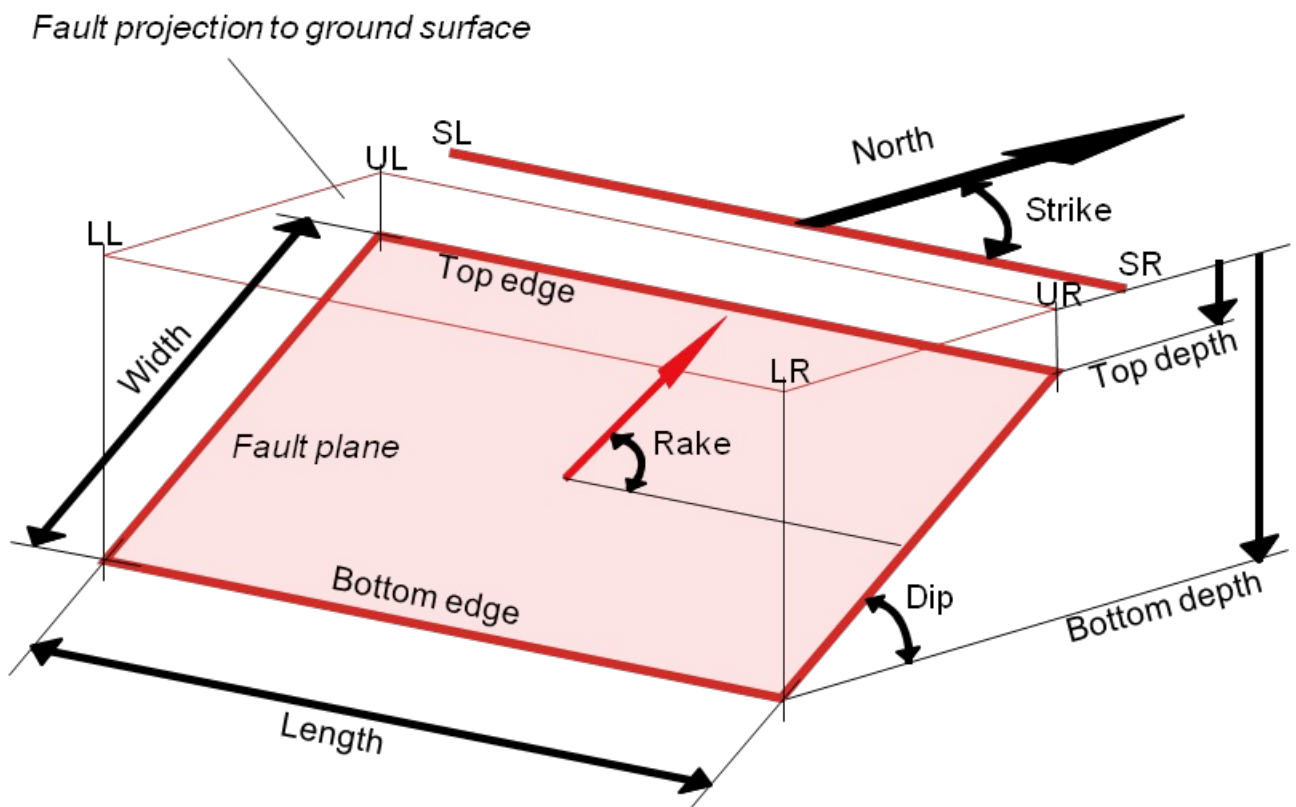


Figure A.2.1: Scheme of a fault and of its characteristics

**Fermat's principle:** This principle, created by the French mathematician Pierre de Fermat, is the principle that the path taken between two points by a ray of light is the path that can be traversed in the least time. This principle is sometimes taken as the definition of a ray of light. However, this version of the principle is not general; a more modern statement of the principle is that rays of light traverse the path of stationary optical length with respect to variations of the path. In other words, a ray of light prefers the path such that there are other paths, arbitrarily nearby on either side, along which the ray would take almost exactly the same time to traverse. In a more precise way, this principle affirms that for a scleronomous isolated system (that is, all its constraints are fixed) the trajectory is travelled by a point in an extremal way.

**Fréchet derivative:** It is a derivative developed by French mathematician Maurice Fréchet. It is used to generalize the situation of the derivative of a real-valued function of a single real variable to the case of a vector-valued function of multiple real variables. Considering  $V$  and  $W$  two Banach spaces,  $U$  an open subset of  $V$ ,  $f : U \rightarrow W$  a Fréchet differentiable function and  $A : V \rightarrow W$  a bounded linear operator such that:

$$\lim_{h \rightarrow 0} \frac{\|f(x+h) - f(x) - Ah\|_W}{\|h\|_V} = 0. \quad (\text{A.2.10})$$

In this way, we can write:

$$Df(\mathbf{x}) = A \quad (\text{A.2.11})$$

where  $A$  is the Fréchet derivative.

**Green's function:** In mathematics, a Green's function is the impulse response of an inhomogeneous differential equation defined on a domain, with specified initial conditions or boundary conditions. Through the superposition principle for linear operator problems, the convolution of a Green's function with an arbitrary function  $f(x)$  on that domain is the solution to the inhomogeneous differential equation for  $f(x)$ . In a more strict way,  $G(x,s)$  is a Green's function of a linear differential operator  $L(x)$  acting on distributions in Euclidean space  $R^N$  at a point  $s$  if:

$$LG(x,s) = \delta(x-s) \quad (\text{A.2.12})$$

Green's functions are named after the British mathematician George Green, who first developed the concept in the 1830s. In the modern study of linear partial differential equations, Green's functions are studied largely from the point of view of fundamental solutions instead. In seismology, Green's functions are used in several aspects. For example, in the expression of the P wave and of S wave motion for a seismic moment tensor (see corresponding item). But their common use is in the computation of propagation filter  $g(t)$  in seismogram (see paragraph 3.3).

**Quality factor:** A seismic wave during its travel undergoes both a elastic attenuation due to epicentral distance and an anelastic attenuation. This last one is due to heat release because of frictions among deforming rocks. Quality factor ( $Q$ ) is a not dimensional parameter that characterizes the

anelastic attenuation. It is defined by following formula:

$$1/Q(\omega) = -(\Delta E/2\pi E) \quad (\text{A.2.13})$$

$-(\Delta E/2\pi E)$  is the fraction of energy dissipated by a seismic wave in an anelastic medium. From (A.2.13), we understand as we have small values of Q in strong attenuating media and vice versa in weak attenuating media.

**Seismic moment tensor:** The displacement in function of time produced by a process of seismic rupture on a fault could be represented by a system of a double couple of time-dependent forces applied on elastic medium. A generic component along the i-th direction of a single couple of forces of this system of double couple could be written as:

$$f_i = -\sum_{j=1,3}(\partial m_{ij}/\partial x_j) \quad (\text{A.2.14})$$

$m_{ij}$  is the **seismic moment tensor per unit volume**. So, forces are strictly connected with their moments. First are connected with stresses responsible of not elastic displacements which happen in a region around a seismic source. Seconds represent the non elastic displacements in seismic source. Integrating on entire volume  $V_0$  of region of seismic source, named focal region, we have:

$$M_{ij} = \iiint m_{ij} dV \quad (\text{A.2.15})$$

where the triple integral has been made on volume  $V_0$ .  $M_{ij}$  is the **seismic**

**moment tensor.**

It is possible to demonstrate that elastic displacements into focal region can be given by the product of  $M_{ij}$  with the derivate of Green's function. For example, for a point seismic source collocated in a cartesian coordinate system  $ijk$  in a point  $\xi$ , the elastic displacement in  $i$ -th direction is given by:

$$\mathbf{u}_i = \mathbf{M}_{kj} \cdot (\partial \mathbf{G}_{ij} / \partial \xi_j) \quad (\text{A.2.16})$$

A very important quantity is the scalar seismic moment  $M_0$ . It is given by:

$$\mathbf{M}_0 = \mu \Delta u \Sigma \quad (\text{A.2.17})$$

where  $\mu$  is the rigidity,  $\Delta u$  is the medium displacement and  $\Sigma$  is the area on which displacement happens. It is a significant quantity because it supplies us the real energetic importance of an earthquake. In fact, it is connected with the magnitude of an earthquake by means of so-called **magnitude moment  $M_w$** , that is given by:

$$\mathbf{M}_w = 2/3(\log_{10} \mathbf{M}_0 - 9.1) \quad (\text{A.2.18})$$

**Seismic ray:** A geometric construction that describes the propagation of a seismic wave in a medium when there is the so-called high-frequency approximation (that is, epicentral distance is much greater than

wavelength). A seismic ray is orthogonal to the wavefront. They are straight lines in a homogeneous elastic medium, curves in a not homogenous elastic medium. Its equation is:

$$\left(\frac{d}{ds}\right)\left[\frac{1}{c(\mathbf{r})}\left(\frac{d\mathbf{r}}{ds}\right)\right] = \nabla\left(\frac{1}{c(\mathbf{r})}\right) \quad (\text{A.2.19})$$

where  $\mathbf{r}$  is the seismic ray,  $d\mathbf{s}$  is the arc length and  $c$  is the velocity of a seismic wave.

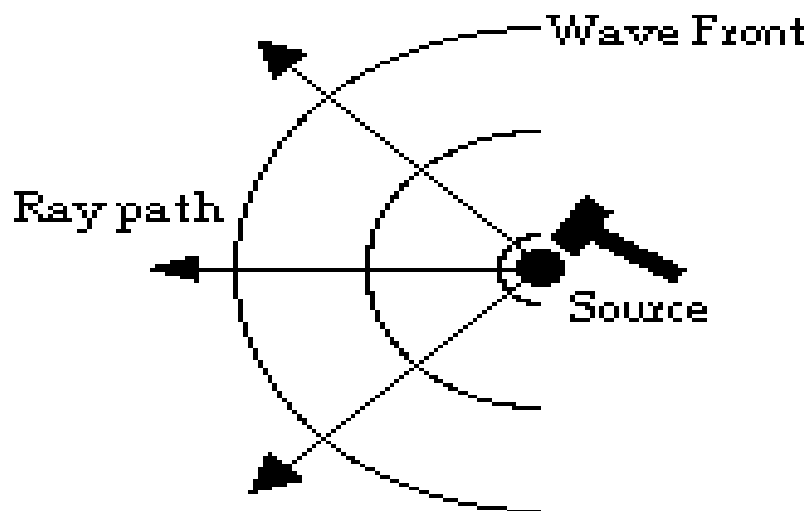


Figure A.2.2: Geometric scheme of a seismic raypath

## Appendix 3

### The Fast Marching Algorithm

The *Fast Marching* is an algorithm that was written and implemented by **James A. Sethian** and **A. Mihai Popovici** in 1999 for solving Eikonal equation to compute traveltimes. They write the equation (1.23) for a grid point (i,j,k) of a 3D discretized space (x,y,z) as:

$$[\max(D_{ijk}^{-x}T, -D_{ijk}^{+x}T, 0)^2 + \max(D_{ijk}^{-y}T, -D_{ijk}^{+y}T, 0)^2 + \max(D_{ijk}^{-z}T, -D_{ijk}^{+z}T, 0)^2]^{1/2} = S_{ijk} \quad (\text{A.3.1})$$

where  $D_{ijk}^{-x}T$  and  $-D_{ijk}^{+x}T$  are respectively:

$$D_i^{-x}T = (T_i - T_{i-1})/h ; D_i^{+x}T = (T_{i+1} - T_i)/h \quad (\text{A.3.2})$$

where h is the distance between two grid points (that is between the (i-1)-th grid point and the i-th grid point and between the i-th grid point and the (i+1)-th grid point along x direction, but the (A.3.2) could be written in an analogous way both for y direction and z direction.  $S_{ijk}$  is the slowness computed in a grid point (i, j, k).  $\max(D_{ijk}^{-x}T, -D_{ijk}^{+x}T, 0)$ ,  $\max(D_{ijk}^{-y}T, -D_{ijk}^{+y}T, 0)$ ,  $\max(D_{ijk}^{-z}T, -D_{ijk}^{+z}T, 0)$  are respectively  $dT/dx$ ,  $dT/dy$  and  $dT/dz$ .

This algorithm is based on an *upwind* loop. That is, the information propagates one way from smaller value of  $T(x, y, z)$  to larger values. Hence, it rests on solving equation (A.3.1) by building the solution outward from the smallest  $T(x,y,z)$  value.

Practically, the algorithm considers a narrow band of trial points around accepted points on which (A.3.1) has been yet solved and it marches this band forward, remembering the values that (A.3.1) has been obtained on previous points and bringing new grid points in a narrow band. The choice of these last ones is the keystone about the good working of algorithm. We can summarise the functioning of algorithm in the following steps.

- It chooses as “Trial point” the grid point - among the Close points to the yet Accepted points - which has the smallest value of  $T(x,y,z)$ .
- This trial point is inserted in Accepted points, while its neighbours are inserted in Close points.
- It repeats the step 1) to find a new trial point. It belongs, together with initial trial point, to the narrow band.
- Finding trial point, it repeats the step 2)

The algorithm stops when narrow band of trial points reaches the top of the grid. Number of realised steps in the loop depend on  $N_B$ , that is the number of grid points inserted into the narrow band. If this is known, the total number of steps for loop is  $N \log N_B$ , otherwise is  $N \log N$ , where  $N$  is the total number of grid points.

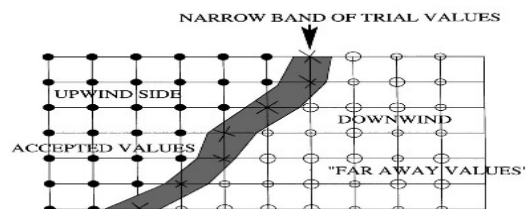


Figure A.3.1: Scheme of upwind construction of narrow band in Fast Marching Algorithm (from “3-D travelttime computation using the Fast Marching Method”, Sethan & Popovici, Geophysics, vol.64, No.2 (1999), 516-523)

## Appendix 4

### The SVD and the subspace method

We consider a real or complex  $m \times n$  matrix  $M$ . ***Singular Value Decomposition***, best known simply as ***SVD***, is a particular factorization of matrix  $M$  given by:

$$\mathbf{M} = \mathbf{U}\mathbf{\Sigma}\mathbf{V}^* \quad (\text{A.4.1})$$

where  $\mathbf{U}$  is a  $m \times m$  unitary matrix (and if its elements are real, it is also an orthogonal matrix),  $\mathbf{\Sigma}$  is a  $m \times n$  diagonal matrix with non-negative real numbers on diagonal that are named ***singular values*** and  $\mathbf{V}^*$  is the conjugate transpose of a  $n \times n$  unitary matrix.

Practically, columns of  $\mathbf{U}$  are orthonormal eigenvectors of  $\mathbf{M}\mathbf{M}^*$  (where  $\mathbf{M}^*$  is the conjugate transpose of  $\mathbf{M}$ ) while columns of  $\mathbf{V}$  are eigenvectors of  $\mathbf{M}^*\mathbf{M}$ .

In a traveltimes seismic tomography, the matrix  $\mathbf{M}$  is a  $L \times p$  matrix, where  $L$  are the number of seismic events which from we have traveltimes and  $p$  are the number of parameters to determine after inversion (usually, they are the three coordinates of re-localization of a single seismic event and the seismic velocity of that seismic event). As written in paragraph 1.5, SVD is used to eliminate redundant values during the computation of inverse problem.

In FMST code (see paragraph 4.3), SVD acts after the implementation of so-called ***subspace method***. This method is used because it projects the

full linearized inverse problem onto a much smaller  $n$ -dimensional model space. The advantage of this approach is that the solution to the inverse problem only requires the inversion of a  $n \times n$  matrix.

The subspace method was implemented by Kennett, Sambridge and Williamson in 1988.

First of all, we rewrite (1.14) considering a current model  $\mathbf{m}_c$ , putting  $\delta\mathbf{m}$  as  $\mathbf{m} - \langle\mathbf{m}\rangle$  and stopping at second order the Taylor's series, so considering Hessian too. In this way, we have:

$$E(\mathbf{m}_c + \delta\mathbf{m}) = E(\mathbf{m}_c) + \boldsymbol{\gamma} \delta\mathbf{m} + (1/2) \delta\mathbf{m} \mathbf{H} \delta\mathbf{m} \quad (\text{A.4.2})$$

where  $\boldsymbol{\gamma}$  is the gradient given by:

$$\boldsymbol{\gamma} = \mathbf{G}^T \mathbf{W}_D^{-1} \mathbf{G} - \mathbf{G}^T \mathbf{W}_D^{-1} \mathbf{d} + \mathbf{W}_M^{-1} (\mathbf{m} - \langle\mathbf{m}\rangle) \quad (\text{A.4.3})$$

and  $\mathbf{H}$  is the Hessian matrix given by:

$$\mathbf{H} = \mathbf{G}^T \mathbf{W}_D^{-1} \mathbf{G} + \nabla_{\mathbf{m}} \mathbf{G}^T \mathbf{W}_D^{-1} \mathbf{G} - \nabla_{\mathbf{m}} \mathbf{G}^T \mathbf{W}_D^{-1} \mathbf{d} + \mathbf{W}_M^{-1} \quad (\text{A.4.4})$$

where matrices  $\mathbf{G}$ ,  $\mathbf{W}_D$ ,  $\mathbf{W}_M$  play same roles as in paragraph 1.

We consider  $n$  basis vectors  $\mathbf{a}_i^{(j)}$ , with  $i = 1, \dots, N$  and  $j = 1, \dots, n$  (where  $N$  is the number of parameters to determine) and a projection matrix  $\mathbf{A}$  composed of the components of these vectors. We rewrite  $\delta\mathbf{m}$  as:

$$\delta\mathbf{m} = \sum_{j=1, n} \mu_j \mathbf{a}^{(j)} \quad (\text{A.4.5})$$

The coefficients  $\boldsymbol{\mu}$  are to be determined by minimizing (A.4.2) that, with the expression (A.4.5), becomes:

$$\mathbf{E} = \mathbf{E}(\mathbf{m}_C) + \sum_{j=1,n} \boldsymbol{\mu}_j \mathbf{a}^{(j)} + (1/2) \sum_{j=1,n} \sum_{k=1,n} \boldsymbol{\mu}_j \boldsymbol{\mu}_k \mathbf{a}^{(k)\top} \mathbf{H} \mathbf{a}^{(j)} \quad (\text{A.4.6})$$

After the minimization of (A.4.6) respect to  $\boldsymbol{\mu}_j$  we have:

$$\boldsymbol{\gamma} \mathbf{a}^{(j)} + \sum_{k=1,n} \boldsymbol{\mu}_k \mathbf{a}^{(k)\top} \mathbf{H} \mathbf{a}^{(j)} = \mathbf{0} \quad (\text{A.4.7})$$

We rewrite (A.4.7) by means of a projection matrix  $\mathbf{A}$  composed of the components of vectors  $\mathbf{a}_j$  and we have:

$$\mathbf{A}^\top \boldsymbol{\gamma} + \mathbf{A}^\top \mathbf{H} \mathbf{A} \boldsymbol{\mu} = \mathbf{0} \quad (\text{A.4.8})$$

The perturbation coefficients can be determined from the projection of the gradient and the Hessian matrix onto the subspace and so we have:

$$\boldsymbol{\mu} = -(\mathbf{A}^\top \mathbf{H} \mathbf{A})^{-1} \mathbf{A}^\top \boldsymbol{\gamma} \quad (\text{A.4.9})$$

The projected Hessian is a small  $n \times n$  matrix, which is generally well conditioned with sensible choices for the basis vectors  $\mathbf{a}^{(j)}$ . The model perturbation  $\boldsymbol{\delta m}$  can be recovered by projecting back into the full model space. In this way, we have:

$$\delta \mathbf{m} = -\mathbf{A}[\mathbf{A}^T(\mathbf{H}_0 + \mathbf{W}_M^{-1})\mathbf{A}]^{-1}\mathbf{A}^T\boldsymbol{\gamma} \quad (\text{A.4.10})$$

where  $H_0$  is the Hessian of the data-fit term. The basis vectors  $\mathbf{a}^{(j)}$  will normally be related to the ascent gradient vector  $\boldsymbol{\gamma}$  and its rate of change and so (A.4.10) normally combines to some extent gradient and matrix techniques for minimizing (A.4.6). Once the (A.4.10) has been estimated, a new  $m_C$  is created and used to generate a further local quadratic approximation to the behaviour of  $E$ . The cycle of estimating  $\delta \mathbf{m}$  and model construction is then iterated until a suitable termination criterion for the minimization of  $E$  is activated.

If we have different types of parameters  $A, B, C, \text{ecc...}$ , model space becomes a product space  $M = M_A \times M_B \times M_C$ . Subspace method can be applied, partitioning both the gradient vector  $\boldsymbol{\gamma}$  and the Hessian matrix for each parameter type and applying the subspace method to each single partition.

For seismic tomography, we have two major parameter classes: hypocentral parameters and velocity field parameters. In thesis, we fix dimension of subspace equal to 5. This because the partition of model is:

$$\mathbf{m} = [\mathbf{h}_x, \mathbf{h}_t, \mathbf{v}_P, \mathbf{v}_{PC}, \mathbf{v}_{PM}] \quad (\text{A.4.11})$$

where  $\mathbf{h}_x$  is the partition of spatial hypocentral coordinates of all events,  $\mathbf{h}_t$  is the partition of origin times of all events,  $\mathbf{v}_P, \mathbf{v}_{PC}$  and  $\mathbf{v}_{PM}$  are velocity of P-waves of events (respectively absolute, crust and mantle).

## Bibliography

**H.M Benz – B.A Chouet – P.B Dawson – J.C Lahr – R.A Page – J.A Hole: *Three Dimensional P And S Wave Velocity Structure Of Redoubt Volcano, Alaska* – *Journal of Geophysical Research* – Vol.101, No.B4, pp. 8111-8128 – 1996**

**H.M Benz, R.B Smith – *Simultaneous Inversion For Lateral Velocity Variations And Hypocenters In The Yellowstone Region Using Earthquake And Refraction Data* – *Journal of Geophysical Research* – Vol.89, No.B2, pp. 1208-1220 - 1984**

**M. Calò, C. Dorbath, D. Luzio, S.G Rotolo, G. D'Anna – *Seismic velocity structures of southern Italy from tomographic imaging of Ionian slab and petrological inferences* – *Geophysical Journal International* – Vol.191, No.2, pp. 751-764 - 2012**

**C. Chiarabba, P. De Gori, F. Speranza – *The southern Tyrrhenian subduction zone: deep geometry, magmatism and Plio-Pleistocene evolution* – *Earth and Planetary Science Letters* – Vol. 268, pp. 408-423 – 2008**

**A. García-Yeguas, I. Koulakov, J.M Ibáñez, A. Rietbrock - *High***

***resolution 3D P wave velocity structure beneath Tenerife Island (Canary Islands, Spain) based on tomographic inversion of active-source data – Journal of Geophysical Research – Vol.117, B09309 - 2012***

**I. Guerra, P. Harabaglia, A. Moretti – *La sismicità della Calabria nel contesto geodinamico del Mediterraneo – 8 Settembre 1905, terremoto in Calabria - pp. 167-179 - 2006***

**B.L.N Kennett, M.S Sambridge, P.R Williamson – *Subspace methods for large inverse problems with multiple parameter classes – Geophysical Journal – Vol. 94, pp. 237-247 - 1988***

**B.L.N Kennett, E.R Engdahl, R. Buland – *Constraints on seismic velocities in the Earth from traveltimes – Geophysical Journal – Vol. 122, pp. 108-124 – 1995***

**C. Kincaid, P. Olson – *An Experimental Study of Subduction and Slab Migration – Journal of Geophysical Research – Vol. 92, No. B13, pp. 13832-13840 – 1987***

**I. Koulakov – *LOTOS code for local earthquake tomographic inversions. Benchmarks for testing tomographic algorithms – Bulletin of Seismological Society of America – Vol. 99, No.1, pp. 194-214 – 2009***

**I. Koulakov, M.K Kaban, M. Tesauero, S. Cloething – *P- and S- velocity***

***anomalies in the upper mantle beneath Europe from tomographic inversion of ISC data*** – *Geophysical Journal International* – Vol. 179, pp. 345-366 - 2009

**T. Lay, T.C Wallace** – *Modern Global Seismology* – Academic Press, 1995

**C. Montuori, G.B Cimini, P. Favali** – *Teleseismic tomography of the southern Tyrrhenian subduction zone: new results from seafloor and land recordings* – *Journal of Geophysical Research* – Vol. 112, No.B03311 - 2007

**G. Neri, B. Orecchio, C. Totaro, G. Falcone, D. Presti** – *Subduction beneath Southern Italy close the ending: results from seismic tomography* – *Seismological Research Letters* – Vol. 80, pp. 63-70 – 2009

**G. Nolet** – *Seismic wave propagation and seismic tomography* - Chapter 1 of *Seismic Tomography*, edited by G. Nolet – 1987

**C.C Paige, M.A Saunders** – *LSQR: An Algorithm for Sparse Linear Equations and Sparse Least Squares* – *ACM Transactions on Mathematical software* - Vol. 8, No. 1, pp. 43-71 - 1982

**J. Plomerova, V. Babuska, R. Scarpa – *Teleseismic P-residual study in the Italian region -inferences on large scale anisotropic structure of the subcrustal lithosphere* – *Annali di Geofisica*, Vol. 41, No. 1, pp. 33-48 – 1998**

**N. Rawlinson, B.L.N Kennett, M. Heintz – *Insights into the structure of the upper mantle beneath the Murray Basin from 3D teleseismic tomography* – *Australian Journal of Earth Sciences* – Vol. 53, pp. 595-604 – 2006**

**G. Selvaggi, C. Chiarabba – *Seismicity and P-wave velocity image of the southern Tyrrhenian subduction zone* – *Geophysical Journal International* - Vol. 121, pp. 818-826 – 1995**

**A. Tarantola – *Inverse Problem Theory: Methods for Data Fitting and Model Parameter Estimation* – Elsevier, Amsterdam - 1987**